Simulation of a simplified 2D MHD model of plasma sheet thinning

Rudolf TRETLER

A dissertation submitted in partial fulfillment
of the requirements for the degree of
Doctor of Science

The University of Electro-Communications

Department of Communication Engineering and Informatics

Chōfu, Tokyo, Japan

March 2021

English title:	Simulation of a simplified 2D MHD model of plasma sheet thinning
Japanese title:	プラズマシート幅の減少に関する2次元MHDシミュレーション

Advisor:	Associate Professor Tomo Tatsuno
Secondary advisor:	Professor Keisuke Hosokawa
Supervisory committee:	Associate Professor Tomo Tatsuno Professor Keisuke Hosokawa Professor Nobito Yamamoto Professor Yoshinobu Nakatani Associate Professor Tadashi Yamazaki

概要

オーロラの発生源は、地球磁気圏内の強磁場の磁気ローブに南北から挟まれ、赤道付近で弱磁場の「プラズマシート」と呼ばれる領域にある。プラズマシート内のプラズマ粒子が磁力線に沿って地球方面に流れ、大気の中性粒子と衝突し励起させる。大気の粒子が元の状態に戻るとき、発光してオーロラとして見られる。サブストームという地球磁気圏の乱れによりプラズマ粒子の流れが強くなることがあり、それに伴ってオーロラも増幅され、「オーロラ爆発現象」を起こす。オーロラ爆発現象は磁気圏内のいくつかの物理現象と関連があることがわかっているが、それらの因果関係が未だに解明されていない。この問題を解決する候補の一つである電流擾乱 (Current Disruption; CD) モデルによると、プラズマシート内には磁気テイル（太陽と反対側）方面に「希薄波」が伝搬し、地球方面のプラズマ流を引き起こすとされている。プラズマが損失されるにつれて、プラズマシート幅も減少する可能性がある。

Chao らは CD モデルの簡単な 1 次元モデルを用いて、希薄波の伝搬と地球プラズマシートの幅の減少を調べた [J. K. Chao *et al.*, Planet. Space Sci. 25, 703 (1977)]。その結果が衛星観測等により CD モデルの正当性を判断するために用いられている。本論文では、Chao らの 1 次元モデルを 2 次元磁気流体 (MHD) モデルに拡張し、シミュレーションして解析を行った。

まず第 1 章を序論とし、地球磁気圏の構造、オーロラ爆発現象とそのモデルを紹介した。

第 2 章では、本研究で基礎方程式として用いる理想 MHD 方程式を保存則形式で導入し、シミュレーション設計に必要な特性分解と連立方程式系の対角化について述べた。

第 3 章では、本論文で用いるシミュレーション手法を解説した。空間差分は不連続性に強い Essentially Non-Oscillatory 法、時間差分は 3 次の Runge-Kutta 法を用いた。空間差分の設計には前章の対角化を利用した。

第 4 章では、先行研究である Chao らが提案した 1 次元モデルのシミュレーションを行い、結果を確認した。Chao らは仮想的なピストンを用意し、ピストンを引くと希薄波が発生することを利用して CD モデルを構築した。本研究では 2 次元への拡張を考え、シート内プラズマの一部に初期速度を与えることで、CD モデルの特徴とされる希薄波をテイル方面に放つこととした。元の 1 次元モデルでは、希薄波が音速でテイル方面

に伝搬する。希薄波の通過に伴う圧力の減少はプラズマシート幅の減少を引き起こし、幅の減少も音速で伝達する可能性が示唆されている。

第 5 章では、本題の 2 次元 MHD モデルへの拡張を行い、磁場がない流体としてのシミュレーションと磁場があるプラズマシート構造としてのシミュレーション結果について詳述した。2 次元 MHD モデルでは、磁場がないプラズマシート領域の北側と南側に接線不連続面で繋がっている強磁場の磁気ローブ領域を追加したことで結果が変わり、希薄波がプラズマシートの圧縮により呑み込まれてほぼ消滅する。しかし、希薄波により引き起こされると考えられていたプラズマシート幅の減少は多少弱まり遅くなるだけで、伝達し続ける。さらに、その伝達速度は 1 次元モデルとは異なり磁気ローブの磁場の強さに依存していることがわかった。尚、圧力の増加を伴う波列がシート幅の減少を先導する形でシート内に音速でテイル方面に伝搬する。

2 次元モデルのシミュレーション結果を物理的に理解するために、波の分解を行った。MHD モデルには 7 つの波（エントロピー波、正と負の速い磁気音波、正と負の遅い磁気音波、正と負の Alfvén 波）が存在するが、シミュレーション結果をそれらに分解して支配的な成分を特定した。分解して得られた結果は、まず、プラズマシート内での希薄波がほぼ消滅することを確認できた。次に、シート幅の減少の前に伝搬する波列は速い磁気音波として進行していく。また、南北に伝わるシート内の速い磁気音波がシートとローブの境界面に衝突すると、その波の一部がローブに渡り速い磁気音波と遅い磁気音波に分解され、残りが反射してシートに戻ることが観測できた。逆に、ローブ内で励起された遅い磁気音波がシートとの境界面に当たると、その進行速度がゼロになり、境界面で溜まる。速い磁気音波と遅い磁気音波に比べて、エントロピー波の成分が弱く、Alfvén 波が全く励起されていないこともわかった。

第 6 章ではまとめと結論を述べた。モデルを拡張したことで結果が 1 次元モデルと比べて大きく変化した。すなわち、1 次元モデルで扱えなかったシートとローブの相互作用がプラズマシート幅の減少に大きな影響を与えていることが明らかになった。また、希薄波がほぼ消滅したということは、希薄波の観測の有無は電流擾乱モデルの正当性に繋がらない可能性があることも意味している。さらに、幅の減少とその進行速度が観測データと矛盾しないことが確認された。以上より、現在の観測方法では、CD モデルの正当性を判定することは困難であると考えられる。

Abstract

There are several competing models trying to explain the physical processes behind auroral breakup, an event where aurora suddenly increases in strength during a magnetospheric substorm. A one dimensional (1D) model for thinning of the Earth's plasma sheet according to the Current Disruption (CD) scenario of auroral breakup was introduced by Chao et al. [J. K. Chao *et al.*, Planet. Space Sci. 25, 703 (1977)], and the model's results form the basis for satellite observations which attempt to determine the CD model's validity. In this thesis, the 1D model is extended to a simple two dimensional (2D) ideal magnetohydrodynamic (MHD) configuration and simulated. In both simplified models, an initial disturbance launches a rarefaction wave towards the magnetotail, which is considered a signature component of the CD model.

In this thesis, overview of the problem and the physical background of auroral breakup are described in Chapter 1.

The ideal MHD equations, their properties, and their formulation as a system of conservation laws are introduced in Chapter 2. The diagonalization procedure based on the theory of characteristics, which will be used when constructing the simulation scheme, is also described.

The development of the simulation code for the MHD equations in their conservation law formulation is presented in Chapter 3. The spatial integration uses the Essentially Non-Oscillatory (ENO) scheme applied to the diagonalized system of MHD equations, while the time stepping uses the three-stage third-order Runge–Kutta scheme.

Chapter 4 reproduces Chao's 1D model, where the plasma sheet thinning is modeled in two distinct stages. First, a rarefaction wave propagates tailward at sound velocity, lowering the sheet pressure; second, the sheet–lobe boundary is assumed to move inwards, reducing the thickness of the plasma sheet. The problem is then reformulated it so it can be extended to 2D.

Chapter 5 is the heart of this thesis; the 1D plasma sheet model is extended to 2D, where the north and south lobe magnetic fields are included in the simulation, simulated under a wide range of parameters,

and the results analyzed. In the extended model, due to sheet recompression, the rarefaction wave is weakened almost to the point of disappearance, with a corresponding drastic weakening of the pressure drop in the plasma sheet. However, the thinning continues to propagate, albeit at a slower velocity than the 1D model suggests; this indicates that the rarefaction wave is not a sole component of plasma sheet thinning. The propagation velocity is also strongly influenced by the strength of the lobe magnetic field, which was outside the scope of the 1D model. Additionally, the thinning front is preceded by a wave train of pulses with slightly increased pressure.

To analyze the simulation results, they were decomposed into their component MHD waves to determine the dominant components. The decomposition confirmed the weakening of the rarefaction wave in the plasma sheet, and showed that the wave train preceding the thinning front consists of fast-mode MHD waves (sound waves). The thinning itself appears to be driven by the slow-mode waves in the magnetic lobes impacting the sheet–lobe boundary, where the slow magnetosonic velocity is sharply reduced, which launches fast-mode waves across the sheet through mode conversion.

Finally, the conclusion is given in Chapter 6, and followed by several appendices. The results of the simulation hint that the presence or absence of the rarefaction wave in the plasma sheet may not be sufficient to determine validity of the CD model. Furthermore, a comparison with the observational data shows that the propagation velocity of the thinning front and the reduction in sheet thickness are within the plausible range of values. This indicates that current observational methods may not be sufficient to prove nor disprove the CD model of auroral breakup.

Contents

Chapter 1

Introduction

> *Space is big. You just won't believe how vastly, hugely, mind-bogglingly big it is. I mean, you may think it's a long way down the road to the chemist's, but that's just peanuts to space.*
>
> —*Douglas Adams, The Hitchhiker's Guide to the Galaxy*

As the late-and-great Douglas Adams so artfully describes, space is vast, and the distances involved are enormous. Unfortunately, this creates some problems when attempting to decipher the physical workings of events taking place off-planet. The development of space programs and slow but steady reductions in launch costs has allowed for deployment of a great many satellites and satellite constellations, whose observational data has been invaluable in determining, among other things, the structure and behavior of Earth's magnetosphere.

However, due to the aforementioned vastness of space, there are countless mysteries that yet have to be solved. Many of those unsolved problems are connected to events that happen over a wide area, and/or are very infrequent. That makes it difficult to capture enough data for a successful analysis, as the chance that any of the observation satellites might be in the vicinity is fairly low. What we can do, however, is use the limited data to form models, and the (even more meteorical) rise in the computational power to simulate them, checking if and how the model and the observation fit together.

1.1 General overview

In this thesis, a simplified model of a certain near-Earth event has been simulated and the results analyzed. The event in question occurs in the Earth's *magnetosphere*, which is the area around our planet where the Earth's magnetic field dominates the Sun's magnetic field (see section 1.2.1). The magnetosphere (and interplanetary space in general) is filled with (low-density) plasma, a charged gas where atoms have been dissociated into electrons and ions. When plasma from the magnetosphere is disturbed, some of it may flow down the magnetic field lines into the atmosphere, colliding with the neutral particles, exciting (and often ionizing) them. Photons emitted when the excited particles return to their ground state can be observed as *aurora*, which is normally expressed as a subdued glow visible in the sky at high latitudes.

A sudden increase in auroral strength, called *auroral breakup*, can occasionally be observed during periods of intense geomagnetic activity [1] (see figure 1.1). While auroral breakup is a highly visible effect, observable from the Earth's surface, the changes in the Earth's magnetosphere related to the event are much more difficult to monitor. Due to very large distances and very low matter densities involved, the magnetosphere conditions—even the state of the (relatively) high density area called *plasma sheet*—cannot be observed from the surface of the Earth, and require a direct measurement with a satellite. As mentioned earlier, the distances involved are large (one might even say "astronomical"), and since auroral breakups are rare, there is a very limited amount of observational data. As a consequence, many aspects of the events leading up to and surrounding the auroral breakup have not yet been conclusively determined, and there are many competing models attempting to explain the process [2].

One of the aspects that are not in question is that the auroral breakup occurs due to a sudden influx of plasma from the Earth's plasma sheet into the atmosphere (see section 1.2.4), and the related formation of a near-Earth neutral line. However, the ordering of these events is unclear: does the neutral line form first, pushing plasma towards the Earth and finally into the atmosphere; or does the near-Earth plasma flow into the atmosphere first, thinning the

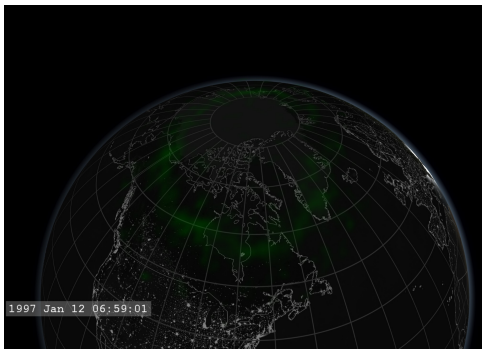

(a) The usual, subdued glow of the aurora.

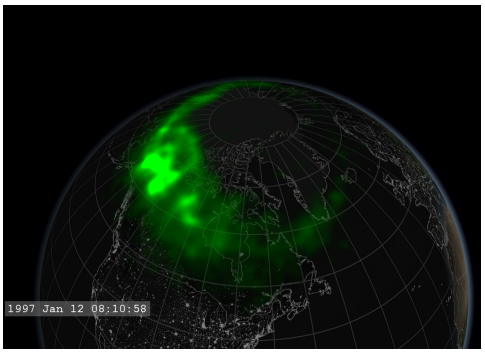

(b) Peak of the auroral breakup.

Figure 1.1: Auroral breakup captured in January 1997 by the visible light camera of the *Polar* satellite [3]. Public domain images by NASA [4] (the source also includes an animation of the entire event).

plasma sheet and causing the neutral line to form? The former is the assertion of the *near-Earth neutral line* (NENL) model [5], while the latter is what the *current disruption* (CD) model [6] states. Currently, most researchers favor the NENL model; however, this thesis focuses on the CD model, simulating the predicted behavior of the plasma sheet and attempting to clarify to what extent the conventional model applies to the observational data. To that end, we focus on what is considered to be the signature aspect of the CD model: a rarefaction wave traveling tailward from the location of the titular current disruption.

In this thesis, we present a simplified two dimensional (2D) magnetohydrodynamic (MHD) model of the rarefaction wave in the Earth's plasma sheet. The model is an extension of a one dimensional (1D) model introduced by Chao *et al.* [7]. Chao's model employed a piston to generate a rarefaction wave in a 1D gas tube (which represents the inner plasma sheet); a problem with an exact solution which was then extrapolated to the entire plasma sheet (see section 4.1 for details).

While satellite observations of the plasma sheet thinning (for example, the THEMIS mission [8]) have been conducted, and the data analyzed with the intent to ascertain the validity of the CD model, a review of available literature

has not revealed any simulations of the thinning propagation in the plasma sheet as described by the model. It would appear that the 1D approximation by Chao *et al.* has been used as a foundation for comparison between CD model's predictions and observations. However, some problems inherent in the (necessarily rough) approximation can be pointed out. For example, there is no mechanism in the 1D model to account for the effects that the rest of the plasma sheet and the magnetic lobes may have on the behavior of the (magnetically neutral) inner plasma sheet, which may make it deviate from the shape of a 1D rarefaction wave; therefore, the interaction in the 1D piston model is strictly one-directional. Additionally, as will be explained in more detail later on in section 5.8, the propagation velocity of thinning itself is not explicitly stated in the paper; from the way properties of the post-thinning sheet are calculated, it can be concluded that thinning may not even propagate at all.

The 2D MHD model presented in this thesis attempts to improve on the 1D piston model by extending the modeled area to a cross-section of the plasma sheet, including parts of the magnetic lobes. (The physical configuration of the modeled area has been simplified for easier analysis.) By extending the approximation to include the magnetic lobes, we can directly measure the properties of plasma sheet thinning if it were to proceed according to the CD model. Of course, the simulation presented in this thesis is still a simplified version of the CD model, and the results are in no way conclusive. Nevertheless, it does bring us one step closer, and allows us to determine some potential inadequacies of the 1D approximation.

The structure of this thesis is as follows. The physical background, including a short description of the Earth's magnetosphere and the two models (NENL and CD), will be presented later in this chapter. The MHD equations, their properties, and their formulation as a conservation law will be introduced in Chapter 2. The simulation scheme and implementation of the self-developed code used to run the simulations in this thesis will be described in Chapter 3. The 1D piston model by Chao *et al.*, as well as an alternative formulation that will be used as a basis of the extension to 2D, will be shown

in Chapter 4. The aforementioned extension of the plasma sheet model to 2D, as well as the simulation results and their analysis, will be presented in Chapter 5. The conclusion to this thesis is in Chapter 6. Finally, there are several appendices. In Appendix A, the order of the three-step Runge-Kutta method used in the simulation is determined, and in Appendix B the results of some standard numerical tests are presented. Appendix C shows the validity of the simulation domain size through running some of the simulations on a larger domain. Influence of the Kelvin-Helmholtz instability is discussed in Appendix D. Appendix E shows the results of testing a couple of candidate wave decomposition methods (used for analysis of simulation results in section 5.6) on a linear wave problem. And finally, Appendix F describes some attempts to analytically derive the relationship between the parameters of the plasma sheet and the properties of the thinning, although we ended up here with not much progress.

1.2 Physical background

1.2.1 Earth's magnetosphere and plasma sheet

The shape and structure [9] of the Earth's magnetic field is depicted in figure 1.2, with a more evocative artist's rendition shown in figure 1.3. The solar wind, a highly conducting plasma that is emitted by the Sun, carries with itself the Sun's coronal magnetic field. As the (supersonic) solar wind flows outward, it collides with the magnetic fields of other bodies in the solar system, including Earth, generating a *bow shock*. As it passes through the bow shock, the solar wind plasma slows down and heats up, creating the *magnetosheath* (the pink-shaded region in figure 1.2), a region between the bow shock and the Earth's magnetic field. Since the magnetic field lines cannot interpenetrate, and solar wind plasma, due to the high conductivity, is frozen-in to the Sun's magnetic field it carries with itself, the solar wind has to deflect around the Earth's magnetic field. This creates a cavity called *magnetosphere* (the blue-shaded region in figure 1.2).

Due to the pressure exerted by the the solar wind plasma, the dipole mag-

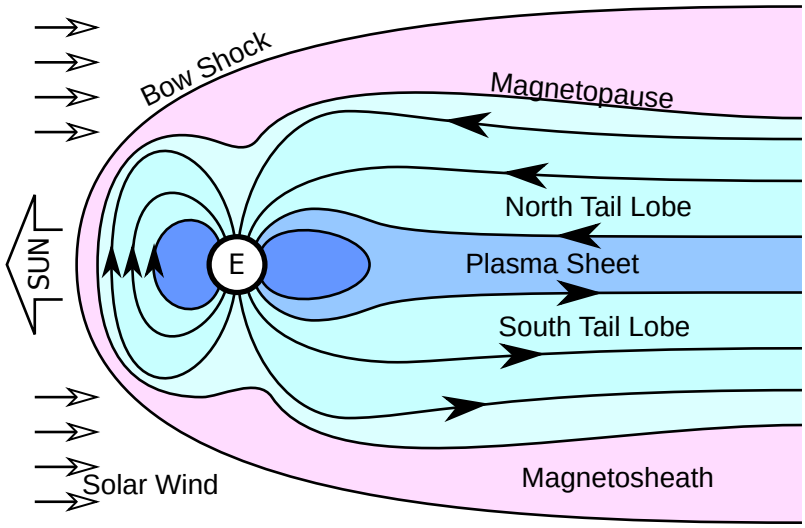

Figure 1.2: Rough schematic of the structure of the Earth's magnetosphere. Supersonic solar wind collides with the terrestrial magnetic field and generates a bow shock. Between the bow shock and the Earth's magnetic field, which is bounded by magnetopause, is the magnetosheath. The terrestrial magnetic field is deformed by the solar wind pressure, and becomes compressed in front and stretched out in the back (magnetotail). The magnetotail can be further divided into north and south magnetic lobes, with a plasma sheet separating the lobes.

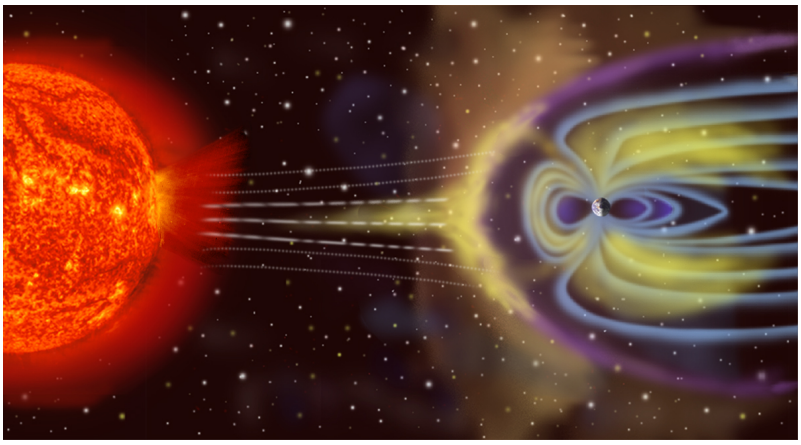

Figure 1.3: Artist's rendition of the Earth's magnetosphere. Image taken from Wikipedia (`https://en.wikipedia.org/wiki/File:Magnetosphere_rendition.jpg`); original source NASA (`http://sec.gsfc.nasa.gov/popscise.jpg`, no longer available).

netic field generated by the Earth is deformed, with a compressed region in the front, and a stretched-out region in the back, called *magnetotail*. The magnetotail can further be divided into the *north* and *south magnetic lobes*.

The magnetic field lines from the north and south lobes are stretched from the dipole configuration and become almost anti-parallel. As a result, in the center region the magnetic field is weakened, and to keep the entire configuration balanced, the density and kinetic pressure increase. This region of increased plasma density within a weak magnetic field is called the *plasma sheet*, or *neutral sheet*. The typical thickness of the plasma sheet during geomagnetically calm periods is 1 to $3R_{\mathrm{E}}$, where R_{E} denotes the radius of the Earth, with very high plasma beta values, on the order of $\beta \approx 100$, where plasma beta $\beta = 2\mu_0 p/B^2$ is the ratio between kinetic pressure p and magnetic pressure $B^2/(2\mu_0)$, where B is the magnetic field strength and μ_0 is the magnetic permeability of vacuum.

Flowing dawn to dusk across the plasma sheet is the *cross tail current*, also known as *neutral sheet current*. It is a diamagnetic current caused by the gradient in the plasma pressure, and combined with several other currents forms the large-scale magnetospheric current system.

The shape of the magnetic field lines and the frozen-in property of the plasma dictate that many of the interesting magnetospheric phenomena observable from the Earth's surface either influence or are influenced by the state of the plasma sheet. In particular, the plasma particles that enter the atmosphere and cause aurora typically originate in the plasma sheet. This is also the reason that the aurora is usually observable only in the far north and south: the magnetic field lines passing through the plasma sheet map to higher latitudes.

1.2.2 Reconnection in the magnetotail

Magnetic reconnection [10] is a physical process where the magnetic field lines rearrange their configuration, releasing the stored magnetic energy. During reconnection, previously unconnected field lines connect to each other, while previously connected field lines separate. The simplest magnetic field configuration conductive to magnetic reconnection is that of antiparallel magnetic fields, where a thin current sheet separates the fields. Magnetic field lines in such a configuration are easily disturbed (through some instability) and moved closer to each other, dramatically increasing the local gradient of the magnetic field; a small portion of the magnetic flux can diffuse through the current sheet, and the magnetic field lines appear to be cut and reconnected in a different configuration (see figure 1.4). In the new configuration the magnetic field lines are under a large amount of tension. As the tension is released, the magnetic field lines move outward from the point of reconnection (in 3D, the reconnection can occur along a line, known as an *X-line* or a *neutral line*), carrying plasma in burst flows (*jets*). (For more details on reconnection see, e.g., Biskamp [10].)

As mentioned in the previous section, the solar wind plasma, carrying with itself the solar magnetic field lines, collides with the Earth's magnetic field and is deflected around it. The details of the subsequent development have been described by, e.g., Baumjohann & Treumann [9]; here, we will present an abridged version.

The interplanetary magnetic field (IMF) is carried with the solar wind, as

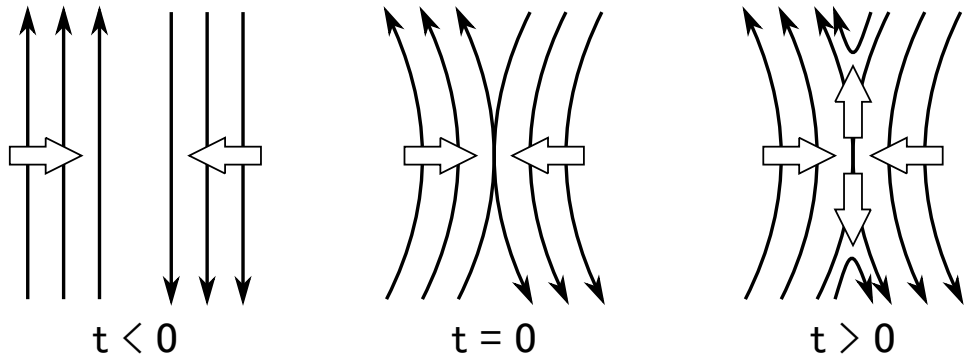

Figure 1.4: The process of magnetic reconnection; diagram based on figure 5.3 from Baumjohann & Treumann [9]. At time $t < 0$ (left), the two plasmas with antiparallel field lines begin moving towards each other. At time $t = 0$ (center), the plasmas meet. If there is any diffusion across the field lines, the magnetic field may vanish at a point of contact ("neutral point"), cutting the field lines which then get reconnected in a different configuration. As the process continues at time $t > 0$ (right), the plasma flow carries the magnetic field towards the neutral point, where the field lines reconnect, expelling the plasma outwards as the field lines relax into a new configuration.

it radiates away from the Sun at supersonic and super-Alfvénic velocity. Due to the Sun's 27-day rotation, the field lines of the IMF are twisted into a spiral configuration. Where the solar wind impacts the Earth's magnetosphere, the frozen-in IMF field lines it carries can be either north-facing or south-facing. As the Earth's magnetic field at the point of contact always faces north, this means that the IMF magnetic field faces south, the field lines at the point of contact will be facing opposite directions, and there will be a merging and *reconnection* of magnetic field lines on the dayside magnetopause. One side of the merged field lines stays anchored to the Earth, while the other side keeps being carried by the solar wind.

After the dayside reconnection, the merged Earth–IMF magnetic field lines are carried with the solar wind towards the magnetotail. At the far end of the magnetotail, at a distance of approximately 100–200R_{E}, the connected Earth–IMF field lines reconnect once more, restoring both the closed Earth field line and the open IMF field line. The tailwise transport of the Earth field line stretches out the magnetic field, creating the so-called *tail-like* configuration (see figure 1.2). As the newly released field line relaxes its magnetic tension, it generates an Earthward plasma flow, and eventually returns to the dayside magnetopause ready for another cycle.

The convection of magnetic field lines from magnetotail back to the dayside does not occur at a uniform rate. As the field lines are released after distant tail reconnection, a part of the magnetic flux stays in the magnetotail, building up and increasing the density of the tail magnetic field lines (i.e., the strength of the magnetic field). The resulting development of the magnetosphere is depicted in figure 1.5. Once the built up flux passes a certain (variable) threshold, the built up flux suddenly gets released in an explosive reconnection, creating a temporary *near-Earth neutral line* (NENL), located at 20–30R_{E}. The near-Earth reconnection has a strong effect on magnetospheric conditions, including the auroral strength, and has been dubbed the *magnetospheric substorm*. [1] The NENL starts moving tailward, and eventually becomes the new distant

[1] Occasionally, magnetospheric substorms are precursors to a much stronger disturbance called the *magnetospheric storm*, the details of which are outside of scope of this thesis; see, e.g., Baumjohann & Treumann [9].

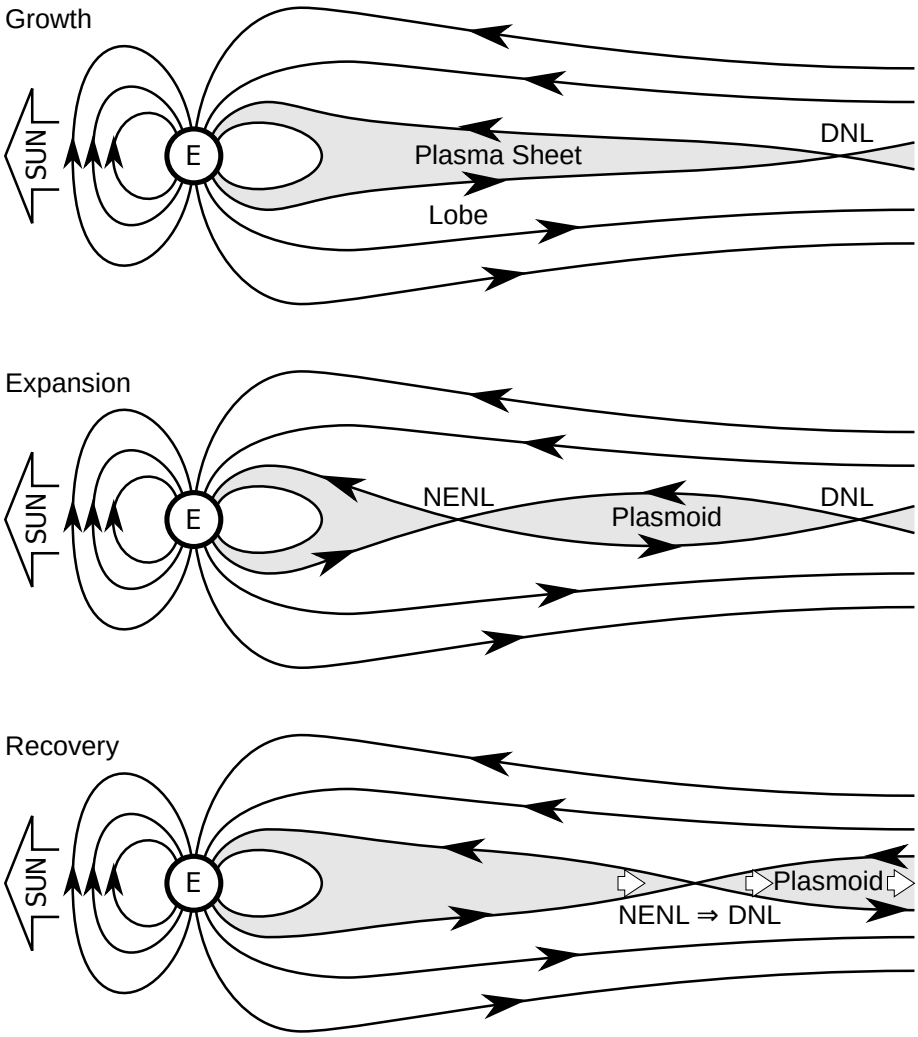

Figure 1.5: Tail reconnection and change in the plasma sheet configuration during a magnetospheric substorm; diagram based on figure 5.11 from Baumjohann & Treumann [9]. During the growth phase (top), the reconnection at the DNL causes a build up of the magnetic flux inside of the plasma sheet. After enough flux is transported inwards, the expansion phase (center) starts and the NENL forms, generating a plasmoid between the two neutral lines. The NENL is pushed tailwards in the recovery phase (bottom), expelling the plasmoid into interplanetary space and taking the place as the new DNL.

neutral line (DNL). After the near-Earth reconnection, the previous DNL is no longer connected to the Earth and is free to be pushed out and released into interplanetary space, carrying with it a portion of magnetospheric plasma.

The signature of the near-Earth reconnection and the formation of the NENL has been observed by the satellites. Figure 1.6 shows the observational data the Geotail satellite took as it was passing close to the location where a neutral line formed, presented by Asano *et al.* [11]. Between times of 11:55 and 12:05, the satellite observed large changes in the plasma sheet properties, consistent with the behavior during reconnection. The density fell, accompanied by a rise in ion and electron temperatures. There was also a large increase in plasma flow velocity, with a large difference between ion and electron components. The velocity moments were used to determine the structure of the current sheet (region of strong current in the inner plasma sheet) around the NENL, with the analysis showing that the thickness of the current sheet is reduced to around 500 km, compared to the local ion inertial length of ~ 720 km. A Hall current system [9], which typically forms around a neutral line, is also present.

Note that in this thesis, the magnetotail reconnection itself is not modeled, as it is not possible for it to occur under the ideal MHD model we will be using (see Chapter 2).

1.2.3 Cross tail current disruption

Around the time of the formation of the NENL at 20–30R_{E}, the near-Earth cross tail current also experiences a strong disturbance [12] at a distance of around 10R_{E} down the magnetotail. The cross tail current, which is aligned with the equatorial plane, forms a so-called *substorm current wedge* [9]; it is diverted on the morning side to flow along the magnetic field lines into the ionosphere, returning back to the plasma sheet on the evening side.

Satellite observations of current disruption are numerous; see, for example, Takahashi *et al.* [13], Lui *et al.* [14], Tang *et al.* [15]. Figure 1.7 shows a current disruption event in March 2008 as observed by the satellite P2 of the THEMIS constellation, reproduced from figure 7 in the paper by Tang *et al.* [15]. Plotted

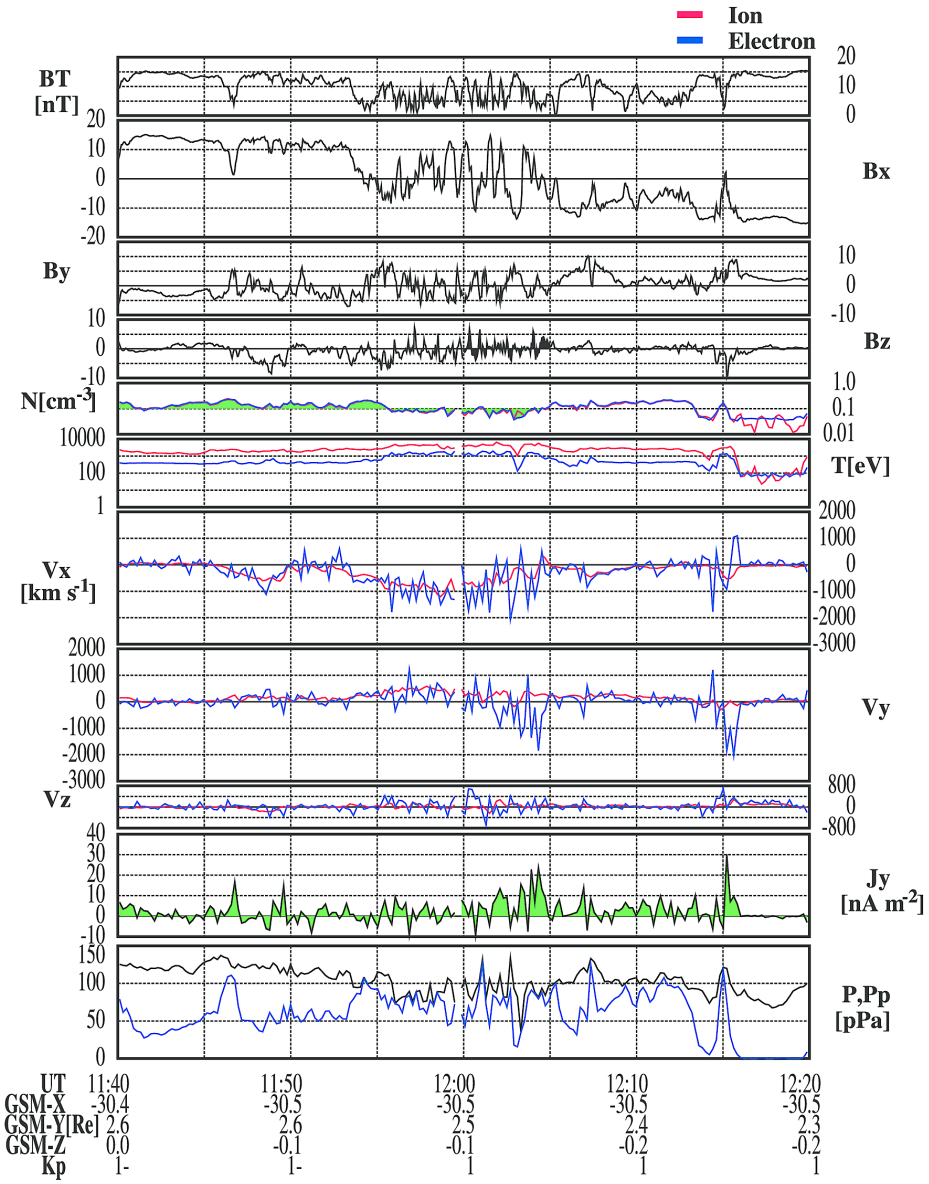

Figure 1.6: Observational data of an NENL event, taken by the Geotail satellite. Plotted values are the total magnetic field BT and it's components B_x, B_y, and B_z (where x points sunward, and z points north); numerical density N, temperature T, and the three velocity components v_x, v_y, and v_z of the plasma; the cross tail current density j_y; and the total pressure P (black) and thermal pressure Pp (blue). Where available, separate values for ions (red) and electrons (blue) are shown. Figure taken from Asano *et al.* [11]; see the referenced paper for detailed discussion.

values are the magnetic field components B_x, B_y, and B_z (where x points sunward, and z points north); the elevation of the magnetic field θ (where 0° is tail-like, and 90° is dipolar); pulses in B_z in the period range of 40–150 s; ion velocity components v_x (black solid line) and v_z (red dotted line); magnetic pressure P_{m} (black solid line), kinetic (thermal) pressure P_{th} (blue dashed line), and total pressure P_{t} (red dotted line); plasma beta β; energy spectra of ions and electrons, obtained by two separate instruments. The vertical solid line denotes the onset of flux pileup, while the vertical dashed line denotes the onset of current disruption. As the cross-tail current is not observed directly, the disruption event has to be inferred, mainly from the behavior of the magnetic field. Here, a sharp decrease in $|B_x|$ around 11:11 marks the start of the current disruption near the satellite's location. This sudden drop in $|B_x|$ is accompanied by an equally sudden increase in average energy of ions and electrons, plasma kinetic pressure, and plasma beta, as well as plasma density and temperature (not shown). At the same time, there is a drop in magnetic pressure and total pressure. These changes are taken to be a clear indicator of current disruption.

Near-Earth magnetotail reconnection and current disruption are connected, though exact causal relationship is so far unknown, and the mechanism behind the magnetotail current disruption has not yet been conclusively determined. One possible explanation [9] is that the magnetic flux carried by the Earthward plasma flow generated by the formation of the NENL (see the following section) piles up in the inner magnetosphere, where the magnetic field lines change from a stretched-out, tail-like configuration, into a dipole configuration. The flux pileup causes the depolarization of the tail magnetic filed, which also reduces the cross-tail current in that region; the excess current trying to move through is forced to divert into the ionosphere as field aligned currents.

Some of the other candidate models for current disruption, which do not require the NENL to form beforehand, are the magnetosphere–ionosphere coupling (MIC) model and the Ballooning Instability (BI) model [12]. In the MIC model [16], the dayside reconnection launches an Alfvén wave into the nightside plasma sheet, where the current in the wave interacts with the cross tail

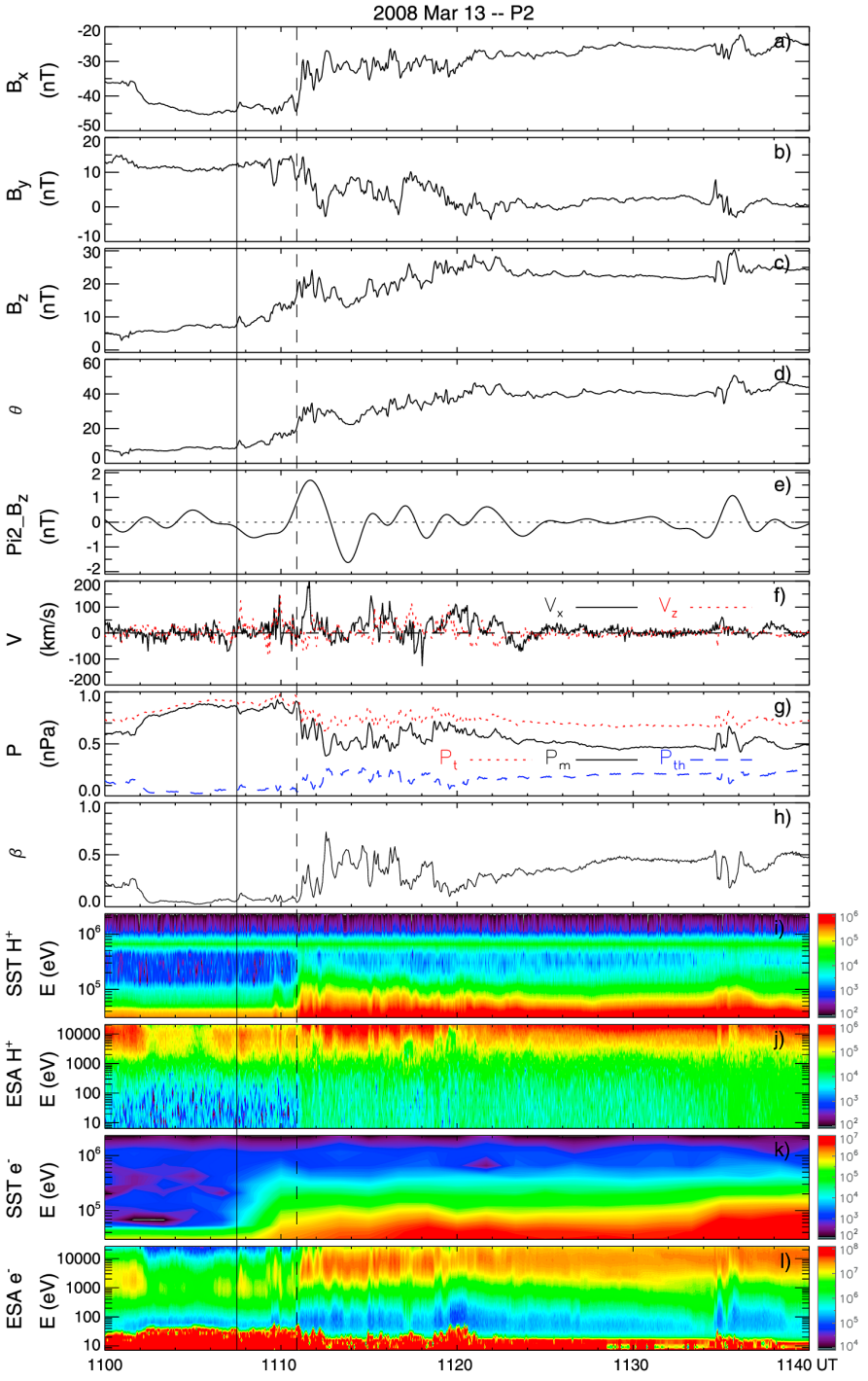

Figure 1.7: Observational data of a current disruption event, taken by one of the THEMIS satellites. Plotted values are described in the main text. Figure taken from Tang *et al.* [15]; see the referenced paper for detailed discussion.

current, reducing it. This interaction bounces the Alfvén wave into ionosphere, which bounces it right back, further disturbing the current, and so on; the positive feedback creates an instability and diverts the current into the ionosphere.

According to the BI model [17], the transition in magnetic field configuration from tail-like to dipolar is analogous to a heavy fluid resting on top of a light fluid; therefore, the configuration is vulnerable to the development of a Rayleigh–Taylor instability. As the ballooning modes grow due to the instability, they cause growth of polarization electric fields, resulting in a charge buildup in the region. Neutralizing the excess charge causes the field aligned currents to form.

1.2.4 Auroral breakup

During *magnetic substorms*, periods of intense geomagnetic activity, a sudden and dramatic increase in auroral strength can sometimes be observed [1]. This event is called *auroral breakup*, or *auroral explosion*, and the mechanism behind it is not yet entirely understood. There are certain sub-events that are known to occur during or before auroral breakup [18] (see figure 1.8), namely,

(a) magnetotail reconnection,

(b) cross tail current reduction, and

(c) auroral breakup itself.

However, the exact order of these events, and therefore their precise causal relationship, has not yet been conclusively determined. The two primary competing models that try to explain these events and how they relate to each other are the Near-Earth Neutral Line (NENL) model [5] and the Current Disruption (CD) model [6].

Near-Earth Neutral Line model

In the Near-Earth Neutral Line model, a disturbance in the magnetotail, caused by the solar wind, induces a reconnection of the stretched-out, antiparallel magnetic field lines (sub-event (a)). The magnetic reconnection is

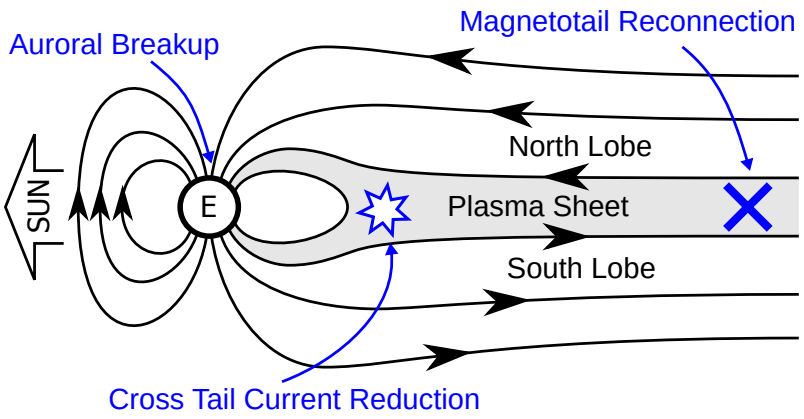

Figure 1.8: Approximate relative locations of the sub-events (marked in blue) related to auroral breakup. The cross tail current reduction occurs at a distance of $\sim$ 6–10R_{E} tailward from the Earth [2] The tail reconnection takes place at a distance of $\sim$ 20–30R_{E}. The auroral breakup itself occurs in the upper regions of the atmosphere.

a high-energy event which creates jets of plasma that flow Earthward and tailward. The passage of the Earthward jet causes a decrease in the cross tail current (sub-event (b)), and finally the jet enters the high-latitude atmosphere, where it causes the auroral breakup (sub-event (c)).

The NENL model has been simulated frequently; for example, a cursory search of the literature has revealed papers from 1981 by Lyon *et al.* [19], with a 2D global MHD simulation, to 1993 by Walker *et al.* [20] and 2010 by Tanaka *et al.* [21], both with a 3D global MHD simulation.

Current Disruption model

In the Current Disruption model, first the cross tail current is reduced (sub-event (b)) through, as the name indicates, a current disruption instability. As a result, the balance of the near-Earth magnetotail plasma is broken, and the resulting plasma flow enters the high-latitude atmosphere and causes the auroral breakup (sub-event (c)).

On the opposite side, the plasma loss in the magnetotail induces a rarefaction wave that starts propagating tailward through the plasma sheet (figure 1.9). The passage of the rarefaction wave causes the plasma sheet pressure

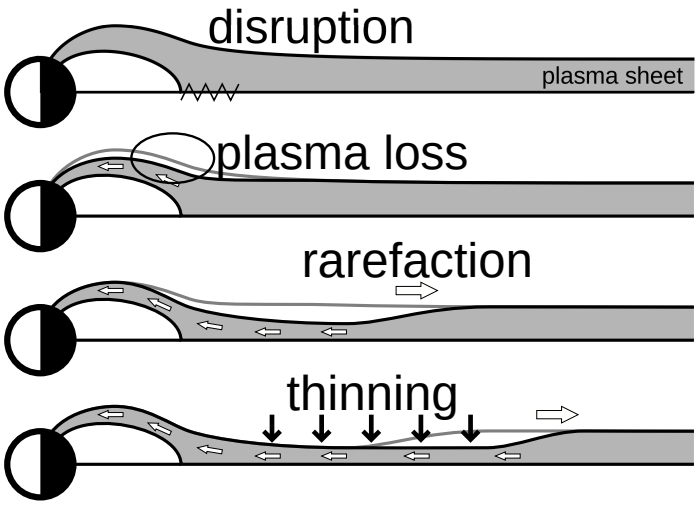

Figure 1.9: The process of plasma sheet thinning as described by the CD model. Image adapted from Chao *et al.* [7].

to drop, the sheet–lobe boundary moves inward, and plasma sheet thickness is reduced. As the antiparallel magnetic field lines move closer to each other, they eventually trigger the magnetotail reconnection (sub-event (a)).

It may be worth pointing out that while there is a strict ordering to the sub-events in the NENL model, in the CD model the auroral breakup and magnetotail reconnection are not parts of the same causal chain. While both sub-events are caused by the same precursor, their relative ordering is not determinable.

A possible mechanism by which the disruption of the cross-tail current may generate an Earthward flow of plasma is presented by Shiokawa *et al.* [22], based on the analysis of the observational data from the Geotail satellite. The mechanism is summarized in figure 7 of Shiokawa *et al.* [22], reproduced here (with minor edits) in figure 1.10. The steps are as follows. (a) During calm periods, the extended, tail-like configuration of the magnetic field lines is supported by the plasma pressure gradient $-\boldsymbol{\nabla} p$ (pushing the plasma tailward) acting against the Lorentz force $\mathbf{j} \times \mathbf{B}$ (pushing the plasma Earthward). (b) The growth phase of the substorm strengthens the cross-tail current, further enhancing the tail-like nature of the magnetic field in the near-Earth region. (c) However, the intense effects of a substorm cause an instability, possibly

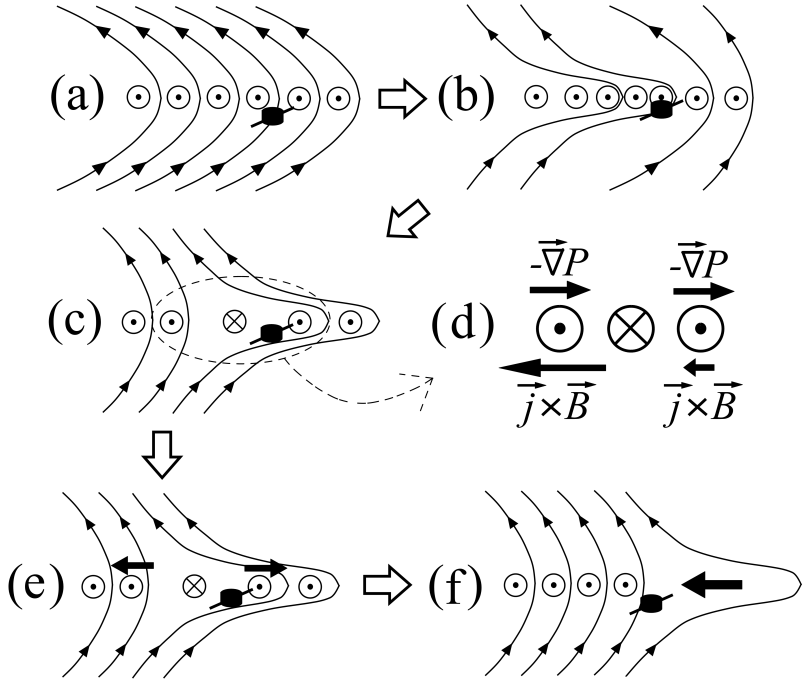

Figure 1.10: A possible mechanism by which an Earthward flow of plasma can be caused by the disruption of near-Earth cross-tail current; image taken from Shiokawa [22]. The steps (a) to (f) are explained in the main text.

by one of the mechanisms introduced above; (d) a localized disruption reduces the cross-tail current, strengthening the magnetic field on the Earth side of the disruption, and weakening it on the tail side. (e) The changes in the Lorentz force break the balance, generating a plasma flow inwards and outwards, away from the disruption. (f) Finally, the plasma loss due to the Earthward flow reduces the plasma pressure gradient, which causes the entire plasma to flow Earthward, initiating the auroral breakup in the upper atmosphere (and, presumably, the thinning of the plasma sheet in the magnetotail).

Note that, unlike the more popular NENL model, an extended search of literature has not surfaced any direct simulations of the CD model. The only relevant paper we were able to find is a 1977 paper by Chao *et al.* [7], which uses an extremely simplified 1D model of the plasma sheet.

Observations

The primary difficulty with determining which of the candidate models (if any) is the correct one is the sheer scale of the problem. While there is observational data for specific sub-events: the current disruption [12, 14, 22], the plasma flow, the change in direction of the magnetic field, and what appears to be the formation of the near-Earth neutral line [11]; the distances involved are such that the most we can obtain is point data at the location of a satellite that is by chance passing by. However, both of the above models involve a large-scale disturbance and reconfiguration of the plasma sheet and the surrounding magnetic field.

As an example, detecting a thinning of the plasma sheet would require finding out the location and time evolution of the sheet–lobe boundary over a distance of 10–20R_{E} during a period of $\sim$ 10 minutes. However, with a point observation from a moving platform, we are only able to detect the magnetic field strength and particle density at a certain location in the magnetotail. If there is a sudden drop in density and the magnetic field, it may signify that the thinning front moved over the satellite, albeit whether the propagation is Earthward or tailward is unknowable without additional points of observation. On the other hand, as the sheet is not stationary, that particular observation

may also signify that the entire sheet moved southwards or northwards, without any thinning at all. We can conclude that the direct observation of thinning would require wide-area detection instruments far beyond the current technology level and/or orders of magnitude larger budgets for satellite launches, neither of which are presently available. The models of plasma sheet thinning have to build on the fragmentary observations currently obtainable, filling in the missing pieces with theoretical analysis; the NENL model and the CD model introduced above are two examples of such analysis.

Nevertheless, the science slowly marches on. About a decade ago, the THEMIS mission [8] tried to determine which of these two models is the one explaining the auroral substorms and the related auroral breakup. Satellite part of the THEMIS mission is composed of five identical satellite probes distributed and coordinated in the tail of the magnetosphere, which enables us to observe the disturbances in the magnetotail leading to the auroral substorm. To support the satellite observations in space, a number of all-sky cameras were deployed in North America to observe the signature of auroral breakup at the magnetic footprints of the satellites [23]. By using the data obtained by the THEMIS mission, Angelopoulos *et al.* [24] demonstrated an event in which reconnection took place at $-20R_{\mathrm{E}}$ a few minutes earlier than the signature of current disruption at $\sim -10R_{\mathrm{E}}$. This observation supports the NENL model, that is, that auroral substorms are initiated by reconnection in the magnetotail. Later, however, Lui [25] claimed that multi-satellite observations during the same interval can be interpreted based on the CD paradigm. Thus, it is still controversial which of these two models better explains the development of the magnetotail disturbances before auroral breakups, and can be regarded as the dominant triggering mechanism of substorms.

Chapter 2

Ideal MHD model

To describe plasma in a precise, physically correct way would require solving a kinetic equation for the particle distribution function over the entire phase space (three spatial and three velocity dimensions). However, this approach is extremely computationally expensive, and the results are more detailed than is necessary in many cases. In physical domains such as the plasma sheet, we are more often interested in large-scale features of the plasma, including its velocity, density, and pressure.

2.1 Ideal MHD equations

In the magnetohydrodynamic (MHD) model, plasma is treated as an ionized fluid. The MHD equations are obtained by integrating the Vlasov equation over the velocity space for each component particle species (multi-fluid theory) and combining them with the Maxwell's equations of electrodynamics [9]. To obtain single-fluid MHD equations, there is a further assumption that there are only two relevant species, electrons and protons, with equal charge densities (*quasi-neutrality*), and the equations can be expressed for the center of mass of the two fluids [9, 26]. By neglecting the viscosity, thermal conductivity, and resistivity [27, 28], and assuming slow variations (neglecting the displacement

current), we can obtain the *ideal MHD equations*,

$$\frac{\partial \rho}{\partial t} + \boldsymbol{\nabla} \cdot (\rho \mathbf{u}) = 0, \tag{2.1}$$

$$\frac{\partial \mathbf{u}}{\partial t} + \mathbf{u} \cdot \boldsymbol{\nabla} \mathbf{u} + \frac{1}{\rho} \boldsymbol{\nabla} p - \frac{1}{\mu_0 \rho} (\boldsymbol{\nabla} \times \mathbf{B}) \times \mathbf{B} = 0, \tag{2.2}$$

$$\frac{\partial p}{\partial t} + \mathbf{u} \cdot \boldsymbol{\nabla} p + \gamma p \boldsymbol{\nabla} \cdot \mathbf{u} = 0, \tag{2.3}$$

$$\frac{\partial \mathbf{B}}{\partial t} - \boldsymbol{\nabla} \times (\mathbf{u} \times \mathbf{B}) = 0, \tag{2.4}$$

$$\boldsymbol{\nabla} \cdot \mathbf{B} = 0, \tag{2.5}$$

where ρ is the density, p is the kinetic pressure, $\mathbf{u} = (u, v, w)$ is the velocity vector, $\mathbf{B} = (B_x, B_y, B_z)$ is the magnetic field vector, γ is the ratio of specific heats, and μ_0 is the magnetic permeability of vacuum.

For the CD model of the auroral breakup in the Earth's plasma sheet, we can describe three distinct phases of development. First is the current disruption phase, which is possibly dominated by the small-scale kinetic effects outside the scope of the MHD theory [12]. Second is the rarefaction wave phase, where the spatial scale is long, and temporal variations are slow; the ideal MHD approximation is justified for this phase. Finally, the third phase is the reconnection phase; since under the ideal MHD theory the magnetic filed lines can never cross each other, that theory is, again, inapplicable. Therefore, the ideal MHD model can be safely used only for the middle phase: after the current disruption is over, and until the reconnection begins.

2.2 Conservation laws

A conservation law states that some physical quantity does not change with time; for example, a conservation of mass or conservation of momentum. These quantities are often called *conserved variables* (e.g., momentum, energy), in contrast to *primitive* or *physical variables* (e.g., velocity, pressure). It is often beneficial to form a system of equations in terms of conserved variables, as it unlocks a wide range of numerical methods and analysis approaches [29].

Conservation laws stated in differential form in full three dimensions (3D)

are

$$\frac{\partial \mathbf{U}}{\partial t} + \frac{\partial \mathbf{F}}{\partial x} + \frac{\partial \mathbf{G}}{\partial y} + \frac{\partial \mathbf{H}}{\partial z} = 0, \tag{2.6}$$

with state vector $\mathbf{U} = \mathbf{U}(x, y, z, t)$ and fluxes $\mathbf{F} = \mathbf{F}(\mathbf{U}), \mathbf{G} = \mathbf{G}(\mathbf{U}), \mathbf{H} = \mathbf{H}(\mathbf{U})$ in x, y, z directions.

In 1D systems, we assume that physical properties vary only in the x direction, while being homogeneous in y and z directions. This significantly reduces the complexity of the problem and allows us to considerably simplify the PDEs describing it. Conservation laws in 1D reduce to

$$\frac{\partial \mathbf{U}}{\partial t} + \frac{\partial \mathbf{F}}{\partial x} = 0 \tag{2.7}$$

with $\mathbf{U} = \mathbf{U}(x, t)$ and a single flux $\mathbf{F} = \mathbf{F}(\mathbf{U})$ in the x direction. Using the Jacobian matrix

$$A(\mathbf{U}) = \frac{\partial \mathbf{F}}{\partial U} = \begin{bmatrix} \frac{\partial F_1}{\partial U_1} & \cdots & \frac{\partial F_1}{\partial U_k} \\ \vdots & \ddots & \vdots \\ \frac{\partial F_k}{\partial U_1} & \cdots & \frac{\partial F_k}{\partial U_k} \end{bmatrix}, \tag{2.8}$$

where k denotes the size of the state vector $\mathbf{U}$, we can rewrite equation (2.7) as

$$\frac{\partial \mathbf{U}}{\partial t} + A(\mathbf{U})\frac{\partial \mathbf{U}}{\partial x} = 0. \tag{2.9}$$

If all of the eigenvalues of the Jacobian matrix $A(\mathbf{U})$ are real and it has a complete set of right eigenvectors, then we say that the system (2.9) is hyperbolic [29].

2.3 Ideal MHD equations as a conservation law

Formulation in 3D

We use the ideal MHD equations in their formulation as a system of conservation laws [30]. A system of conservation laws in 3D can be represented as

$$\frac{\partial \mathbf{U}}{\partial t} + \frac{\partial}{\partial x}\mathbf{F}(\mathbf{U}) + \frac{\partial}{\partial y}\mathbf{G}(\mathbf{U}) + \frac{\partial}{\partial z}\mathbf{H}(\mathbf{U}) = 0, \tag{2.10}$$

where $\mathbf{U}$ is a vector of conserved variables and $\mathbf{F}(\mathbf{U})$, $\mathbf{G}(\mathbf{U})$, and $\mathbf{H}(\mathbf{U})$ are respectively fluxes in x, y, and z directions. For the ideal MHD system, the conserved variables are

$$\mathbf{U} = (\rho, \rho u, \rho v, \rho w, B_x, B_y, B_z, e)^\intercal, \tag{2.11}$$

where ρ is the density, $\mathbf{u} = (u, v, w)$ is the velocity vector, $\mathbf{B} = (B_x, B_y, B_z)$ is the magnetic field vector, and e is the total energy density. Manipulating the equations (2.1)–(2.5) into the conservation form (2.10), the fluxes in (2.10) become

$$\mathbf{F}(\mathbf{U}) = \begin{bmatrix} \rho u \\ \rho u u - \frac{1}{\mu_0} B_x B_x + p_{\text{total}} \\ \rho v u - \frac{1}{\mu_0} B_x B_y \\ \rho w u - \frac{1}{\mu_0} B_x B_z \\ 0 \\ B_y u - B_x v \\ B_z u - B_x w \\ u(e + p_{\text{total}}) - \frac{1}{\mu_0} B_x (\mathbf{u} \cdot \mathbf{B}) \end{bmatrix}, \tag{2.12}$$

$$\mathbf{G}(\mathbf{U}) = \begin{bmatrix} \rho v \\ \rho u v - \frac{1}{\mu_0} B_y B_x \\ \rho v v - \frac{1}{\mu_0} B_y B_y + p_{\text{total}} \\ \rho w v - \frac{1}{\mu_0} B_y B_z \\ B_x v - B_y u \\ 0 \\ B_z v - B_y w \\ v(e + p_{\text{total}}) - \frac{1}{\mu_0} B_y (\mathbf{u} \cdot \mathbf{B}) \end{bmatrix}, \tag{2.13}$$

$$\mathbf{H}(\mathbf{U}) = \begin{bmatrix} \rho w \\ \rho u w - \frac{1}{\mu_0} B_z B_x \\ \rho v w - \frac{1}{\mu_0} B_z B_y \\ \rho w w - \frac{1}{\mu_0} B_z B_z + p_{\text{total}} \\ B_x w - B_z u \\ B_y w - B_z v \\ 0 \\ v(e + p_{\text{total}}) - \frac{1}{\mu_0} B_z (\mathbf{u} \cdot \mathbf{B}) \end{bmatrix}, \tag{2.14}$$

where $\mu_0 = 4\pi \times 10^{-7}$ H m^{-1} is the magnetic permeability of vacuum, and total pressure p_{total} is

$$p_{\text{total}} = p + \frac{1}{2\mu_0} \mathbf{B} \cdot \mathbf{B} \tag{2.15}$$

with pressure p defined as

$$p = (\gamma - 1) \left(e - \frac{1}{2} \rho \mathbf{u} \cdot \mathbf{u} - \frac{1}{2\mu_0} \mathbf{B} \cdot \mathbf{B} \right), \tag{2.16}$$

where γ is the ratio of specific heats.

Formulation in 2D

The formulation of conservation law in 2D is

$$\frac{\partial \mathbf{U}}{\partial t} + \frac{\partial}{\partial x} \mathbf{F}(\mathbf{U}) + \frac{\partial}{\partial y} \mathbf{G}(\mathbf{U}) = 0, \tag{2.17}$$

where the fluxes $\mathbf{F}(\mathbf{U})$ and $\mathbf{G}(\mathbf{U})$ are the same as in the formulation in 3D.

Formulation in 1D

The formulation of conservation law in 1D is

$$\frac{\partial \mathbf{U}}{\partial t} + \frac{\partial}{\partial x} \mathbf{F}(\mathbf{U}) = 0, \tag{2.18}$$

and the divergence condition (2.5) dictates that B_x must be constant in space. The component equation for B_x becomes $\partial B_x / \partial t = 0$, and the system can be reduced to seven variables,

$$\mathbf{U}' = (\rho, \rho u, \rho v, \rho w, B_y, B_z, e)^\intercal, \tag{2.19}$$

with a seven-component flux

$$\mathbf{F}'(\mathbf{U}') = \begin{bmatrix} \rho u \\ \rho u u - \frac{1}{\mu_0} B_x B_x + p_{\text{total}} \\ \rho v u - \frac{1}{\mu_0} B_x B_y \\ \rho w u - \frac{1}{\mu_0} B_x B_z \\ B_y u - B_x v \\ B_z u - B_x w \\ u(e + p_{\text{total}}) - \frac{1}{\mu_0} B_x (\mathbf{u} \cdot \mathbf{B}) \end{bmatrix} \tag{2.20}$$

in the x direction.

2.4 Normalization

To further simplify the formulation (and ease the implementation), we normalize the equations by scaling all quantities φ by their respective normalization parameters, $\varphi = \hat{\varphi}\bar{\varphi}$, where $\bar{\varphi}$ are the normalized quantities, and the constants $\hat{\varphi}$ are the normalization parameters. Specifically, the normalization parameters for the ideal MHD equations are

$$\begin{aligned} &\rho = \hat{\rho}\bar{\rho}, \quad u = \hat{u}\bar{u}, \quad B_x = \hat{B}_x\bar{B}_x, \quad x = \hat{x}\bar{x}, \\ &e = \hat{e}\bar{e}, \quad v = \hat{v}\bar{v}, \quad B_y = \hat{B}_y\bar{B}_y, \quad y = \hat{y}\bar{y}, \\ &p = \hat{p}\bar{p}, \quad w = \hat{w}\bar{w}, \quad B_z = \hat{B}_z\bar{B}_z, \quad z = \hat{z}\bar{z}, \\ &t = \hat{t}\bar{t}. \end{aligned} \tag{2.21}$$

Substituting (2.21) into MHD equations, we obtain the constraints that the parameters must satisfy. First set of constraints,

$$\hat{x} = \hat{y} = \hat{z}, \tag{2.22}$$

$$\hat{u} = \hat{v} = \hat{w}, \tag{2.23}$$

$$\hat{B}_x = \hat{B}_y = \hat{B}_z = \sqrt{\mu_0 \hat{p}}, \tag{2.24}$$

$$\hat{p} = \hat{e}, \tag{2.25}$$

defines parameter groups, while the second set,

$$\hat{x} = \hat{u}\hat{t}, \tag{2.26}$$

$$\hat{p} = \hat{\rho}\hat{u}^2, \tag{2.27}$$

defines relationships between them. The parameter groups are distance, velocity, energy, density, and time. Here, energy is strongly coupled with magnetic field (2.24) and pressure (2.25). We can choose three of the parameters from (2.26)–(2.27) as free parameters, with the other two as dependents.

We define $\bar{\mathbf{U}}$ as a vector of *normalized* conserved variables, and $\bar{\mathbf{F}}(\bar{\mathbf{U}})$ and $\bar{\mathbf{G}}(\bar{\mathbf{U}})$ as *normalized* fluxes in $\bar{x}$ and $\bar{y}$ *normalized* directions. With this convention, normalized conserved variables in 2D become

$$\bar{\mathbf{U}} = \left(\bar{\rho}, \bar{\rho}\bar{u}, \bar{\rho}\bar{v}, \bar{\rho}\bar{w}, \bar{B}_x, \bar{B}_y, \bar{B}_z, \bar{e}\right)^\intercal . \tag{2.28}$$

Normalized fluxes become

$$\bar{\mathbf{F}}(\bar{\mathbf{U}}) = \begin{bmatrix} \bar{\rho}\bar{u} \\ \bar{\rho}\bar{u}\bar{u} - \bar{B}_x\bar{B}_x + \bar{p}_{\text{total}} \\ \bar{\rho}\bar{v}\bar{u} - \bar{B}_x\bar{B}_y \\ \bar{\rho}\bar{w}\bar{u} - \bar{B}_x\bar{B}_z \\ 0 \\ \bar{B}_y\bar{u} - \bar{B}_x\bar{v} \\ \bar{B}_z\bar{u} - \bar{B}_x\bar{w} \\ \bar{u}(\bar{e} + \bar{p}_{\text{total}}) - \bar{B}_x(\bar{\mathbf{u}} \cdot \bar{\mathbf{B}}) \end{bmatrix}, \tag{2.29}$$

$$\bar{\mathbf{G}}(\bar{\mathbf{U}}) = \begin{bmatrix} \bar{\rho}\bar{v} \\ \bar{\rho}\bar{u}\bar{v} - \bar{B}_y\bar{B}_x \\ \bar{\rho}\bar{v}\bar{v} - \bar{B}_y\bar{B}_y + \bar{p}_{\text{total}} \\ \bar{\rho}\bar{w}\bar{v} - \bar{B}_y\bar{B}_z \\ \bar{B}_x\bar{v} - \bar{B}_y\bar{u} \\ 0 \\ \bar{B}_z\bar{v} - \bar{B}_y\bar{w} \\ \bar{v}(\bar{e} + \bar{p}_{\text{total}}) - \bar{B}_y(\bar{\mathbf{u}} \cdot \bar{\mathbf{B}}) \end{bmatrix}, \tag{2.30}$$

$$\bar{\mathbf{H}}(\bar{\mathbf{U}}) = \begin{bmatrix} \bar{\rho}\bar{w} \\ \bar{\rho}\bar{u}\bar{w} - \bar{B}_z\bar{B}_x \\ \bar{\rho}\bar{v}\bar{w} - \bar{B}_z\bar{B}_y \\ \bar{\rho}\bar{w}\bar{w} - \bar{B}_z\bar{B}_z + \bar{p}_{\text{total}} \\ \bar{B}_x\bar{w} - \bar{B}_z\bar{u} \\ \bar{B}_y\bar{w} - \bar{B}_z\bar{v} \\ 0 \\ \bar{v}(\bar{e} + \bar{p}_{\text{total}}) - \bar{B}_z(\bar{\mathbf{u}} \cdot \bar{\mathbf{B}}) \end{bmatrix}, \tag{2.31}$$

where $\bar{p}_{\text{total}}$ is the total pressure

$$\bar{p}_{\text{total}} = \bar{p} + \frac{1}{2}\bar{\mathbf{B}} \cdot \bar{\mathbf{B}} \tag{2.32}$$

with pressure $\bar{p}$ defined as

$$\bar{p} = (\gamma - 1)\left(\bar{e} - \frac{1}{2}\bar{\rho}\bar{\mathbf{u}} \cdot \bar{\mathbf{u}} - \frac{1}{2}\bar{\mathbf{B}} \cdot \bar{\mathbf{B}}\right). \tag{2.33}$$

In 1D, the vectors of conserved variables $\bar{\mathbf{U}}$ and flux $\bar{\mathbf{F}}$ can be formed by dropping the $\bar{B}_x$ component. For simplicity, we will henceforth drop the bars and refer exclusively to the normalized version of the MHD equations (2.28)–(2.33).

2.5 Galilean invariance

Let the inertial frame K' be moving with constant relative velocity $\mathbf{V}$, $|\mathbf{V}| \ll c$, with respect to the reference frame K. With no loss of generality, we can assume that $\mathbf{V} = (V, 0, 0)$ (figure 2.1). Then, the Galilean transformations for

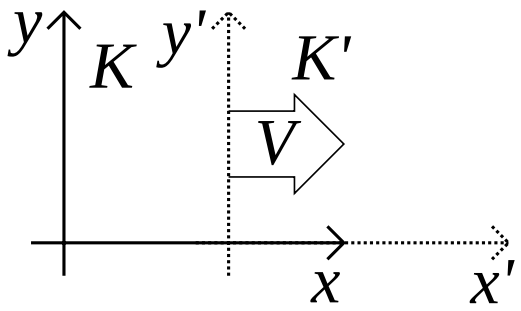

Figure 2.1: Coordinate systems of the reference frame K (solid axes) and inertial frame K' (dotted axes). The inertial frame moves with a constant velocity $\mathbf{V} = (V, 0, 0)$ with respect to the reference frame.

parameters of frame K' and an MHD plasma in that frame are [31]

$$\begin{aligned} t' &= t, \\ (x', y', z') &= (x - Vt, y, z), \\ (u', v', w') &= (u - V, y, z), \\ \rho' &= \rho, \\ p' &= p, \\ \mathbf{B}' &= \mathbf{B}. \end{aligned} \tag{2.34}$$

Expressing $t' = t'(x, y, z, t)$, $x' = x'(x, y, z, t)$, $y' = y'(x, y, z, t)$, and $z' = z'(x, y, z, t)$, we can obtain the partial derivatives of all pairs of coordinates,

$$\begin{aligned} &\partial t'/\partial t = 1, \quad \partial t'/\partial x = 0, \quad \partial t'/\partial y = 0, \quad \partial t'/\partial z = 0, \\ &\partial x'/\partial t = -V, \quad \partial x'/\partial x = 1, \quad \partial x'/\partial y = 0, \quad \partial x'/\partial z = 0, \\ &\partial y'/\partial t = 0, \quad \partial y'/\partial x = 0, \quad \partial y'/\partial y = 1, \quad \partial y'/\partial z = 0, \\ &\partial z'/\partial t = 0, \quad \partial z'/\partial x = 0, \quad \partial z'/\partial y = 0, \quad \partial z'/\partial z = 1. \end{aligned} \tag{2.35}$$

Substituting the above into the partial derivatives of a plasma property φ' in the inertial frame K' with respect to the reference frame K, through the chain rule we obtain

$$\begin{aligned} \frac{\partial \varphi'}{\partial t} &= \frac{\partial \varphi'}{\partial t'}\frac{\partial t'}{\partial t} + \frac{\partial \varphi'}{\partial x'}\frac{\partial x'}{\partial t} + \frac{\partial \varphi'}{\partial y'}\frac{\partial y'}{\partial t} + \frac{\partial \varphi'}{\partial z'}\frac{\partial z'}{\partial t} \\ &= \frac{\partial \varphi'}{\partial t'} - V\frac{\partial \varphi'}{\partial x'}, \end{aligned} \tag{2.36}$$

and with the equivalent calculation

$$\frac{\partial \varphi'}{\partial x} = \frac{\partial \varphi'}{\partial x'}, \quad \frac{\partial \varphi'}{\partial y} = \frac{\partial \varphi'}{\partial y'}, \quad \frac{\partial \varphi'}{\partial z} = \frac{\partial \varphi'}{\partial z'}. \tag{2.37}$$

Taking the density component of the MHD system expressed in the reference frame K,

$$\frac{\partial \rho}{\partial t} + \frac{\partial}{\partial x}(\rho u) + \frac{\partial}{\partial y}(\rho v) + \frac{\partial}{\partial z}(\rho w) = 0, \tag{2.38}$$

and substituting the Galilean transformations in (2.34), we obtain

$$\frac{\partial \rho'}{\partial t} + \frac{\partial}{\partial x}(\rho' u' + \rho' V) + \frac{\partial}{\partial y}(\rho' v') + \frac{\partial}{\partial z}(\rho' w') = 0. \tag{2.39}$$

Applying the chain rules from (2.36) and (2.37), the equation transforms into

$$\frac{\partial \rho'}{\partial t'} - V\frac{\partial \rho'}{\partial x'} + \frac{\partial}{\partial x'}(\rho' u') + V\frac{\partial \rho'}{\partial x'} + \frac{\partial}{\partial y'}(\rho' v') + \frac{\partial}{\partial z'}(\rho' w') = 0, \tag{2.40}$$

that can be simplified into

$$\frac{\partial \rho'}{\partial t'} + \frac{\partial}{\partial x'}(\rho' u') + \frac{\partial}{\partial y'}(\rho' v') + \frac{\partial}{\partial z'}(\rho' w') = 0, \tag{2.41}$$

which is the density component of the MHD system in the inertial frame K'. Comparing equation (2.41) with the density component in the reference frame K from (2.38), it is clear that the density equation is Galilei invariant.

Obtaining the transforms $p_{\text{total}} = p'_{\text{total}}$ and $e = e' + \frac{1}{2}\rho' V^2 + \rho' u' V$, and performing equivalent transformations on the other seven MHD equations, after some simple manipulations it is easily confirmed that all eight MHD equations are Galilei invariant.

2.6 System of equations

A single-component conservation law, where the vector of conserved variables $\mathbf{U}$ consists of a single element, is relatively easy to discretize (see section 3.1.3). Properly extending the aforementioned discretization method to a system of equations (see section 3.1.4) requires the use of the theory of *characteristics*.

2.6.1 Characteristics

Characteristics or *characteristic curves* of a partial differential equation (PDE) of a scalar variable $u(x,t)$ are curves $x = x(t)$ in the t-x plane along which the PDE becomes an ordinary differential equation (ODE) [29]. For the 1D advection equation, which is a PDE of the form

$$\frac{\partial u}{\partial t} + a\frac{\partial u}{\partial x} = 0, \tag{2.42}$$

and taking $x = x(t)$, the rate of change $\mathrm{d}u/\mathrm{d}t$ along the curve $x = x(t)$ is

$$\frac{\mathrm{d}u}{\mathrm{d}t} = \frac{\partial u}{\partial t} + \frac{\mathrm{d}x}{\mathrm{d}t}\frac{\partial u}{\partial x}. \tag{2.43}$$

If we set

$$\frac{\mathrm{d}x}{\mathrm{d}t} = a, \tag{2.44}$$

where a is called the *characteristic speed*, then from the equation (2.43) the rate of change $\mathrm{d}u/\mathrm{d}t$ along the curve $x = x(t)$ becomes zero; in other words, u is constant along the said curve.

2.6.2 Diagonalization

Another concept that will be used in section 3.1.4 to discretize a system of equations is the *diagonalization* of said system.

We define the matrices Λ and R as

$$\Lambda = \begin{bmatrix} \lambda_1 & & 0 \\ & \ddots & \\ 0 & & \lambda_k \end{bmatrix} \quad \text{and} \quad R = (R_1, \ldots, R_k), \tag{2.45}$$

where λ_j $(j = 1, \ldots, k)$ are the eigenvalues, R is a square matrix of order k whose column vectors of k components R_j are the right eigenvectors of the system's Jacobian A, where A is defined by equation (2.8). For a system with one variable the Jacobian A degenerates into the characteristic speed a (see 2.6.1). For a hyperbolic system—which we assume our conservation law to be—all of the right eigenvectors are linearly independent, and consequently the

matrix R is non-singular. Inverting the matrix R, we get the matrix $L = R^{-1}$,

$$L = \begin{bmatrix} L_1 \\ \vdots \\ L_k \end{bmatrix}, \tag{2.46}$$

where L is a square matrix of order k whose the row vectors of k components L_j are the left eigenvectors of the Jacobian matrix A. The matrix L is the inverse of matrix R, $L = R^{-1}$.

Multiplying the Jacobian A from left and right with L and R, respectively, we obtain

$$LAR = \Lambda. \tag{2.47}$$

If the matrices A, Λ, R and L are *constant*, we can use the identity (2.47) to rewrite (2.9) to obtain

$$\begin{aligned} L\frac{\partial \mathbf{U}}{\partial t} + (LAR)L\frac{\partial \mathbf{U}}{\partial x} &= 0 \\ \frac{\partial \mathbf{W}}{\partial t} + \Lambda\frac{\partial \mathbf{W}}{\partial x} &= 0 \end{aligned} \tag{2.48}$$

where $\mathbf{W} = L\mathbf{U}$ is a state vector of *characteristic variables*. It is immediately obvious that (2.48) is a set of k independent advection equations

$$\frac{\partial W_j}{\partial t} + \lambda_j \frac{\partial W_j}{\partial x} = 0, \quad (j = 1, \ldots, k) \tag{2.49}$$

with eigenvalues λ_j as wave speeds (characteristic speeds).

For the 1D normalized ideal MHD equations, with flux (2.20), the wave speeds λ_j are, in non-decreasing order (and independent of the value of β),

$$\begin{aligned} &\lambda_1 = u - c_{\mathrm{fm}},\ \lambda_2 = u - c_{\mathrm{A}},\ \lambda_3 = u - c_{\mathrm{sm}},\ \lambda_4 = u, \\ &\lambda_5 = u + c_{\mathrm{sm}},\ \lambda_6 = u + c_{\mathrm{A}},\ \lambda_7 = u + c_{\mathrm{fm}}, \end{aligned} \tag{2.50}$$

where c_{A} is the Alfvén speed

$$c_{\mathrm{A}} = \sqrt{\frac{B_x^2}{\rho}} \tag{2.51}$$

and c_{fm} and c_{sm} are, respectively, the fast and slow magnetosonic speeds,

$$c_{\mathrm{fm}} = \sqrt{\frac{1}{2}\left[c_{\mathrm{s}}^2 + \frac{\mathbf{B}\cdot\mathbf{B}}{\rho} + \sqrt{\left(c_{\mathrm{s}}^2 + \frac{\mathbf{B}\cdot\mathbf{B}}{\rho}\right)^2 - 4c_{\mathrm{s}}^2 c_{\mathrm{A}}^2}\right]} \tag{2.52}$$

$$c_{\mathrm{sm}} = \sqrt{\frac{1}{2}\left[c_{\mathrm{s}}^2 + \frac{\mathbf{B}\cdot\mathbf{B}}{\rho} - \sqrt{\left(c_{\mathrm{s}}^2 + \frac{\mathbf{B}\cdot\mathbf{B}}{\rho}\right)^2 - 4c_{\mathrm{s}}^2 c_{\mathrm{A}}^2}\right]}, \tag{2.53}$$

with sound speed c_{s} defined as

$$c_{\mathrm{s}} = \sqrt{\frac{\gamma p}{\rho}}. \tag{2.54}$$

Complete sets of right and left eigenvectors of the 1D MHD system are given, respectively, by Brio & Wu [32] and Ryu & Jones [27]. The eigenvectors have been renormalized to remove the singularities.

Note that the eigenvalues of the MHD equations' Jacobian depend on the conserved variables $\mathbf{U}$; the same is true for the matrices A, R and L. Thus, it would appear that the MHD system cannot be decomposed into independent advection equations (2.49). This problem will be addressed in section 3.1.4.

Chapter 3

Simulation code

The simulations in this thesis have been run on a self-developed C++ simulation code, and the results analyzed with an ad-hoc hodge-podge of gnuplot scripts, Perl scripts, and spreadsheets.

3.1 Simulation scheme

The simulation method is constructed in two steps, using the so-called *method of lines*. A 1D PDE for a conserved physical quantity $u(x,t)$ and flux $f(u(x,t))$ is

$$\frac{\partial u}{\partial t} + \frac{\partial f(u)}{\partial x} = 0. \tag{3.1}$$

Leaving the time variable in the MHD equations continuous, we discretize only the spatial derivative,

$$L(u) \approx -\frac{\partial f(u(x,t))}{\partial x}, \tag{3.2}$$

where L is an operator denoting a discretized approximation where the time variable is left continuous. The partially discretized PDE can then be rewritten as

$$\frac{\partial u}{\partial t} = L(u), \tag{3.3}$$

and the time derivative can now also be discretized independently with a suitable time stepping scheme.

3.1.1 Problem properties

The traditional computational schemes (e.g., central finite difference), when applied to conservation laws, reconstruct the numerical flux from a stencil fixed in both space and time. One of the problems with a fixed stencil emerges when there exists a *shock* (discontinuity) in the physical variables. In problems that include shocks, fixed stencils produce solutions with pronounced non-physical oscillations, known as *Gibbs phenomena*.

There are several ways of dealing with Gibbs phenomena. Among those, the Essentially Non-Oscillatory (ENO) schemes for hyperbolic conservation laws introduced by Harten *et al.* [33] are among the most robust, with reasonably sharp shock resolutions, on the order of several computational cells, and no discernible accuracy penalty. Conversely, the relative difficulty of implementation and computational cost of the ENO schemes have to be considered before deciding on their use. Since the goal of this research is to simulate the rarefaction wave in the Earth's plasma sheet, the positive sides of ENO scheme will be necessary, thus the penalties are acceptable.

3.1.2 TVD schemes

Total Variation Diminishing (TVD)—also sometimes known as Total Variation Non-Increasing (TVNI)—schemes [34, 35] are a class of numerical schemes where the *total variation* TV of a discretized variable u, defined as

$$TV(u) = \sum_i |u_{i+1} - u_i|, \tag{3.4}$$

satisfies the condition

$$TV(u^{(n+1)}) \leq TV(u^{(n)}) \tag{3.5}$$

where $TV(u^{(n)})$ is the total variation at time step n.

TVD schemes are convergent and monotonicity preserving. Furthermore, as the total variation is bounded, oscillations such as the Gibbs phenomena are unable to develop. The downside is that the accuracy is limited; linear TVD schemes have first-order accuracy. However, nonlinear TVD schemes such as ENO can have second-order or higher accuracy.

3.1.3 Spatial integration

We consider a scalar conservation law in one space dimension, where the state vector $\mathbf{U}(x,t)$ and its flux $\mathbf{F}(\mathbf{U})$ each contain only a single element, respectively $u = u(x,t)$ and $f = f(u)$. Discretized values of u and f at grid points x_i are denoted with u_i and f_i. As mentioned earlier, in order to calculate the evolution of $u(x,t)$ and $f(u)$ with a numerical method we need a discretized approximation of the spatial derivative $L(u) \approx -\partial f/\partial x$, and we need to obtain it from the discretized values u_i (and, by extension, f_i) at grid points x_i. In section 3.1.5, we will use the values of f at half-grid points $x_{i+\frac{1}{2}}$ to obtain the spatial derivative $L(u)$; in order to obtain these half-grid values, we need to *reconstruct* the flux f. Note that a second order accuracy will be sufficient for the purposes of this thesis.

We first address the general case, and describe the reconstruction procedure [36] for a piecewise polynomial approximation of a scalar function $v(x)$, with discretized values v_i at equidistant grid points x_i. For a second order accuracy, $v_{i+\frac{1}{2}} \approx v(x_{i+\frac{1}{2}})$ is obtained by approximating $v(x)$ with first order polynomials.

Fixed stencil methods

A second order *central finite difference* interpolation to $v_{i+\frac{1}{2}}$ can be obtained with

$$v_{i+\frac{1}{2}} = \frac{1}{2}(v_i + v_{i+1}), \tag{3.6}$$

a *backward finite difference* extrapolation with

$$v_{i+\frac{1}{2}} = \frac{1}{2}(-v_{i-1} + 3v_i), \tag{3.7}$$

and a *forward finite difference* extrapolation with

$$v_{i+\frac{1}{2}} = \frac{1}{2}(3v_{i+1} - v_{i+2}). \tag{3.8}$$

All three of the above approximations, shown in figure 3.1, have one thing in common; namely, the grid points used to calculate them, called *stencil*, are

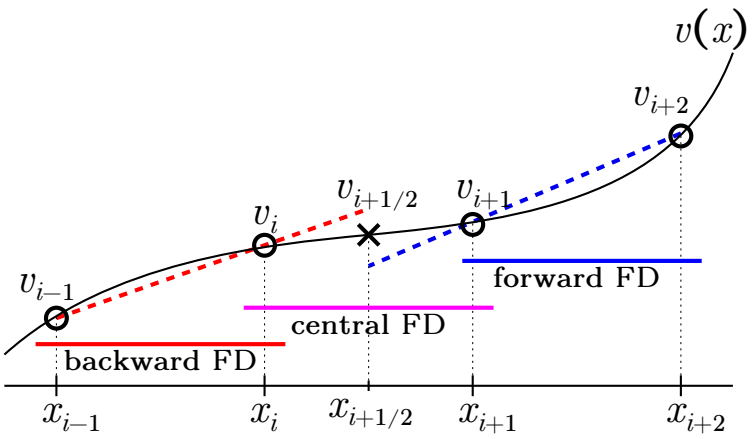

Figure 3.1: Finite difference schemes with a fixed stencil. Backward finite difference (red) approximates $v_{i+\frac{1}{2}}$ with v_{i-1} and v_i, forward finite difference (blue) approximates it with v_{i+1} and v_{i+2}, and central finite difference (purple) approximates it with v_i and v_{i+1}.

fixed and do not depend on the value of v_i. For example, when using the central finite difference approximation, the reconstructed value of $v(x)$ at $x_{i+\frac{1}{2}}$ will always be calculated from discretized values of v at grid points x_i and x_{i+1}.

The strong point of the fixed stencil methods shown above is that they are simple to calculate. Unfortunately, their weak point is that they are stable only for sufficiently smooth function $v(x)$. If $v(x)$ is too steep or, in the extreme case, includes shocks, the fixed stencil methods become unstable and the simulation breaks down. The reconstruction used in this thesis, the Essentially Non-Oscillatory method, addresses this problem by employing a *dynamic* stencil.

ENO reconstruction

The general idea behind the ENO scheme [33, 36] is to consider multiple candidate stencils and choose the smoothest one. Here, smoothness is usually defined through the Newton divided differences,

$$N_{i+\frac{1}{2}} = \frac{v_{i+1} - v_i}{x_{i+1} - x_i}, \tag{3.9}$$

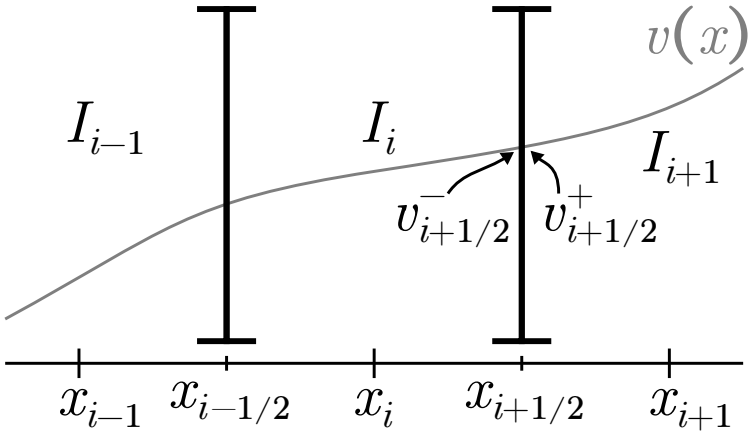

Figure 3.2: ENO reconstruction of function $v(x)$. Cell I_i is centered on grid point x_i. Approximation of $v(x)$ at cell boundary $x_{i+\frac{1}{2}}$ is calculated from the left cell I_i on the minus edge, $v^-_{i+\frac{1}{2}}$, and from the right cell I_{i+1} on the plus edge, $v^+_{i+\frac{1}{2}}$.

which can be replaced by the undivided differences

$$V_{i+\frac{1}{2}} = v_{i+1} - v_i \tag{3.10}$$

if the grid points x_i are equidistant.

We first define cells I_i around grid points x_i as

$$I_i = \left[x_{i-\frac{1}{2}}, x_{i+\frac{1}{2}}\right]. \tag{3.11}$$

In the ENO reconstruction (see figure 3.2), we calculate approximations $v^-_{i+\frac{1}{2}}$ (reconstructed from the left cell, I_i) and $v^+_{i+\frac{1}{2}}$ (reconstructed from the right cell, I_{i+1}) to the function $v(x)$ at all cell boundaries $x_{i+\frac{1}{2}}$.

To achieve second-order accuracy, the function $v(x)$ is approximated from a two-point stencil, somewhat simplifying the procedure presented by Shu [36]. For each cell I_i, we compute the approximations to $v(x)$ on both edges, $v^+_{i-\frac{1}{2}}$ on the left (minus) edge and $v^-_{i+\frac{1}{2}}$ on the right (plus) edge (see figure 3.2).

Similarly to the fixed stencil methods, $v(x)$ in the cell I_i is approximated with a first degree polynomial. We assume $\{v_i\}$ to be the cell average of $v(x)$ inside I_i and compute the undivided differences $V_{i+\frac{1}{2}} = v_{i+1} - v_i$. By comparing the undivided differences we can determine which of the candidate stencils is

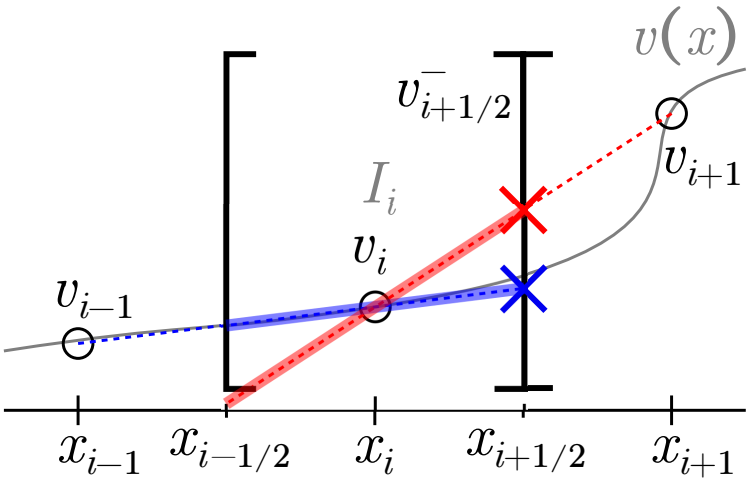

Figure 3.3: ENO stencils of function $v(x)$ for the minus edge $v^-_{i+\frac{1}{2}}$ at grid point $x_{i+\frac{1}{2}}$. The blue and red shaded lines inside cell I_i show the reconstruction of $v(x)$ in I_i as obtained from, respectively, the left and right candidate stencils, while the blue and red crosses show the respective resulting value of $v^-_{i+\frac{1}{2}}$. In the depicted case, the left (blue) stencil is smoother, so it would be the one chosen for the reconstruction, and the value of $v^-_{i+\frac{1}{2}}$ would be as shown by the blue cross.

smoother and compute the approximations of $v(x)$ at the cell boundaries as

$$\begin{aligned}
&\text{if } |V_{i-\frac{1}{2}}| < |V_{i+\frac{1}{2}}| \quad (\text{stencil } \{I_{i-1}, I_i\}) \\
&\qquad \begin{cases} v^+_{i-\frac{1}{2}} &= \frac{1}{2}v_{i-1} + \frac{1}{2}v_i, \\ v^-_{i+\frac{1}{2}} &= -\frac{1}{2}v_{i-1} + \frac{3}{2}v_i; \end{cases} \qquad (3.12) \\
&\text{if } |V_{i-\frac{1}{2}}| \geq |V_{i+\frac{1}{2}}| \quad (\text{stencil } \{I_i, I_{i+1}\}) \\
&\qquad \begin{cases} v^+_{i-\frac{1}{2}} &= \frac{3}{2}v_i - \frac{1}{2}v_{i+1}, \\ v^-_{i+\frac{1}{2}} &= \frac{1}{2}v_i + \frac{1}{2}v_{i+1}, \end{cases} \qquad (3.13)
\end{aligned}$$

where coefficients are equivalent to the ones in backward and forward finite differences, equations (3.7) and (3.8).

An example of the ENO reconstruction procedure for $v^-_{i+\frac{1}{2}}$, the approximation of $v(x)$ at the minus edge of grid point $x_{i+\frac{1}{2}}$ (i.e., inside cell I_i), is depicted in figure 3.3. The blue and red dotted lines show, respectively, the linear polynomial obtained from left and right candidate stencils. The sections of said polynomials that lie inside of the cell I_i are shaded, and represent the segment of a piecewise linear reconstruction of $v(x)$. The value of $v^-_{i+\frac{1}{2}}$ according to each reconstruction is marked with a cross in their respective colors. In the figure, it is clear that undivided difference $|V_{i-\frac{1}{2}}| = |v_i - v_{i-1}|$ is smaller than $|V_{i+\frac{1}{2}}| = |v_{i+1} - v_i|$; therefore, the blue segment is proclaimed "smoother", and the value of $v^-_{i+\frac{1}{2}}$ is taken to be the blue cross, obtained from the left candidate stencil.

Finally, the values of $v^\pm_{i+\frac{1}{2}}$ are used to reconstruct the function $v(x)$ at the cell boundaries. When $v(x)$ is a flux, for stability of the solution, the reconstruction has to use upwinding.

ENO-Roe scheme

The simplest way to upwind the numerical flux is the ENO-Roe version of the ENO scheme, where we upwind by using the *Roe speed* [37]

$$a_{i+\frac{1}{2}} = \frac{f(u_{i+1}) - f(u_i)}{u_{i+1} - u_i}, \qquad (3.14)$$

which is a discretized approximation to $\mathrm{d}f/\mathrm{d}u$. The full procedure of calculating the numerical flux is as follows. First, take $v(x) = f(u(x, t_n))$, where t_n is the current time step, as the continuous function we wish to approximate, and set $v_i = f(u_i)$ as its discretized values. Then, use the ENO reconstruction procedure described above to obtain cell boundary values $v^-_{i+\frac{1}{2}}$ and $v^+_{i+\frac{1}{2}}$. Next, calculate the Roe speed $a_{i+\frac{1}{2}}$ at all cell boundaries $x_{i+\frac{1}{2}}$. Finally, the (upwinded) approximation to the numerical flux $\bar{f}_{i+\frac{1}{2}}$ at cell boundaries $x_{i+\frac{1}{2}}$ can be obtained with

$$\bar{f}_{i+\frac{1}{2}} = \begin{cases} v^+_{i+\frac{1}{2}} & \text{, if } a_{i+\frac{1}{2}} < 0 \\ v^-_{i+\frac{1}{2}} & \text{, if } a_{i+\frac{1}{2}} \geq 0. \end{cases} \tag{3.15}$$

ENO scheme with the Lax-Friedrichs flux splitting

Unfortunately, the ENO-Roe scheme may result in entropy-violating solutions [36]. As a more robust approach, the flux $f(u)$ can be split into a right-moving and left-moving component, $f^+(u)$ and $f^-(u)$, so that

$$f(u) = f^+(u) + f^-(u) \tag{3.16}$$

where

$$\frac{\mathrm{d}f^+(u)}{\mathrm{d}u} \geq 0, \tag{3.17}$$

$$\frac{\mathrm{d}f^-(u)}{\mathrm{d}u} \leq 0. \tag{3.18}$$

(Note that the "+" and "-" superscripts here denote the direction of the flux, and are not to be confused with the superscripts in $v^\pm_{i+\frac{1}{2}}$—shown in figure 3.2—where they denote the plus or minus edge of a cell boundary. While it may be slightly confusing, the notation is reproduced verbatim from the reference paper by Shu [36].) The simplest smooth flux splitting satisfying the above relations is the *Lax–Friedrichs* splitting,

$$f^\pm(u) = \frac{1}{2}(f(u) \pm \alpha u) \tag{3.19}$$

where α is defined as

$$\alpha = \max_u \left| \frac{\mathrm{d}f}{\mathrm{d}u} \right| \tag{3.20}$$

over the relevant range of u; in this case, the relevant range for calculating the numerical flux $\bar{f}_{i+\frac{1}{2}}$ are all of the points in its candidate stencils.

The positive component $\bar{f}^+_{i+\frac{1}{2}}$ of the numerical flux $\bar{f}_{i+\frac{1}{2}}$ is obtained by taking $v(x) = f^+(u(x,t_n))$ as the continuous function to approximate, and setting $v_i = f^+(u_i)$ as its discretization. The cell boundary values $v^-_{i+\frac{1}{2}}$ are, as before, obtained with the ENO reconstruction procedure, and the positive numerical flux $\bar{f}^+_{i+\frac{1}{2}}$ becomes

$$\bar{f}^+_{i+\frac{1}{2}} = v^-_{i+\frac{1}{2}}. \tag{3.21}$$

The negative component $\bar{f}^-_{i+\frac{1}{2}}$ of the numerical flux is obtained in the same way, by taking $v(x) = f^-(u(x,t_n))$ and setting $v_i = f^-(u_i)$, then using the ENO reconstruction to obtain the cell boundary values $v^+_{i+\frac{1}{2}}$. The negative numerical flux becomes

$$\bar{f}^-_{i+\frac{1}{2}} = v^+_{i+\frac{1}{2}}. \tag{3.22}$$

Finally, the positive and negative components are combined into the full numerical flux $\bar{f}_{i+\frac{1}{2}}$ with

$$\bar{f}_{i+\frac{1}{2}} = \bar{f}^+_{i+\frac{1}{2}} + \bar{f}^-_{i+\frac{1}{2}}. \tag{3.23}$$

This thesis uses the ENO scheme with Lax-Friedrichs flux splitting, which we will call the *ENO-LF scheme*. The simulation code also implements the *ENO-Roe scheme*, ENO scheme with Roe speed upwinding.

3.1.4 Extension to systems

Systems of equations can sometimes be solved by applying the above scalar scheme for each component separately, which gives an adequate approximation in most cases. However, for the ENO schemes to work correctly there has to be enough points between shocks to construct a smooth stencil. When shocks in different variables interact with each other, this assumption can be violated, and this simple extension is no longer adequate [33]. To avoid the issue, we use the *characteristic decomposition* to transform the problem into a set of k independent equations, one for each wave, which can then be handled separately.

Characteristic decomposition

If the system's Jacobian $A(\mathbf{U}) = \partial\mathbf{F}/\partial\mathbf{U}$ was constant, the MHD system could be decomposed into a set of independent advection equations of the characteristic variables $\mathbf{W}$ using the diagonalization procedure described in section 2.6.2. The ENO schemes described in the previous section can be applied to the individual advection equations for $\mathbf{W} = \{W_j\}$ to obtain their numerical fluxes $\mathbf{F}_W = \{f_{W,j}\}$. The physical numerical fluxes $\mathbf{F}$ can then be obtained with

$$\mathbf{F} = R\,\mathbf{F}_W. \tag{3.24}$$

Unfortunately, the Jacobian $A(\mathbf{U})$, as well as $\Lambda(\mathbf{U})$, $R(\mathbf{U})$, and $L(\mathbf{U})$, are *not* constant, which would normally mean the diagonalization procedure cannot be used. However, those matrices can be locally frozen to their values at the boundary $x_{i+\frac{1}{2}}$,

$$\begin{aligned} A_{i+\frac{1}{2}} &= A(\mathbf{U}_{i+\frac{1}{2}}), \quad \Lambda_{i+\frac{1}{2}} = \Lambda(\mathbf{U}_{i+\frac{1}{2}}), \\ R_{i+\frac{1}{2}} &= R(\mathbf{U}_{i+\frac{1}{2}}), \quad L_{i+\frac{1}{2}} = L(\mathbf{U}_{i+\frac{1}{2}}), \end{aligned} \tag{3.25}$$

when performing the reconstruction at that boundary. Treating them as constant allows us to perform the decomposition resulting in equation (2.48), which can then be used in calculations for the numerical flux at $x_{i+\frac{1}{2}}$.

The half-point values $\mathbf{U}_{i+\frac{1}{2}}$ that are used to locally freeze the matrices can be taken as either the simple average

$$\mathbf{U}_{i+\frac{1}{2}} = \frac{1}{2}\left(\mathbf{U}_i + \mathbf{U}_{i+1}\right) \tag{3.26}$$

or with some more complicated expression that has some useful properties. For example, in the case of Euler equations the Roe average [38] is often employed. For the MHD equations, this thesis averages the density, velocity, magnetic field, and total pressure [32].

ENO-Roe scheme for systems

When applying the ENO-Roe scheme to hyperbolic systems of PDEs using characteristic decomposition, we first calculate the numerical fluxes $\mathbf{F}(\mathbf{U}_i)$ and

undivided differences

$$\mathbf{V}_{F,i+\frac{1}{2}} = \mathbf{F}(\mathbf{U}_{i+1}) - \mathbf{F}(\mathbf{U}_i) \tag{3.27}$$

for all points x_i. Then, at each boundary $x_{i+\frac{1}{2}}$, we calculate the averaged half-point state $\mathbf{U}_{i+\frac{1}{2}}$ and the corresponding eigenvalues and eigenvectors according to (3.25). Next, for all l lying in the potential stencils for $x_{i+\frac{1}{2}}$, we set

$$\mathbf{v}_l = L_{i+\frac{1}{2}}\ \mathbf{F}(\mathbf{U}_l), \quad \mathbf{V}_{l+\frac{1}{2}} = L_{i+\frac{1}{2}}\ \mathbf{V}_{F,l+\frac{1}{2}}. \tag{3.28}$$

With these values we perform the element-wise ENO reconstruction to obtain the cell boundary values $\mathbf{v}^-_{i+\frac{1}{2}}$ and $\mathbf{v}^+_{i+\frac{1}{2}}$. Analogous to the scalar case, but using the eigenvalues as Roe speeds, the numerical flux $\bar{\mathbf{v}}_{i+\frac{1}{2}} = (\bar{v}_{1,i+\frac{1}{2}}, \ldots, \bar{v}_{k,i+\frac{1}{2}})$ at cell boundaries is obtained with

$$\bar{v}_{j,i+\frac{1}{2}} = \begin{cases} v^+_{j,i+\frac{1}{2}} & \text{, if } \lambda_{j,i+\frac{1}{2}} < 0 \\ v^-_{j,i+\frac{1}{2}} & \text{, if } \lambda_{j,i+\frac{1}{2}} \geq 0 \end{cases} \quad (j = 1, \ldots, k). \tag{3.29}$$

Finally, the obtained characteristic fluxes are returned to physical space with

$$\bar{\mathbf{F}}_{i+\frac{1}{2}} = R_{i+\frac{1}{2}}\ \bar{\mathbf{v}}_{i+\frac{1}{2}}. \tag{3.30}$$

ENO-LF scheme for systems

The ENO-LF scheme is extended in a similar vein as the ENO-Roe scheme. We first calculate the numerical fluxes $\mathbf{F}(\mathbf{U}_i)$ for all points x_i, as well as the averaged half-point states $\mathbf{U}_{i+\frac{1}{2}}$ with the corresponding eigenvalues $\lambda_{i+\frac{1}{2}}$ and eigenvectors $R_{i+\frac{1}{2}}, L_{i+\frac{1}{2}}$ at each boundary $x_{i+\frac{1}{2}}$. Next, for all l lying in the potential stencils for $x_{i+\frac{1}{2}}$, we decompose the system into the characteristic variables $\mathbf{W}_l$ and their fluxes $\mathbf{v}_l$,

$$\mathbf{W}_l = L_{i+\frac{1}{2}}\ \mathbf{U}_l, \quad \mathbf{v}_l = L_{i+\frac{1}{2}}\ \mathbf{F}(\mathbf{U}_l). \tag{3.31}$$

The ENO-LF scheme can be applied independently to each of the decoupled components $v_{j,l}$ $(j = 1, \ldots, k)$ of the transformed flux $\mathbf{v}_l = (v_{1,l}, \cdots, v_{k,l})$ to obtain the right-moving and left-moving partial fluxes. The splitting coefficient α_j is taken to be the largest eigenvalue of the jth component,

$$\alpha_j = \max_i(\lambda_j(u_{j,i})), \tag{3.32}$$

where i is again taken over the relevant range of u. After applying the ENO-LF scheme and recombining the partial fluxes into the numerical flux $\bar{\mathbf{v}}_{i+\frac{1}{2}}$ of the characteristic decomposition, the physical space numerical flux can be obtained with

$$\bar{\mathbf{F}}_{i+\frac{1}{2}} = R_{i+\frac{1}{2}}\ \bar{\mathbf{v}}_{i+\frac{1}{2}}. \tag{3.33}$$

3.1.5 Time integration

After applying the ENO-LF (or ENO-Roe) scheme, the discrete approximation $\mathbf{L}(\mathbf{U}_i)$ of $\partial\mathbf{U}/\partial t$ can be calculated by

$$\mathbf{L}(\mathbf{U}_i) = \frac{\bar{\mathbf{F}}_{i+\frac{1}{2}} - \bar{\mathbf{F}}_{i-\frac{1}{2}}}{x_{i+\frac{1}{2}} - x_{i-\frac{1}{2}}}, \tag{3.34}$$

and substituted into the optimal third order TVD Runge-Kutta method [35],

$$\begin{aligned}
\mathbf{U}^{(1)} &= \mathbf{U}^n + \Delta t\mathbf{L}(\mathbf{U}^n) \\
\mathbf{U}^{(2)} &= \frac{3}{4}\mathbf{U}^n + \frac{1}{4}\mathbf{U}^{(1)} + \frac{1}{4}\Delta t\mathbf{L}(\mathbf{U}^{(1)}) \\
\mathbf{U}^{n+1} &= \frac{1}{3}\mathbf{U}^n + \frac{2}{3}\mathbf{U}^{(2)} + \frac{2}{3}\Delta t\mathbf{L}(\mathbf{U}^{(2)}),
\end{aligned} \tag{3.35}$$

where $\mathbf{U}^n$ and $\mathbf{U}^{n+1}$ are the state vectors at time steps n and $n+1$, and $\mathbf{U}^{(1)}$ and $\mathbf{U}^{(2)}$ are the state vectors of the intermediate RK steps. The order of the scheme is shown in Appendix A.

The time step Δt is calculated from maximum wave speeds at every time step, halving or doubling the value as required to stay below the desired Courant-Friedrichs-Lewy (CFL) number [36]. In the simulation code the exact condition is configurable, though for all simulations in this thesis the CFL number was set to 0.1.

3.1.6 Extension to 2D

In 2D systems, we assume only one direction to be homogeneous. Conservation laws of the form (2.6) are reduced to

$$\frac{\partial\mathbf{U}}{\partial t} + \frac{\partial\mathbf{F}}{\partial x} + \frac{\partial\mathbf{G}}{\partial y} = 0 \tag{3.36}$$

with $\mathbf{U} = \mathbf{U}(x, y, t)$ and two fluxes, $\mathbf{F} = \mathbf{F}(\mathbf{U})$ in x direction, and $\mathbf{G} = \mathbf{G}(\mathbf{U})$ in y direction. By using the Jacobians $A(\mathbf{U}) = \partial\mathbf{F}/\partial\mathbf{U}$ and $B(\mathbf{U}) = \partial\mathbf{G}/\partial\mathbf{U}$, we can write

$$\frac{\partial \mathbf{U}}{\partial t} + A(\mathbf{U})\frac{\partial \mathbf{U}}{\partial x} + B(\mathbf{U})\frac{\partial \mathbf{U}}{\partial y} = 0. \tag{3.37}$$

When adapting the ENO-Roe scheme to higher dimensions, there are multiple possible approaches of various levels of complexity. We employ the simplest approach, where we treat each direction as a separate 1D problem, solving the fluxes for each direction separately, and generate the total flux by simple addition. Specifically, after the numerical fluxes $\bar{\mathbf{F}}_{i+\frac{1}{2}}$ and $\bar{\mathbf{G}}_{j+\frac{1}{2}}$ are obtained, the discrete approximation $\mathbf{L}(\mathbf{U})$ of $\partial\mathbf{U}/\partial t$ in the time integration step is modified to

$$\mathbf{L}(\mathbf{U}_{i,j}) = \frac{\bar{\mathbf{F}}_{i+\frac{1}{2},j} - \bar{\mathbf{F}}_{i-\frac{1}{2},j}}{x_{i+\frac{1}{2},j} - x_{i-\frac{1}{2},j}} + \frac{\bar{\mathbf{G}}_{i,j+\frac{1}{2}} - \bar{\mathbf{G}}_{i,j-\frac{1}{2}}}{y_{i,j+\frac{1}{2}} - y_{i,j-\frac{1}{2}}}, \tag{3.38}$$

where i and j are, respectively, the grid indices in the x and y directions.

Divergence cleaning

Using a 1D solver on a 2D MHD system solves one problem, but creates another. As the $\boldsymbol{\nabla} \cdot \mathbf{B} = 0$ condition is not explicitly enforced in the MHD equations, the independent calculations in x and y direction are likely to introduce an error and the divergence becomes non-zero. This error accumulates exponentially [39]. To remedy this issue, after every time step we conduct divergence cleaning by solving the Poisson equation

$$\nabla^2\phi + \boldsymbol{\nabla} \cdot \mathbf{B} = 0 \tag{3.39}$$

with the SOR (Successive Over-Relaxation) method [40] with relaxation parameter $\omega = 1.6$, and calculating the corrected magnetic field [30] with

$$\mathbf{B}_{\text{corrected}} = \mathbf{B} + \boldsymbol{\nabla}\phi. \tag{3.40}$$

Discretizing the Poisson equation with central finite differences, we obtain

$$\begin{aligned}\frac{1}{\Delta x^2}(\phi_{i-2,j} - 2\phi_{i,j} + \phi_{i+2,j}) + \frac{1}{\Delta y^2}(\phi_{i,j-2} - 2\phi_{i,j} + \phi_{2,j+2}) \\ + \frac{1}{2\Delta x}(B_{x,i+1,j} - B_{x,i-1,j}) + \frac{1}{2\Delta y}(B_{y,i,j+1} - B_{y,i,j-1}) = 0,\end{aligned} \tag{3.41}$$

which can be rearranged into

$$\left(\frac{1}{\Delta x^2}+\frac{1}{\Delta y^2}\right)\phi^*_{i,j} = \frac{1}{\Delta x^2}(\phi_{i-2,j}+\phi_{i+2,j}) + \frac{1}{\Delta y^2}(\phi_{i,j-2}+\phi_{2,j+2}) + \frac{1}{2\Delta x}(B_{x,i+1,j}-B_{x,i-1,j}) + \frac{1}{2\Delta y}(B_{y,i,j+1}-B_{y,i,j-1}), \tag{3.42}$$

where $\phi^*_{i,j}$ is the value of ϕ calculated from the discretization. Defining

$$r = \phi^*_{i,j} - \phi_{i,j} \tag{3.43}$$

as the residue, we can calculate a more accurate guess $\phi^{\text{new}}_{i,j}$ as

$$\phi^{\text{new}}_{i,j} = \phi_{i,j} + \omega r, \tag{3.44}$$

and repeat the procedure until the maximum residue $\max|r|$ falls below some desired threshold.

3.2 Implementation

The simulation code has been developed in C++. The only external dependency is the Boost library [41], which is used to read and process the configuration file. The numerical simulation code itself is manually written. The source code is available on GitHub [42]. The latest commit used in this thesis is `302a641d` from March 2019. Although many of the simulations have been run with earlier versions, later changes are almost exclusively additional test problems and configuration options, with a few minor bug fixes that shouldn't impact the results.

The core algorithm, an implementation of the ENO scheme for systems of equations with the Lax–Friedrichs flux splitting as described by Shu [36] (section 3.1.4), uses a 1D solver and applies it separately to x and y directions to obtain the numerical fluxes for each grid point. The time is advanced through the method of lines, where numerical fluxes are applied with the third order Runge–Kutta scheme (section 3.1.5). Finally, the magnetic field is corrected by solving the Poisson equation (3.39) with the SOR method and applying the

Grid density	Total grid size	Total steps	Real time (s)	Real time
16	512×96	5120	1171	$\sim$ 20 min
32	1024×192	11247	12395	$\sim$ 3 h 45 min
64	2048×384	21747	200982	$\sim$ 2 d 8 h

Table 3.1: Running time for the simulations under identical conditions, except for grid density. Simulations were run until $t_{\max} = 10$. Times shown are for the personal computer.

correction to the magnetic field. Simulations of several standard test problems for MHD numerical codes are presented in Appendix B.

Runtime environment

The simulations, including numerical tests, were predominantly run on the author's personal computer (CPU: Intel Core i7-4790S, 3.20GHz, 4 physical cores; memory: 16 GB). Simulations with grid density of 64 points per unit length (total grid size of 2048×384) were—except for a couple of test runs—run on the laboratory's server, as each run took several days to complete. Typical times for individual simulation runs are shown in table 3.1.

Note that the simulation code is not parallelized. As a large number of simulations was required, quasy-parallelization was achieved by running two or three simulations at the same time. This did not noticeably impact individual running times.

Chapter 4

One-dimensional plasma sheet model

4.1 Piston model

In the current disruption model of auroral breakup, the plasma loss in the near-Earth magnetotail induces a rarefaction wave that propagates tailward. Chao *et al.* [7] have used a simplified 1D model to explore the behavior of the rarefaction wave in the Earth's plasma sheet. The model is assumed to be valid in the distant tail region.

In the proposed model, the weakly magnetized (plasma beta $\beta \gg 1$, where $\beta = 2p/B^2$) inner plasma sheet is approximated as a 1D tube of isotropic gas (the horizontal blue line in figure 4.1). An imaginary piston is placed on the near-Earth side of the tube, and at time $t = 0$, the piston starts moving Earthward at constant velocity. The movement causes a pressure drop behind the piston, which in turn generates a rarefaction wave. The resulting pressure profile of the inner plasma sheet was used to model the thinning of the entire sheet.

The time evolution of gas in the 1D piston-bounded tube has an exact solution [43]. If piston is moving at velocity $u_\mathrm{p} < 0$, then for $0 < -u_\mathrm{p} < 2c_{\mathrm{s},0}/(\gamma - 1)$, where $c_{\mathrm{s},0} = \sqrt{\gamma p_0/\rho_0}$ is the sound velocity, p_0 and ρ_0 are the initial pressure and density inside the 1D gas tube, and γ is the ratio of specific

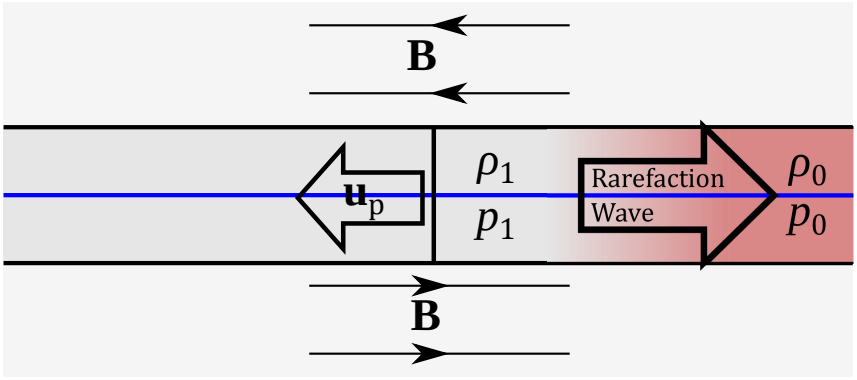

Figure 4.1: A simplified structure of the distant tail region of the plasma sheet. In the piston model, the inner plasma sheet is bounded on the Earth side by a piston moving at velocity u_p; the movement launches a rarefaction wave tailwards. Plasma sheet itself is modeled as unmagnetized 1D slab of gas, depicted here by a horizontal blue line through the center of the sheet. Density ρ_0 and pressure p_0 depict the initial state of the sheet, while density ρ_1 and pressure p_1 depict the state after rarefaction.

heats, plasma velocity $u(x,t)$, pressure $p(x,t)$, and density $\rho(x,t)$ are given by

$$u(x,t) = \begin{cases} u_\mathrm{p} & \text{if } x < \left(c_{\mathrm{s},0} + \frac{\gamma+1}{2}u_\mathrm{p}\right)t, \\ 0 & \text{if } x > c_{\mathrm{s},0}t, \\ \frac{2}{(\gamma+1)t}x - \frac{2c_{\mathrm{s},0}}{\gamma+1} & \text{otherwise,} \end{cases} \tag{4.1}$$

$$p(x,t) = p_0\left[1 - \frac{\gamma-1}{2}\frac{|u(x,t)|}{c_{\mathrm{s},0}}\right]^{2\gamma/(\gamma-1)}, \tag{4.2}$$

$$\rho(x,t) = \rho_0\left[1 - \frac{\gamma-1}{2}\frac{|u(x,t)|}{c_{\mathrm{s},0}}\right]^{2/(\gamma-1)}. \tag{4.3}$$

An example plot is shown in figure 4.2. The exact solution of the 1D piston model describes the state of the inner plasma sheet as the rarefaction wave propagates through it.

Chao *et al.* [7] argue that the plasma sheet changes through three distinct stages formed by two separate events, the rarefaction wave and the adiabatic compression (see figure 4.3). Before the rarefaction wave, sheet plasma is in its initial state, denoted by the subscript "0", and sheet and lobe are balanced with a constant total pressure $p_{\mathrm{total},0}$. After the rarefaction wave passes, the

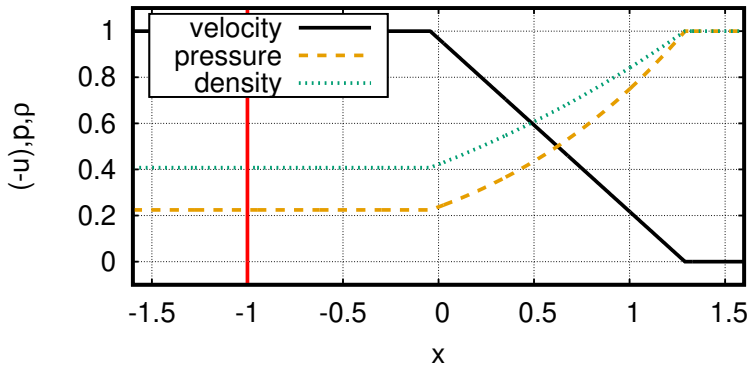

Figure 4.2: Exact solution for the 1D piston model of the plasma sheet, for $p_0 = \rho_0 = 1$, $u_\mathrm{p} = -1$, at time $t = 1$. Shown are the velocity (solid black line), pressure (dashed orange line), and density (dotted green line) profiles, with current piston location at $x = -1$ marked with a red vertical line.

pressure and density of the lobe plasma are reduced. The properties of the sheet plasma in this stage are denoted by the subscript "1". Lowering the sheet pressure breaks the sheet-lobe balance and induces the sheet-lobe boundary to move inward, causing *plasma sheet thinning*, which compresses the sheet plasma and re-establishes the sheet-lobe balance. The properties of the sheet plasma in this final stage are denoted by the subscript "2". The sheet plasma is assumed to be isotropic in the first two stages, and anisotropic in the last stage, after the perpendicular compression.

We consider the plasma sheet to consist of a stack of 1D layers to allow spatial variation across the sheet, and focus on a fluid element of the plasma sheet initially located at y (see figure 4.3). Then, the actual perpendicular position of the element can be described as a function of y: $y_0(y) = y$ is the initial position, $y_1(y)$ is where the fluid element that started at y is after the rarefaction wave passed (as there is no perpendicular movement yet, $y_1(y) = y_0(y) = y$), and $y_2(y)$ is where the fluid element that started at y is after thinning ($y_2(y) \neq y_0(y)$ due to perpendicular compression). Similarly, a property φ of the fluid element changes from $\varphi_0(y_0(y)) = \varphi_0(y)$, to $\varphi_1(y_1(y)) = \varphi_1(y)$, and finally to $\varphi_2(y_2(y))$, where, again, $y_0(y) = y_1(y) = y$, and due to perpendicular compression $y_2(y) \neq y$.

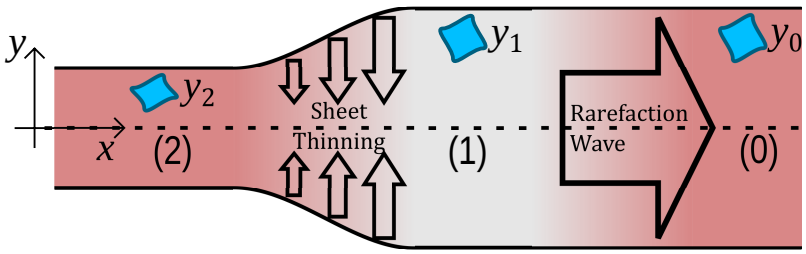

Figure 4.3: Development stages of the plasma sheet in the 1D piston model of the plasma sheet thinning. The initial state (0) is transformed by the passing of the rarefaction wave into state (1), which is in turn transformed by thinning into state (2). The fluid elements are shown in blue.

Using the above definitions, the equations describing the initial state of the plasma [7] become

$$p_0(y_0(y)) = p_{\mathrm{total},0} - \frac{1}{2}B_0^2(y_0(y)), \tag{4.4}$$

$$\rho_0(y_0(y)) = \frac{\gamma p_0(y_0(y))}{c_{\mathrm{s},0}^2}, \tag{4.5}$$

$$\beta_0(y_0(y)) = \frac{2p_0(y_0(y))}{B_0^2(y_0(y))}, \tag{4.6}$$

where the speed of sound in the sheet $c_{\mathrm{s},0}$ is assumed constant through all of the 1D layers in the sheet, and $p_{\mathrm{total},0}$ is the total pressure, which can be expressed using the magnetic field strength and plasma beta at the sheet side of the sheet-lobe boundary, $B_{\mathrm{b},0}$ and $\beta_{\mathrm{b},0}$,

$$p_{\mathrm{total},0} = \frac{1}{2}B_{\mathrm{b},0}^2(\beta_{\mathrm{b},0} + 1). \tag{4.7}$$

The boundary between the plasma sheet and magnetic lobes is assumed to be a tangential discontinuity (see section 5.1 for the reasoning), where the total pressure has to be balanced across the boundary. Using the exact solutions (4.2) and (4.3), pressure and density behind the rarefaction wave become

$$p_1(y_1(y)) = p_0(y_0(y))\left[1 - \frac{\gamma-1}{2}\frac{|u_{\mathrm{p}}|}{c_{\mathrm{s},0}}\right]^{2\gamma/(\gamma-1)}, \tag{4.8}$$

$$\rho_1(y_1(y)) = \rho_0(y_0(y))\left[1 - \frac{\gamma-1}{2}\frac{|u_{\mathrm{p}}|}{c_{\mathrm{s},0}}\right]^{2/(\gamma-1)}, \tag{4.9}$$

where $u_{\rm p}$ is the speed of the imaginary piston.

Finally, the sheet undergoes a perpendicular compression, which is assumed to follow the CGL (Chew-Goldberger-Low) double adiabatic variation. The total pressure in the sheet becomes anisotropic, and the final state of the sheet plasma becomes [7]

$$\beta_{\perp,2}(y_2(y)) = \frac{2p_1(y_1(y))}{B_0^2(y_0(y))}, \tag{4.10}$$

$$B_2^2(y_2(y)) = \frac{2p_{\rm total,0}}{1+\beta_{\perp,2}(y_2(y))}, \tag{4.11}$$

$$p_{\perp,2}(y_2(y)) = p_1(y_1(y))\frac{B_2^2(y_2(y))}{B_0^2(y_0(y))}, \tag{4.12}$$

$$p_{\parallel,2}(y_2(y)) = p_1(y_1(y))\frac{B_2(y_2(y))}{B_0(y_0(y))}, \tag{4.13}$$

$$\rho_2(y_2(y)) = \rho_1(y_1(y))\frac{B_2(y_2(y))}{B_0(y_0(y))}, \tag{4.14}$$

where $\beta_{\perp,2}$ is the plasma beta in the direction perpendicular to the ambient magnetic field, while $p_{\perp,2}$ and $p_{\parallel,2}$ are, respectively, the perpendicular and parallel components of pressure p_2.

We assume that the profile of the magnetic field in the plasma sheet is

$$B_0(y_0(y)) = B_\infty \tanh(y/y_{\rm b}), \tag{4.15}$$

where $y_{\rm b}$ is the sheet half-thickness (see figure 4.4(a)), and B_∞ is determined from the value of B_0 at the inner edge of the sheet-lobe boundary ($y \to y_{\rm b} - 0$). Taking the value of sheet plasma beta at the inner edge of the boundary as $\beta_{\rm b,0} = 2.5$, piston velocity $u_{\rm p} = 0.8\ c_{\rm s,0}$, and sheet half-thickness $y_{\rm b} = 3.0\ R_{\rm E}$, and substituting them into the above equations, we obtain the values in table 4.1. Comparing with results from Chao *et al.* [7], shown in table 4.2, we can see that the values are within 5%; the slight difference in results is most likely due to rounding.

To calculate the thickness $y_2(y)$ of the thinned plasma sheet, we assume that the magnetic flux is conserved. We take the values of $B_0(y_0(y^{(n)}))$ at $y^{(n)} = 0.6n$, $n = 0, \ldots, 5$, and approximate the profile of the magnetic field

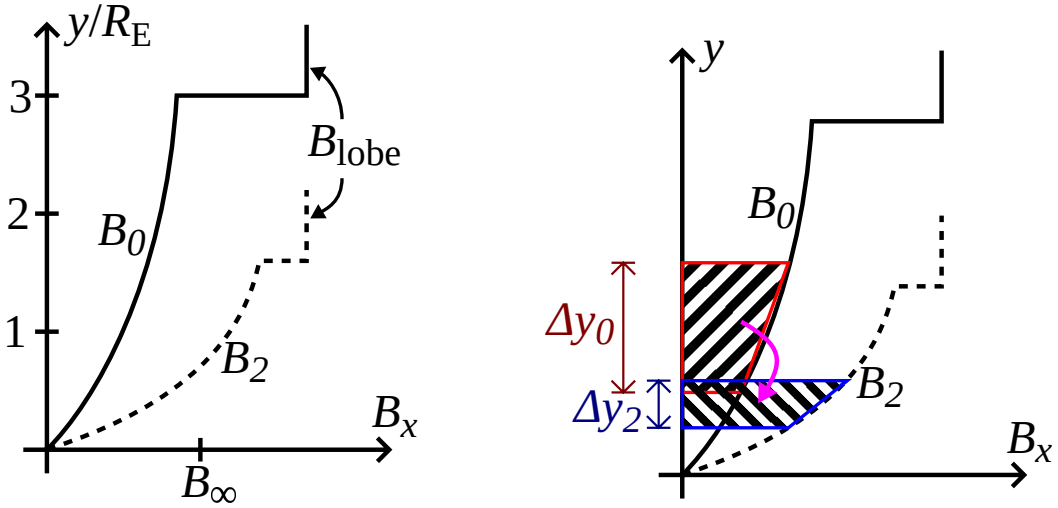

(a) magnetic field

(b) integration

Figure 4.4: Profile of the magnetic field in the 1D plasma sheet model. (a) shows initial profile and profile after thinning, adapted from Chao *et al.* [7]. (b) shows the trapezoid approximation used to calculate the thickness of the plasma sheet after thinning, with $\Delta y_0 = y^{(n)} - y^{(n-1)}$ and $\Delta y_2 = y_2(y^{(n)}) - y_2(y^{(n-1)})$.

y	y_0	y_2	β_0	B_2^2/B_0^2	$p_{\perp,2}/p_0$	$p_{\parallel,2}/p_0$	ρ_2/ρ_0	$p_{\parallel,2}/p_{\perp,2}$
0.6	0.6	0.29	51.11	4.40	0.93	0.44	0.83	0.48
1.2	1.2	0.59	13.06	3.73	0.79	0.41	0.76	0.52
1.8	1.8	0.92	6.04	3.09	0.65	0.37	0.69	0.57
2.4	2.4	1.27	3.60	2.61	0.55	0.34	0.64	0.62
3.0	3.0	1.66	2.50	2.29	0.49	0.32	0.60	0.66

Table 4.1: Properties of the plasma sheet after thinning in the 1D piston model. Coordinates y, y_0, and y_2 are given in units of R_E.

y_0	y_2	B_2^2/B_0^2	$p_{\perp,2}/p_0$	$p_{\parallel,2}/p_0$	ρ_2/ρ_0	$p_{\parallel,2}/p_{\perp,2}$
0.6	0.28	4.4	0.93	0.44	0.83	0.48
1.2	0.58	3.7	0.79	0.41	0.76	0.52
1.8	0.92	3.1	0.65	0.37	0.69	0.57
2.4	1.28	2.6	0.55	0.34	0.63	0.62
3.0	1.67	2.3	0.48	0.32	0.59	0.66

Table 4.2: Properties of the plasma sheet after thinning in the 1D piston model, taken from Chao *et al.* [7]. Coordinates y_0 and y_2 are given in units of $R_{\rm E}$.

with trapezoids (see figure 4.4(b)). Then, $y_2(y^{(n)})$ can be obtained from

$$y_2(y^{(n)}) = y_2(y^{(n-1)}) + (y^{(n)} - y^{(n-1)})\frac{B_0(y_0(y^{(n-1)})) + B_0(y_0(y^{(n)}))}{B_2(y_2(y^{(n-1)})) + B_2(y_2(y^{(n)}))}, \quad (4.16)$$

where $n = 1, \ldots, 5$ and $B_0(y_0(y^{(0)})) = B_2(y_2(y^{(0)})) = 0$.

To recap, as the rarefaction wave moves tailward, behind it the pressure in the inner sheet falls. To keep the balance of the total pressure, as required by the tangential discontinuity, the sheet–lobe boundary has to move inward, thinning the plasma sheet. The thickness of the plasma sheet after the thinning is a function of piston velocity, which is estimated to be between 0.25 $c_{\rm s,0}$ and 1.25 $c_{\rm s,0}$. At velocity $u_{\rm p} = 0.8\ c_{\rm s,0}$, the thickness of the plasma sheet is reduced to around half of the original value.

It is noted here that Chao *et al.* [7] argue that plasma sheet thinning takes place under two separate steps of 1) rarefaction, and 2) adiabatic compression. As can be seen from the exact solution for the rarefaction wave in (4.1), it also follows that the right front of the thinned plasma sheet is located at $x \leq (c_{\rm s,0} + (\gamma+1)u_{\rm p}/2)t$, which might even move to the left, especially when $|u_{\rm p}|$ is large. In this thesis, I will argue that these two steps proceed at the same time scale, and the plasma shows more complicated dynamics with propagation and reflection of various plasma waves.

4.2 Initial velocity model

While the piston model works well for the 1D model of rarefaction, it becomes problematic if we attempt to extend the model to two or more dimensions. Therefore, we replace the 1D piston model with an equivalent model that will be easier to extend.

From the Galilean invariance of the MHD equations (see section 2.5), the piston moving with a velocity u_p in a fixed plasma is equivalent to the fixed piston (i.e., a wall) in a moving plasma with the velocity $-u_\mathrm{p}$.

Mirroring the wall system around the wall location, we obtain a combined system with a wall in the middle, two (mirrored) rarefaction waves moving outward, and stationary plasma behind the rarefaction waves. Since the plasma around the wall is stationary, the wall can be removed without influencing the solution. We are left with a system where two lumps of plasmas are moving apart with the velocity $\pm u_\mathrm{p}$ from a fixed point in space. The fixed point may be regarded as the piston in the 1D piston model by Chao *et al.* [7]

With a second application of the Galilean invariance, we can make the system symmetric around u_p, so that the right half is identical to the piston model we started with. The initial plasma velocities become 0 and $u_\mathrm{init} \equiv 2u_\mathrm{p}$, where u_init is the initial disturbance parameter that will be introduced in section 5.1.

The equivalence of the piston model and the initial velocity model can be clearly seen in figure 4.5, where mirror symmetric forward and backward rarefaction waves of the initial velocity model simulation are shown as the solid line, and the dashed line denotes the analytic solution to the piston model as given in equations (4.1)–(4.3).

In the next chapter, we will extend this initial velocity model into 2D.

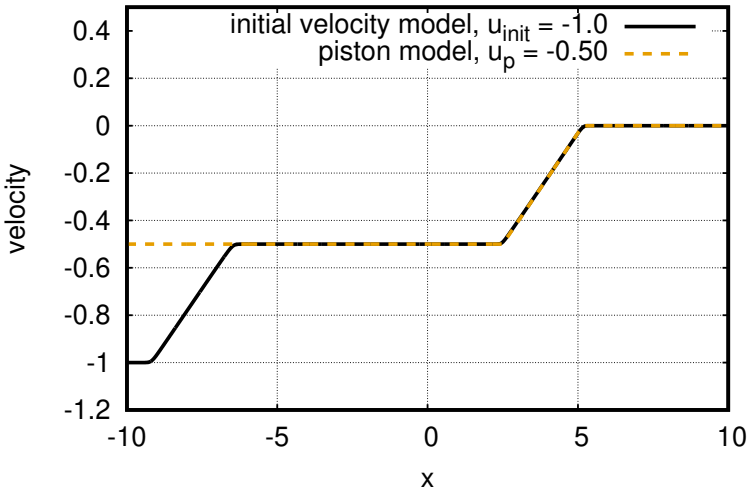

(a) velocity at $t = 4.0$

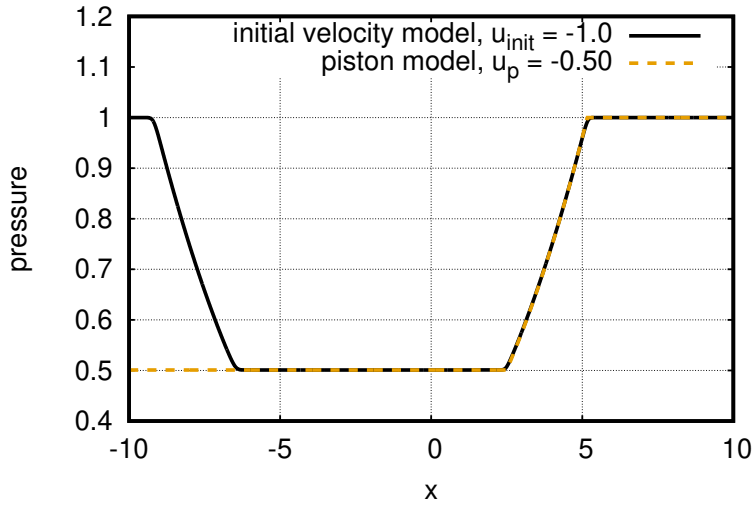

(b) pressure at $t = 4.0$

Figure 4.5: Results of the numerical simulation of the initial velocity model (solid line) compared to the exact solution of the equivalent piston model (dashed line). The plots shown are for (a) velocity and (b) pressure at time $t = 4.0$.

Chapter 5

Two-dimensional plasma sheet model

In the 1D piston model by Chao *et al.* [7], the rarefaction wave in the inner plasma sheet depends solely on the initial conditions of said region. Furthermore, while the plasma sheet thinning is assumed to occur as a consequence of the pressure drop behind the rarefaction wave, the model itself is built as a two-step process. The first step in the process is the rarefaction wave, where the initial pressure and density are reduced to the values in equations (4.2)–(4.3), and the second step is the thinning process itself, where the rarefied plasma is assumed to be compressed by the inward movement of the boundary. However, there is no mechanism in the model for the changes in the magnetic field configuration and inner sheet pressure caused by the thinning process to influence the sheet plasma before or during the rarefaction wave; those effects are outside the scope of the model.

To further explore the thinning process itself, as well as the effects it may have on the rarefaction wave, requires extending the model so it includes more of the relevant plasma sheet configuration. Specifically, we can expect that the strong magnetic field in the lobes may have a significant effect on the dynamics.

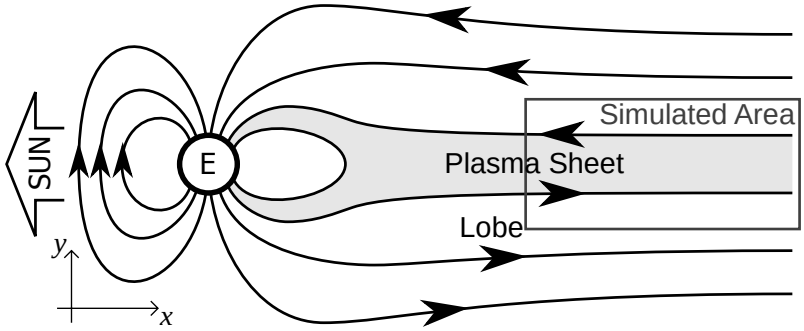

Figure 5.1: Rough structure of the Earth's magnetosphere, with the modeled area marked.

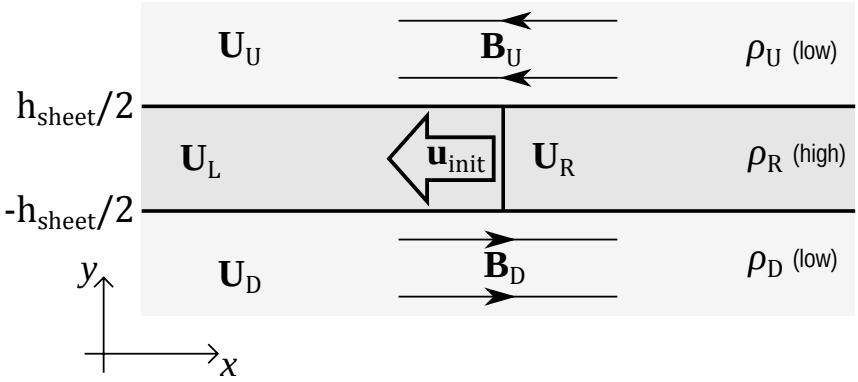

Figure 5.2: Initial configuration of the modeled area, including the plasma sheet and a section of north and south magnetic lobes.

5.1 Plasma sheet model

Starting with the 1D initial velocity model from section 4.2, we extend it to 2D and include the north and south magnetic lobes, modeling the 2D vertical cross-section of the plasma sheet.

To simplify the initial setup we take the relatively flat area of the plasma sheet, with approximately parallel magnetic field lines (figure 5.1). We mark the x axis so it points from the Earth tailward, and y axis to point north, so that the x-y plane becomes the cross section. (Note: the usual convention, where z axis points north, is not used so that we have a more natural notation for the MHD equations.)

We separate the modeled region into four main sub-regions, as shown in

figure 5.2. If we take the thickness of the plasma sheet to be h_{sheet}, then the sub-region where $y > h_{\text{sheet}}/2$ is the northern lobe, the sub-region where $y < h_{\text{sheet}}/2$ is the southern lobe, and the sub-region where $-h_{\text{sheet}}/2 < y < h_{\text{sheet}}/2$ is the neutral sheet. The neutral sheet is further divided into the left ($x < 0$) and right ($x > 0$) halves, with the right half being in the steady-state configuration, and the left half being where the initial disturbance occurs.

The steady-state neutral sheet contains weakly magnetized plasma of high density, $\mathbf{U}_{\text{sheet}}$. On the north and south are the magnetic lobes, containing low density plasmas in strong, antiparallel magnetic fields, $\mathbf{U}_{\text{U}}$ (where "U" stands for "Up") and $\mathbf{U}_{\text{D}}$ ("Down"). After the initial disturbance is applied, the right half of the plasma sheet contains the as-of-yet undisturbed plasma $\mathbf{U}_{\text{R}} = \mathbf{U}_{\text{sheet}}$ ("Right"), while the left half contains the disturbed plasma $\mathbf{U}_{\text{L}}$ ("Left").

The profile of the magnetic field in the inner layer of the plasma sheet was assumed by Chao *et al.* [7] to be the current sheet profile $\mathbf{B}_{\text{sheet}} = \mathbf{B}_{\infty} \tanh(y)$. However, simulations have shown that the results are almost identical if the plasma in the plasma sheet is uniform and has no magnetic field. Since a uniform plasma with sharp sheet–lobe transitions is significantly easier to analyze, the uniform plasma sheet is used for the initial condition in our simulations, $\mathbf{B}_{\text{sheet}} = \mathbf{0}$. We also assume that initially the plasma sheet and lobes are in a steady-state configuration.

The plasma state across the sheet–lobe boundary is discontinuous. To determine which type of the MHD discontinuity applies, we consider that, across the boundary [7],

(a) the magnitude of the magnetic field changes,

(b) there is no high-speed flow (greater than 100 km/s; the sound speed is on the order of 400 km/s), and

(c) plasma density falls by an order of magnitude when going from sheet to lobe.

Comparing the above with the Rankine-Hugoniot jump conditions [9], it follows that the sheet–lobe boundary is not a shock, as, according to (b), the

mass flux across the boundary is very low; additionally, in an MHD shock with $\gamma = 5/3$ plasma density can increase at most fourthfold [7], which is ruled out by (c). In a rotational discontinuity [9], the magnetic field strength across the boundary is constant; therefore, a rotational discontinuity is ruled out by (a). The same point rules out the contact discontinuity, in which both strength and direction of the magnetic field must be exactly equal. That leaves only the tangential discontinuity. For a tangential discontinuity, the magnetic field and velocity have no component normal to the boundary; therefore, point (b) allows it, but only as an approximation. Additional Rankine-Hugoniot jump condition for a tangential discontinuity [9] is

$$[p_{\text{total}}] = 0, \tag{5.1}$$

where $[\varphi]$ denotes the jump in φ when crossing the boundary. Under the model's assumptions, the plasma sheet magnetic field is uniform, $\mathbf{B}_{\text{sheet}} = \mathbf{0}$, and the lobe magnetic field is pointing in the x direction, $\mathbf{B}_{\text{U,D}} = \pm\mathbf{B}_{\text{lobe}} = (\pm B_{x,\text{lobe}}, 0, 0)$. Substituting the above into the expression for total pressure (2.32), the jump condition (5.1) becomes

$$p_{\text{sheet}} = p_{\text{lobe}} + \frac{1}{2}B_{x,\text{lobe}}^2. \tag{5.2}$$

The system is normalized so that $p_{\text{sheet}} = 1.0$, $\rho_{\text{sheet}} = 1.0$, and the initial thickness of the plasma sheet is $h_{\text{sheet}} = 1.0$, covering the area $-0.5 < y < 0.5$. The normalization parameters are determined by the process introduced in section 2.4, with the conversion relation for physical quantity φ defined as $\varphi_{\text{real}} = \hat{\varphi}\varphi_{\text{sim}}$, where φ_{real} are the physical units, φ_{sim} are the normalized units used in the simulation, and $\hat{\varphi}$ are the normalization parameters. The normalization parameters $\hat{\varphi}$ are strongly coupled, as they have to satisfy the MHD equations. Only three of the parameters can be set freely; here, the chosen free parameters are distance $\hat{l} \approx 3R_{\text{E}}$, ion temperature $\hat{T}_{\text{i}}$, and ion number density $\hat{n}_{\text{i}}$. The normalization has been performed using the realistic values for sheet and lobe obtained from satellite measurements [9, 44] as the baseline. The baseline values and the relationship between physical and normalized units are shown in table 5.1.

	time, t (s)	length, l (m)	velocity, u (m/s)
normalization parameter $\hat{\varphi}$	30	1.9×10^7	6.5×10^5
	ion num. dens., n_i (m^{-3})	ion temp., T_i (K)	density, ρ ($\mathrm{kg/m}^3$)
normalization parameter $\hat{\varphi}$	5.0×10^5	5.0×10^7	8.4×10^{-22}
realistic, sheet	5.0×10^5	5.0×10^7	8.4×10^{-22}
realistic, lobe	1.0×10^4	5.0×10^6	1.7×10^{-23}
	pressure, p (nPa)	mag. field, B (nT)	
normalization parameter $\hat{\varphi}$	0.35	21	
realistic, sheet	0.35	10	
realistic, lobe	0.00069	30	

Table 5.1: Units are normalized with respect to the plasma sheet. Table has been divided into three groups for space reasons. The first row of each group are the normalization parameters $\hat{\varphi}$. In the second and third rows of the second and third group are the realistic values for, respectively, plasma sheet and magnetic lobe, obtained from satellite measurements [9, 44].

Since the physical quantities are normalized to sheet conditions and the geometry is fixed, the system has only a few degrees of freedom left to parameterize. As a first parameter we take the *lobe plasma beta* β_{lobe}, where plasma beta is defined as $\beta = 2p/B^2$ (note that the usual factor of μ_0 is gone due to normalization).

The second parameter is the kinetic *temperature ratio* τ,

$$\tau = \frac{T_{\text{i,sheet}}}{T_{\text{i,lobe}}} = \frac{p_{\text{sheet}}/\rho_{\text{sheet}}}{p_{\text{lobe}}/\rho_{\text{lobe}}}, \tag{5.3}$$

where the ion temperature T_{i} is defined through

$$p = n_{\text{i}} k_{\text{B}} T_{\text{i}} \tag{5.4}$$

$$\rho = n_{\text{i}} m_{\text{p}}, \tag{5.5}$$

where n_{i} is the ion number density, k_{B} is the Boltzmann constant, and m_{p} is the proton mass (it is assumed that plasma consists overwhelmingly of electrons and hydrogen ions).

Assuming the aforementioned normalization and the fixed geometry, the steady-state initial condition of the plasma sheet is fully defined by the two parameters plasma beta β_{lobe} and temperature ratio τ.

The current disruption in the magnetosphere is outside of scope of the MHD theory [12], therefore we need to approximate the disruption with an initial disturbance. The piston model which was used by Chao *et al.* [7] to induce the rarefaction wave is replaced with a uniform Earthward plasma flow (see section 4.2). The flow is created by assigning an initial velocity $\mathbf{u}_{\text{init}} = (u_{\text{init}}, 0, 0)$ to the plasma $\mathbf{U}_{\text{L}}$ on the Earth side of the plasma sheet (see figure 5.2; $x < 0$, $-0.5 < y < 0.5$ in figures 5.3 and 5.4).

The velocity magnitude u_{init}, which indicates the strength of the disturbance, is the third and final parameter needed to unambiguously define the stated plasma sheet problem. This parameter is equivalent to the initial velocity in the 1D initial velocity model introduced in section 4.2.

Unfortunately, the discontinuities in the initial conditions were causing numerical artefacts to appear, displaying a diagonal hatch pattern over the simulation area. The form of the pattern suggests that the main source of

error was the divergence cleaning step; as under the SOR implementation it uses a point (x_i, y_i) depends only on $(x_{i\pm2}, y_{i\pm2})$; as a consequence, neighboring grid points are mutually independent. To reduce these numerical artefacts, the discontinuities—namely, the jump in pressure, density, and the magnetic field across the tangential discontinuity, as well as the jump in velocity between the $\mathbf{U}_\mathrm{L}$ region and the other three—have been smeared over two additional grid points [45].

5.2 Simulation box and boundary conditions

The simulation box length for the results presented in this thesis was $(L_x, L_y) = (32.0, 6.0)$ units, with $-16 \leq x \leq 16$, $-3 \leq y \leq 3$. The grid density per unit length in x and y direction is 16, 32, and 64 grid points, for a total of, respectively, $(N_x, N_y) = (512, 96)$, $(1024, 192)$, and $(2048, 384)$ grid points for the entire simulation box. A handful of simulation runs have been made with double the length (and grid points) in the y direction. The results for the extended simulation area had shown a minor difference in the lobes, as the slight wave reflection from the boundary is eliminated; however, there was no effect on the observed behavior of the sheet–lobe boundary, indicating that the reflection is too weak to influence the results presented in the following sections.

The boundary conditions for the simulation are Dirichlet at $x = -L_x/2$ (Earth) and $x = L_x/2$ (tail), with values being set to their initial values as defined above,

$$\mathbf{U}(-L_x/2, y, t) = \begin{cases} \mathbf{U}_\mathrm{U}(-L_x/2, y) & (h_\mathrm{sheet}/2 < y) \\ \mathbf{U}_\mathrm{L}(-L_x/2, y) & (-h_\mathrm{sheet}/2 < y < h_\mathrm{sheet}/2)\,, \\ \mathbf{U}_\mathrm{D}(-L_x/2, y) & (y < -h_\mathrm{sheet}/2) \end{cases} \tag{5.6}$$

$$\mathbf{U}(L_x/2, y, t) = \begin{cases} \mathbf{U}_\mathrm{U}(L_x/2, y) & (h_\mathrm{sheet}/2 < y) \\ \mathbf{U}_\mathrm{R}(L_x/2, y) & (-h_\mathrm{sheet}/2 < y < h_\mathrm{sheet}/2)\,. \\ \mathbf{U}_\mathrm{D}(L_x/2, y) & (y < -h_\mathrm{sheet}/2) \end{cases} \tag{5.7}$$

For the other two boundaries, the boundary conditions are Neumann at $y = -L_y/2$ (south) and $y = L_y/2$ (north), except for the magnetic field component perpendicular to the boundary, which is calculated from $\boldsymbol{\nabla} \cdot \mathbf{B} = 0$;

$$\frac{\partial}{\partial y}\rho(x, -L_y/2, t) = 0, \tag{5.8}$$

$$\frac{\partial}{\partial y}(\rho u)(x, -L_y/2, t) = 0, \tag{5.9}$$

$$\frac{\partial}{\partial y}(\rho v)(x, -L_y/2, t) = 0, \tag{5.10}$$

$$\frac{\partial}{\partial y}(\rho w)(x, -L_y/2, t) = 0, \tag{5.11}$$

$$\frac{\partial}{\partial y}B_x(x, -L_y/2, t) = 0, \tag{5.12}$$

$$\frac{\partial}{\partial y}B_y(x, -L_y/2, t) = -\frac{\partial}{\partial x}B_x(x, -L_y/2, t), \tag{5.13}$$

$$\frac{\partial}{\partial y}B_z(x, -L_y/2, t) = 0, \tag{5.14}$$

$$\frac{\partial}{\partial y}e(x, -L_y/2, t) = 0 \tag{5.15}$$

for the south boundary and, analogously,

$$\frac{\partial}{\partial y}\rho(x, L_y/2, t) = 0, \tag{5.16}$$

$$\frac{\partial}{\partial y}(\rho u)(x, L_y/2, t) = 0, \tag{5.17}$$

$$\frac{\partial}{\partial y}(\rho v)(x, L_y/2, t) = 0, \tag{5.18}$$

$$\frac{\partial}{\partial y}(\rho w)(x, L_y/2, t) = 0, \tag{5.19}$$

$$\frac{\partial}{\partial y}B_x(x, L_y/2, t) = 0, \tag{5.20}$$

$$\frac{\partial}{\partial y}B_y(x, L_y/2, t) = -\frac{\partial}{\partial x}B_x(x, L_y/2, t), \tag{5.21}$$

$$\frac{\partial}{\partial y}B_z(x, L_y/2, t) = 0, \tag{5.22}$$

$$\frac{\partial}{\partial y}e(x, L_y/2, t) = 0 \tag{5.23}$$

for the north boundary.

5.3 Gas simulation

The 1D initial velocity model has been extended to 2D. First, to allow for a more direct comparison, we set all of the magnetic fields to zero; in other words, we extend the 1D model by adding unmagnetized north and south "lobe" regions. This introduces the second parameter, sheet/lobe temperature ratio τ (since the lobe magnetic field has not been introduced, the lobe beta parameter is set to infinity and left unused). As there is no magnetic field to generate the magnetic pressure component, the pressure balance is achieved by making the initial sheet and lobe pressures equal.

The initial conditions for simulation runs A, B, and C are shown in table 5.2, where the plasma sheet ($\mathbf{U}_\mathrm{L}$, $\mathbf{U}_\mathrm{R}$) quantities are φ_sheet, and the magnetic lobe ($\mathbf{U}_\mathrm{D}$, $\mathbf{U}_\mathrm{U}$) quantities are φ_lobe. The magnetic fields are all set to zero, $\mathbf{B}_\mathrm{sheet} = \mathbf{B}_\mathrm{lobe} = \mathbf{0}$. Each of these configurations was simulated with initial disturbance $\mathbf{U}_\mathrm{L}$, where velocity $u_\mathrm{init} = -1.0$ (left-facing, Earthward flow).

2D plots of density for run B ($\tau = 2.0$, $u_\mathrm{init} = -1.0$) are given in figure 5.3. At time $t = 0$, the left half of the plasma sheet ($x < 0$, $-0.5 < y < 0.5$) begins moving to the left at velocity u_init. This creates a drop in pressure in the center of the plasma sheet, which starts pulling in the surrounding plasma. As a result, a rarefaction wave starts spreading in all directions. The plasma from the right half of the sheet is pulled by the rarefaction wave, lowering pressure and breaking the balance between sheet and lobes.

As the pressure balance is disturbed, lobe plasma starts pushing at the sheet plasma, transforming the rarefaction wave into plasma sheet thinning (figure 5.3(b)). However, due to the inward movement of the lobe plasma, the sheet plasma is compressed, its pressure rises, and the pressure balance between sheet and lobes is quickly re-established. While the rarefaction wave itself continues to propagate in all directions, since the jump between sheet and lobe pressures is lost, there is no further significant inward movement of the sheet–lobe boundary on the right-hand side ($x > 0$) after $t \gtrsim 2.5$ (figures 5.3(d) and (f)).

As can be seen from table 5.2, initial properties of sheet and lobe plasmas for run A are identical. As a result, the rarefaction wave generated by the initial

Run	τ	u_{init}	ρ_{sheet}	p_{sheet}	ρ_{lobe}	p_{lobe}	$c_{\mathrm{s,sheet}}$	$c_{\mathrm{s,lobe}}$
A	1.0	-1.0	1.0	1.0	1.0	1.0	1.29	1.29
B	2.0	-1.0	1.0	1.0	2.0	1.0	1.29	0.91
C	5.0	-1.0	1.0	1.0	5.0	1.0	1.29	0.58

Table 5.2: Initial conditions for the 2D unmagnetized plasma simulations.

velocity spreads evenly in all directions, and since there is no magnetic field in the lobe, plasma sheet thinning does not propagate to the right (tailward).

In run C, the deformation of the boundary progresses through the identical sequence as in run B. However, the development is slightly slower, presumably due to a lower sound velocity in the lobes, in other words, the lower propagation velocity of the lobe rarefaction wave.

5.4 Overview of the plasma simulation

Finally, we introduce the third parameter, lobe plasma beta β_{lobe}, by adding a finite lobe magnetic field. Note that a realistic lobe plasma beta would be on the order of $\beta_{\mathrm{lobe}} \lesssim 0.01$ [46]; however, this is difficult to achieve in a simulation due to the extremely low kinetic pressure in such a plasma (see the last row of table 5.3). Specifically, when the lobe pressure is too low, the simulation code developed for this thesis breaks down and generates non-physical negative pressure. Therefore, for this paper, we limit the values of plasma beta to $\beta_{\mathrm{lobe}} \geq 0.2$, which may be justified a posteriori in the next section.

The addition of the magnetic field to the lobe plasma means that, compared to the gas simulation in section 5.3, the lobe kinetic pressure must be lowered to keep the total pressure constant and the lobe/sheet pressure balanced. An overview of the initial conditions is shown in table 5.3.

2D plots of pressure for run E1 are shown on the left side of figure 5.4. The right side of figure 5.4 shows the profile at $y = 0$ taken from the 2D plasma simulation (orange solid line) and compares it with the time evolution of sheet pressure taken from 1D gas simulation at a grid density of 128 points per unit

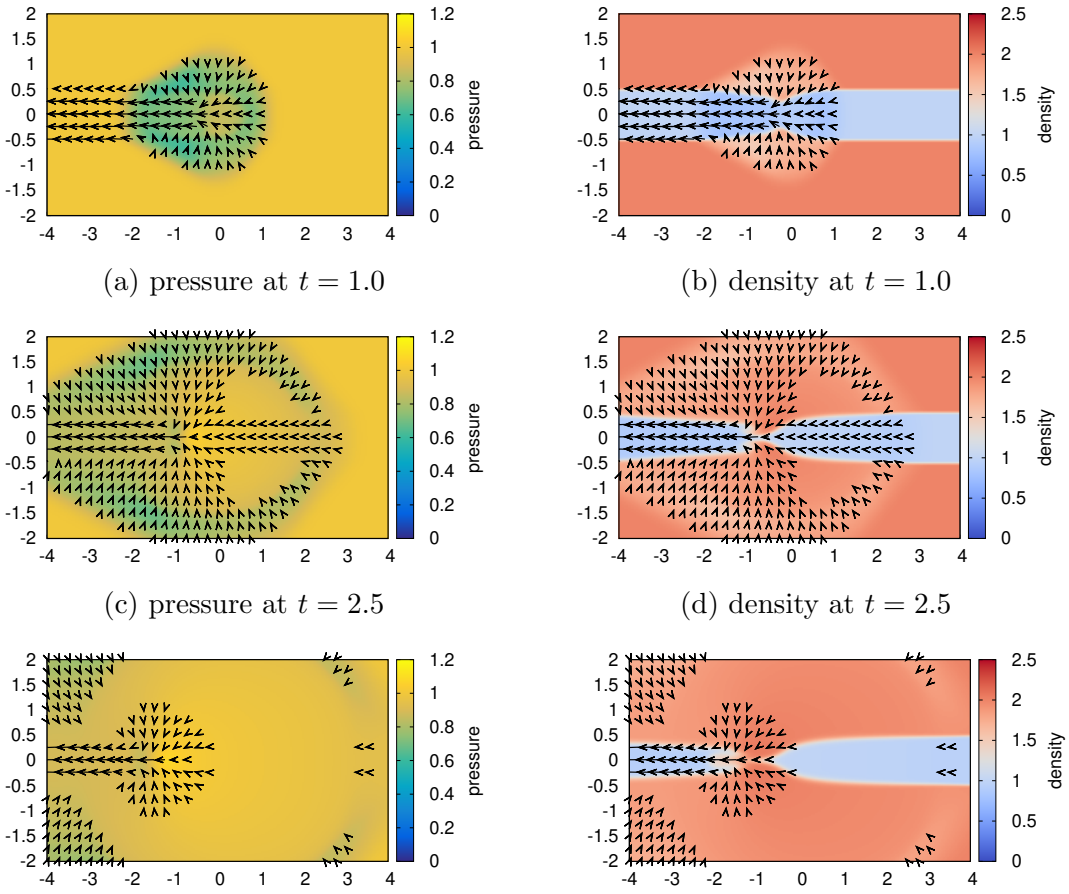

(a) pressure at $t = 1.0$

(b) density at $t = 1.0$

(c) pressure at $t = 2.5$

(d) density at $t = 2.5$

(e) pressure at $t = 4.0$

(f) density at $t = 4.0$

Figure 5.3: Plots of pressure and density evolution for run B ($\tau = 2.0$, $u_{\text{init}} = -1.0$) of the 2D gas simulation with a grid resolution of 32 points per unit length. After an initial set-up period, the thinning does not propagate tailward. Velocity vectors are over-plotted, at a resolution of four vectors per unit length, with velocities below 0.075 not shown for clarity. The length of the vector is proportional to the velocity; note that for velocities near the lower limit, the vector stem is too small to see. Density plots are shown because the shape of the plasma sheet is not visible in the pressure plots, as the initial pressure is uniform.

Run	τ	β_{lobe}	ρ_{lobe}	p_{lobe}	$B_{x,\text{lobe}}$	$c_{\text{s,lobe}}$	$c_{\text{A,lobe}}$
D1	1.0	0.2	0.155	0.155	1.30	1.29	3.30
D2		0.4	0.280	0.280	1.20		2.27
D3		0.7	0.395	0.395	1.10		1.75
D4		1.0	0.500	0.500	1.00		1.41
D5		2.6	0.719	0.719	0.75		0.88
D6		7.0	0.875	0.875	0.50		0.53
D7		31	0.969	0.969	0.25		0.25
D8		199	0.995	0.995	0.10		0.10
E1	2.0	0.2	0.31	0.155	1.30	0.91	2.33
E2		0.4	0.56	0.280	1.20		1.60
E3		0.7	0.79	0.395	1.10		1.24
E4		1.0	1.00	0.500	1.00		1.00
E5		2.6	1.44	0.719	0.75		0.63
E6		7.0	1.75	0.875	0.50		0.38
E7		31	1.94	0.969	0.25		0.18
F1	5.0	0.2	0.78	0.155	1.30	0.58	1.48
F2		0.4	1.40	0.280	1.20		1.01
F3		0.7	1.98	0.395	1.10		0.78
F4		1.0	2.50	0.500	1.00		0.63
F5		2.6	3.59	0.719	0.75		0.40
F6		7.0	4.38	0.875	0.50		0.24
realistic	10.0	0.002	0.02	0.002	1.413	0.40	10.0

Table 5.3: An overview of the initial conditions for 2D plasma sheet simulations. The last row shows the ideal, realistic values, which couldn't be used due to limitations of the simulation program. For all runs, the initial velocity of the disturbance is $u_{\text{init}} = -1.0$, sheet density and pressure are $\rho_{\text{sheet}} = 1.0$, $p_{\text{sheet}} = 1.0$, and sheet sound velocity is $c_{\text{s,sheet}} = 1.29$.

length (black dash-dotted line).

At time $t = 0$, the left half of the plasma sheet begins moving Earthward. The pressure drop that the disturbance leaves behind pulls in the surrounding plasma (figure 5.4(a)). For a few moments ($t \lesssim 0.3$), the resulting rarefaction wave in 2D is similar to the one in the 1D simulation; the remnant of the similarity can be seen as the slope at $0.2 \lesssim x \lesssim 0.8$ in figure 5.4(b). However, as the boundaries with the magnetic lobes move inward due to loss of the pressure balance, the plasma sheet is compressed and the pressure rises; this increase manifests as a bulge at $-0.7 \lesssim x \lesssim 0.2$ in figure 5.4(b). The re-pressurization of the sheet nullifies the rarefaction wave and generates a wave train of pulses of increased pressure (figures 5.4(d) and (f)). The waves in the wave train will be identified as fast-mode MHD waves in section 5.6. Despite the apparent loss of the rarefaction wave, the Earthward plasma flow and the accompanying thinning of the plasma sheet continue. After the initial set-up period at $t \lesssim 1$, the thinning propagates in a self-similar fashion (see figures 5.4(c) and (e)).

Figure 5.5 shows the equivalent plots for run E4, where plasma beta has been increased relative to run E1. 2D plots of pressure are shown on the left side, and the comparison of a profile at $y = 0$ taken from the 2D plasma simulation (orange solid line) with the time evolution of sheet pressure taken from 1D gas simulation (black dash-dotted line) on the right side. General development of the plasma sheet thinning in run E4 follows the same pattern as in run E1. There is an initial pressure drop due to the Earthward flow, generating a rarefaction wave. At $t = 0.5$ (figure 5.5(a)) the rarefaction wave is still visible and identical to the one in the 1D simulation, though soon afterwards it is subsumed in the pressure increase caused by sheet thinning. The wave train generated by sheet re-pressurization (figures 5.5(d) and (f)) is observable, though drastically weaker than in the run E1. It is also clear that increasing the lobe beta (i.e., lowering the lobe magnetic field, which also lowers lobe Alfvén velocity) slowed down the propagation of the thinning front.

Figure 5.6 shows the plots for run F1, where the sheet–lobe temperature ratio has been increased relative to run E1. 2D plots of pressure are again

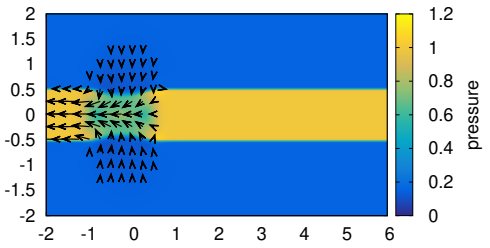

(a) pressure at $t = 0.5$

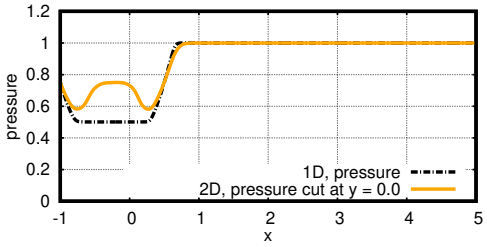

(b) 1D vs 2D at $t = 0.5$

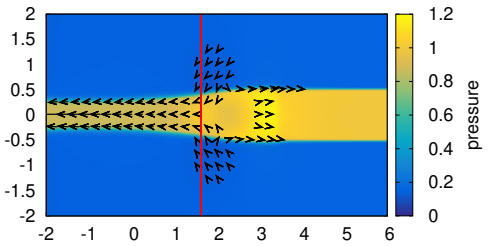

(c) pressure at $t = 2.5$

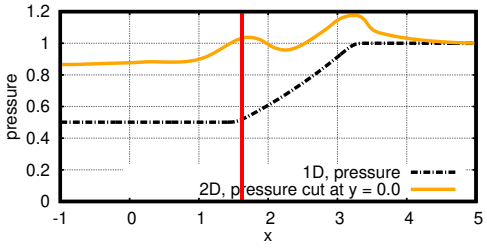

(d) 1D vs 2D at $t = 2.5$

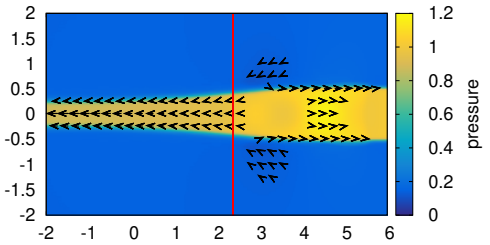

(e) pressure at $t = 4.0$

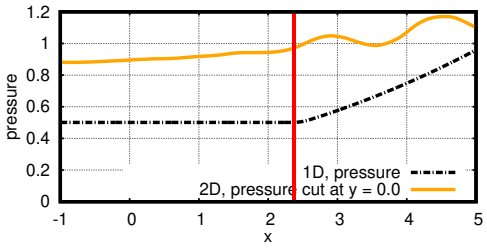

(f) 1D vs 2D at $t = 4.0$

Figure 5.4: Plots of pressure evolution for run E1 ($\tau = 2.0$, $\beta_{\text{lobe}} = 0.2$, $u_{\text{init}} = -1.0$) of the 2D plasma simulation with a resolution of 32 grid points per unit length. (a) shows the initial plasma sheet pressure drop and the beginning of recompression. (c) and (e) show the propagation of the thinning front, with the detected location of the front marked with a red line. Velocity vectors are over-plotted, at a resolution of four vectors per unit length, with velocities below 0.075 not shown for clarity. (b), (d), and (f) show the comparison of pressure in 1D and 2D simulation, with the detected location of the front again marked with a red line. The grid density for 1D simulation is 128 points per unit length. For the 2D simulation, we show the horizontal cut through the center of the plasma sheet, at $y = 0$. (Note that it is only a coincidence that the thinning front and the foot of the 1D rarefaction wave are in approximately the same location. Since the sheet parameters do not change, the 1D rarefaction wave—including the foot—is identical in all of the simulation runs, while the location of the thinning front is different for each run.)

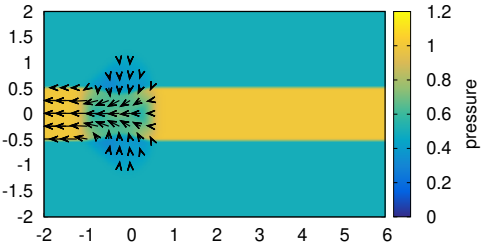

(a) pressure at $t = 0.5$

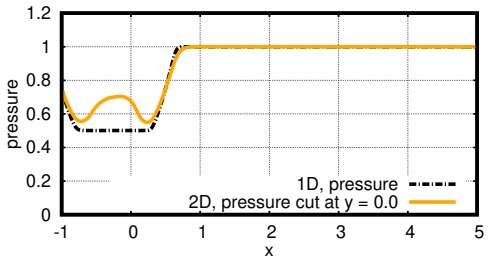

(b) 1D vs 2D at $t = 0.5$

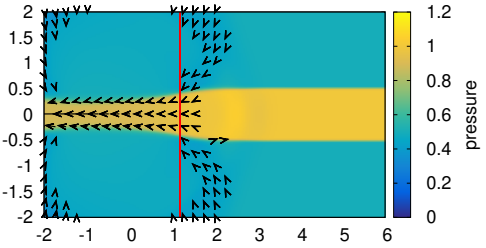

(c) pressure at $t = 2.5$

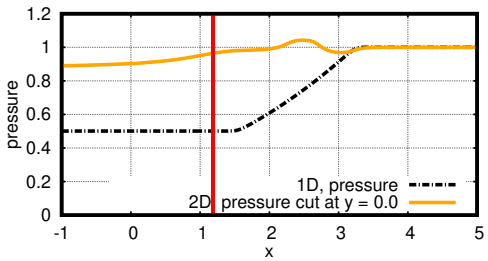

(d) 1D vs 2D at $t = 2.5$

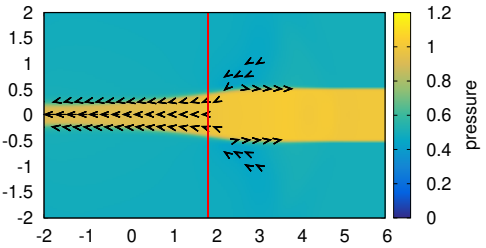

(e) pressure at $t = 4.0$

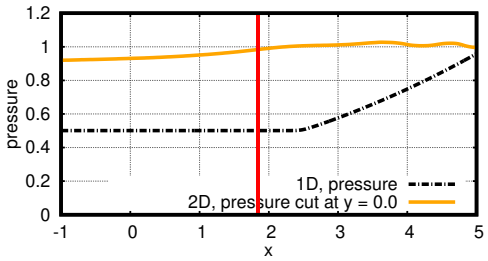

(f) 1D vs 2D at $t = 4.0$

Figure 5.5: Plots of pressure evolution for run E4 ($\tau = 2.0$, $\beta_{\text{lobe}} = 1.0$, $u_{\text{init}} = -1.0$) of the 2D plasma simulation with a resolution of 32 grid points per unit length. (a) shows the initial plasma sheet pressure drop and the beginning of recompression. (c) and (e) show the propagation of the thinning front, with the detected location of the front marked with a red line. Velocity vectors are over-plotted, at a resolution of four vectors per unit length, with velocities below 0.075 not shown for clarity. (b), (d), and (f) show the comparison of pressure in 1D and 2D simulation, with the detected location of the front again marked with a red line.

shown on the left side, and the comparison of a profile at $y = 0$ taken from the 2D plasma simulation (orange solid line) with the time evolution of sheet pressure taken from 1D gas simulation (black dash-dotted line) on the right side. General development of the plasma sheet thinning in run F1 is unchanged from the previous two runs shown. In figure 5.6(a), the rarefaction wave is visible and identical to the one in the 1D simulation, and subsumed soon afterwards. The wave train generated by sheet re-pressurization (figures 5.6(d) and (f)) is much stronger than in the run E4, though still somewhat weaker and slower than in the run E1. The propagation of the thinning front is slightly slower than in the run E1 as well, showing that increasing the sheet–lobe temperature ratio (i.e., increasing the lobe density, which lowers lobe sound and Alfvén velocities) also slows down the propagation of the thinning front.

The other runs listed in table 5.3 follow the same basic sequence of events, albeit with different propagation velocities and thinning amounts. The propagation velocity of the thinning front decreases as lobe beta and temperature ratio τ increase. While the propagation velocity appears to be fairly constant over a single simulation run for sufficiently small β_{lobe}, for lobe plasmas with $\beta_{\mathrm{lobe}} \gg 1$ the measured location of the thinning front may eventually stop advancing, or even slightly reverse direction. This effect is more pronounced in runs with higher temperature ratio τ, where sound and Alfvén velocities in the lobe are lower. Presumably, the physical process that causes the propagation of the thinning front is on a too slow of a timescale for the current simulation. As the actual lobe plasma has $\beta \ll 1$, and the high-beta simulations have been conducted only to determine the overall scaling and confirm it asymptotes towards the "infinite-beta" gas simulation from section 5.3, the affected runs are not required and have been discarded from the overview table and the following analysis.

It is worth noting that we observed the development of Kelvin-Helmholtz (KH) instability on the sheet–lobe interface, arising due to the velocity difference between the two plasmas [47]. However, the instability appears only for the weak magnetic field ($B_{x,\mathrm{lobe}} \lesssim 0.5$, $\beta_{\mathrm{lobe}} \gtrsim 7$), and when it does appear its effect is constrained to the far left of the simulation domain ($x \lesssim -3$), where

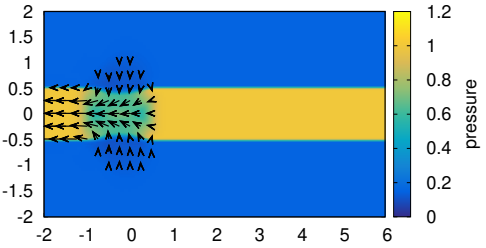

(a) pressure at $t = 0.5$

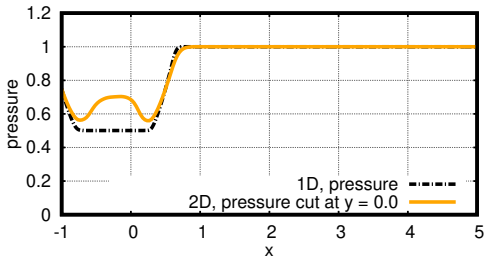

(b) 1D vs 2D at $t = 0.5$

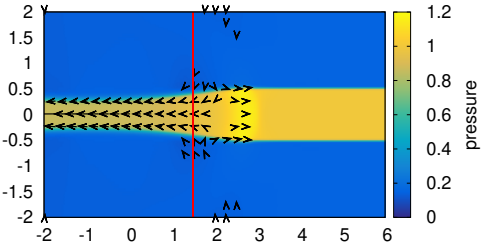

(c) pressure at $t = 2.5$

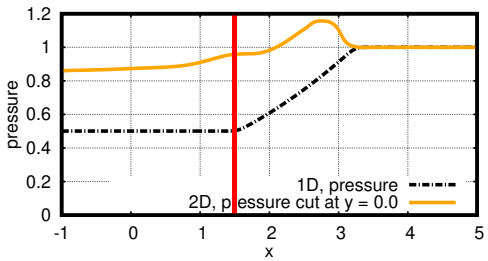

(d) 1D vs 2D at $t = 2.5$

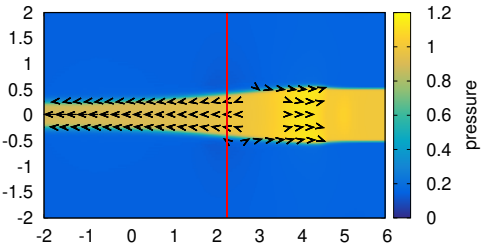

(e) pressure at $t = 4.0$

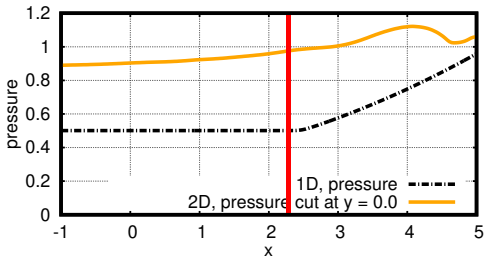

(f) 1D vs 2D at $t = 4.0$

Figure 5.6: Plots of pressure evolution for run F1 ($\tau = 5.0$, $\beta_{\text{lobe}} = 0.2$, $u_{\text{init}} = -1.0$) of the 2D plasma simulation with a resolution of 32 grid points per unit length. (a) shows the initial plasma sheet pressure drop and the beginning of recompression. (c) and (e) show the propagation of the thinning front, with the detected location of the front marked with a red line. Velocity vectors are over-plotted, at a resolution of four vectors per unit length, with velocities below 0.075 not shown for clarity. (b), (d), and (f) show the comparison of pressure in 1D and 2D simulation, with the detected location of the front again marked with a red line.

the velocity difference is significantly larger. As we are only interested in the right side of the domain ($x > 0$), presence of the instability does not affect the following discussions. For a more in-depth discussion of the KH instability, see Appendix D.

Additionally, the flows that can be seen on the sheet–lobe boundary in the right half ($x \gtrsim 2$) of figures 5.4(c) and (e) are due to thin, non-physical jets in the two-grid-points-wide transition area between sheet and lobe, which was introduced to increase the numerical stability of the simulation by slightly smoothing out the initial discontinuity. Increasing the grid density and/or widening the transition area weakens the jets; however, as widening the transition area makes the following analysis more difficult, and the evolution of the plasma sheet shape does not noticeably change, the transition area width was kept at two grid points.

5.5 Thinning front

For further analysis of the plasma sheet thinning, we measure the propagation velocity of its front with the following method. First, for each discrete x coordinate, linearly interpolate the B_x profile to find the location in y where the magnetic field drops below half of the initial lobe value. Collecting all the (x, y) values gives a rough profile of the plasma sheet, which can again be linearly interpolated to obtain the x coordinate of the point where the sheet thickness is reduced to 80% of the initial value. The interpolation procedure is repeated to obtain the "80% thinning" locations between $t = 2$ and $t = 10$ (skipping the initial period at $t < 2.0$ where the self-similar shape of the thinning may not yet be fully developed). Finally, the thinning velocity u_{80} is derived from a linear fit on the "80% thinning" locations. The results for grid density 32 are shown in figure 5.7.

A strong, approximately linear dependence can be observed between the magnetic field strength in the lobes and the thinning velocity. Furthermore, all thinning velocities are considerably slower than the sheet sound velocity. Assuming the linear relationship holds for smaller β_{lobe} (larger $B_{x,\text{lobe}}$), and

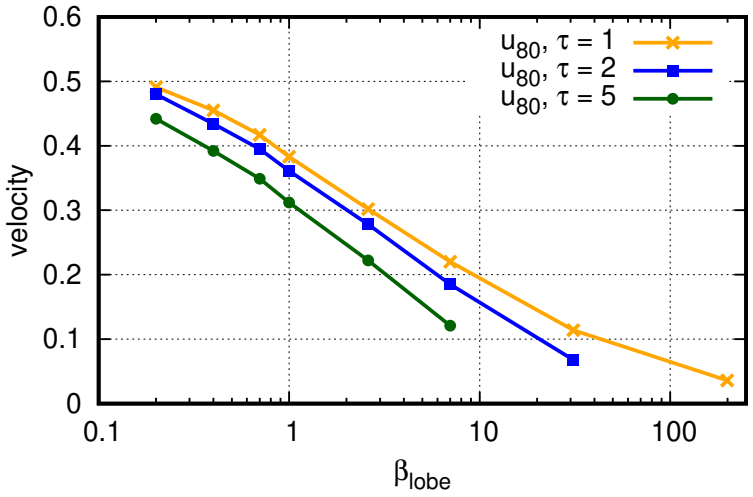

(a) thinning velocity vs plasma beta

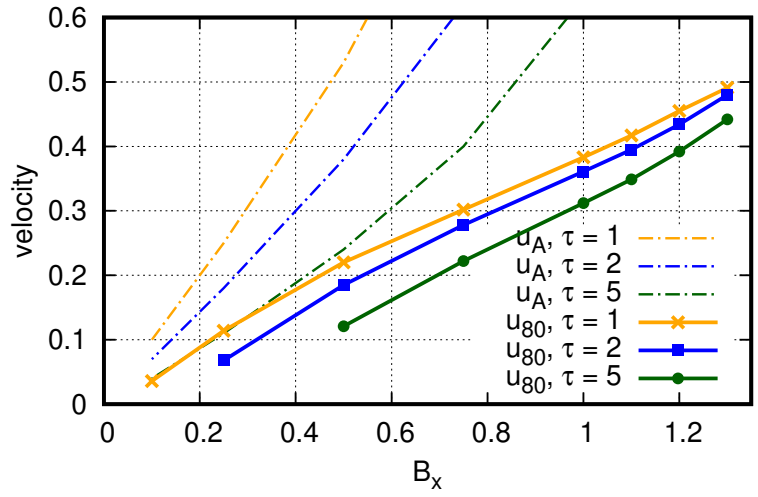

(b) thinning velocity vs B_x

Figure 5.7: Front velocity dependence on the temperature ratio τ and the plasma beta β_{lobe} for 2D simulations with grid density of 32 points, plotted versus lobe beta (top) and the initial lobe magnetic field strength (bottom) with Alfvén velocities for the lobe initial conditions shown for comparison. The relationship between lobe beta and lobe magnetic field is $\beta_{\text{lobe}} = 2/B_{x,\text{lobe}}^2 - 1$.

taking into the account that, in order to satisfy the pressure balance condition (5.1), it has to hold that $B_{x,\text{lobe}} \leq \sqrt{2}$, we can extrapolate that the maximum velocity of the 80% thinning is $u_{80} \sim 0.5$, or less than half of the sheet sound velocity $c_{\text{s,sheet}} = 1.29$.

It may also be illuminating to compare the thinning velocity u_{80} with the typical velocities of the plasma sheet and magnetic lobes. Table 5.4 shows the measured wave velocities and thinning velocity for each of the simulation runs. Note that the values listed in the table are for the undisturbed medium, and will change as the disturbances propagate throughout the domain.

It is clear from the table that none of the wave velocities appear to have a direct relation to the propagation velocity of the thinning front. At first glance it does seem that the Alfvén velocity may have some proportionality; however, in the following section we will see that in this configuration the Alfvén waves do not propagate, which would indicate that the apparent relationship is simply a consequence of both of the velocities being proportional to the lobe magnetic field strength. Divining the mechanism of the plasma sheet thinning will require a more involved analysis.

The fairly smooth dependence of propagation velocity on plasma beta also provides a degree of justification for running the simulations with a higher plasma beta than the actual value in the magnetic lobe. If the physics of the ideal MHD solution was dramatically different depending on the lobe beta, we would expect the critical point to appear around $\beta_{\text{lobe}} = 1$, where plasma behavior typically changes from being dominated by kinetic effects ($\beta_{\text{lobe}} > 1$) to being dominated by magnetic effects ($\beta_{\text{lobe}} < 1$). However, the current problem changes smoothly over the entire range of tested lobe beta values, $199 \geq \beta_{\text{lobe}} \geq 0.2$, which suggests that the trend should hold for $\beta_{\text{lobe}} < 0.2$ as well. Other parameters that may usually cause a dramatic change in plasma behavior when a certain threshold is passed—for example, particle Larmor radius, resistivity, etc.—are not directly used in the ideal MHD equations used in this thesis, and therefore will not influence the simulation results. They may, of course, mean that the ideal MHD approximation is no longer valid; however, the approximation is supposed to hold in the current regime, and if

Run	τ	β_{lobe}	$c_{\mathrm{s,lobe}}$	$c_{\mathrm{A,lobe}}$	$c_{\mathrm{sm,lobe}}$	$c_{\mathrm{fm,lobe}}$	$c_{\mathrm{s,sheet}}$	u_{80}
D1	1.0	0.2	1.29	3.30	1.29	3.30	1.29	0.49
D2		0.4		2.27	1.29	2.27		0.46
D3		0.7		1.75	1.29	1.75		0.42
D4		1.0		1.41	1.29	1.41		0.38
D5		2.6		0.88	0.88	1.29		0.30
D6		7.0		0.53	0.53	1.29		0.22
D7		31		0.25	0.25	1.29		0.11
D8		199		0.10	0.10	1.29		0.036
E1	2.0	0.2	0.91	2.33	0.91	2.33	1.29	0.48
E2		0.4		1.60	0.91	1.60		0.43
E3		0.7		1.24	0.91	1.24		0.40
E4		1.0		1.00	0.91	1.00		0.36
E5		2.6		0.63	0.63	0.91		0.28
E6		7.0		0.38	0.38	0.91		0.19
E7		31		0.18	0.18	0.91		0.068
F1	5.0	0.2	0.58	1.48	0.58	1.48	1.29	0.44
F2		0.4		1.01	0.58	1.01		0.39
F3		0.7		0.78	0.58	0.78		0.35
F4		1.0		0.63	0.58	0.63		0.31
F5		2.6		0.40	0.40	0.58		0.22
F6		7.0		0.24	0.24	0.58		0.12

Table 5.4: Comparison of wave velocities with the thinning velocity u_{80} for 2D plasma sheet simulations. The thinning velocities u_{80} are the values obtained with the grid density of 32 points per unit length. The wave velocities shown are the lobe sound velocity $c_{\mathrm{s,lobe}}$, lobe Alfvén velocity $c_{\mathrm{A,lobe}}$, slow and fast lobe magnetosonic velocities $c_{\mathrm{sm,lobe}}$ and $c_{\mathrm{fm,lobe}}$, and finally sheet sound velocity $c_{\mathrm{s,sheet}}$.

those ranges of values *are* present, they're out of scope of this thesis to begin with. Therefore, we can conclude that, while the actual lobe beta is $\beta_{\text{lobe}} < 0.1$, it is almost certainly valid to base the analysis on the results for the lobe beta values $\beta_{\text{lobe}} \geq 0.2$, extrapolating if needed.

Finally, in order to show numerical convergence, the comparison between grid densities for temperature ratio $\tau = 2$ is shown in figure 5.8. We can see a good agreement between grid densities 16 and 32, and an excellent agreement between grid densities 32 and 64. More specifically, for $\beta_{\text{lobe}} \leq 7$ ($B_{x,\text{lobe}} > 0.5$), the disagreement in thinning velocity between grid densities 16 and 32 is below 4%, and the disagreement between grid densities 32 and 64 is below 2%. The convergence worsens for $\beta_{\text{lobe}} > 7$, as determining the thinning velocity grows less reliable and requires more grid density as that velocity nears zero. However, lobe plasma is a low-beta plasma, and the simulations for $\beta_{\text{lobe}} > 1$ are used only to confirm that the thinning velocity goes to zero as lobe beta rises (as anticipated from the 2D gas simulation); therefore, somewhat rough results for high values of lobe beta are acceptable.

5.6 Wave decomposition

One possible approach that can be used to determine the physical process behind an event in a system of conservation laws is to decompose the disturbances into component waves. The decomposition may be obtained by the same approach as in the simulation code: splitting the 2D problem into mutually independent collections of 1D problems for each x and y coordinate of the original system (see section 3.1.6), and diagonalizing the obtained 1D MHD equations using the procedure described in section 2.6.2.

The diagonalized system can be written as

$$\frac{\partial(L\mathbf{U})}{\partial t} + \frac{\partial(L\mathbf{F})}{\partial x} = 0, \tag{5.24}$$

where $L = (\mathbf{L}_1, \cdots, \mathbf{L}_k)$ is a matrix of left eigenvectors $\mathbf{L}_1, \ldots, \mathbf{L}_k$ of the system's Jacobian, $\partial\mathbf{F}/\partial\mathbf{U}$. To reiterate, as the left eigenvectors of the MHD equations are not constant but a function of $\mathbf{U}$, the diagonalization procedure,

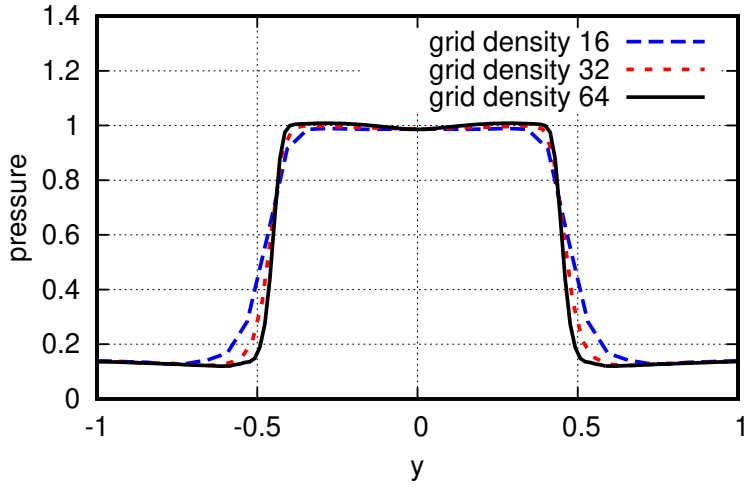

(a) pressure profiles for run E1 at $x = 2.0$

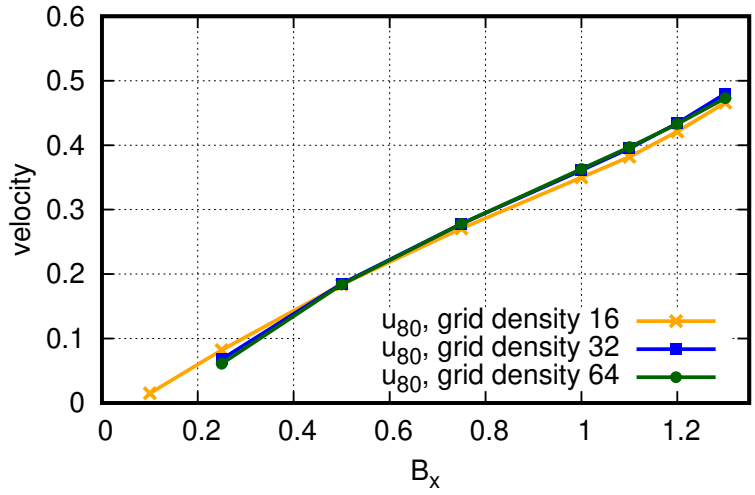

(b) thinning velocity vs B_x

Figure 5.8: Comparisons between simulation results with different grid densities. Pressure profiles of the plasma sheet are increasingly smeared out as grid density falls (top), though the sheet width is consistent. The impact of the minor width variation on measured thinning velocity is low (bottom).

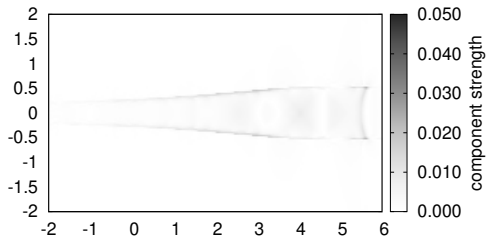

(a) fast-mode wave in the positive x direction

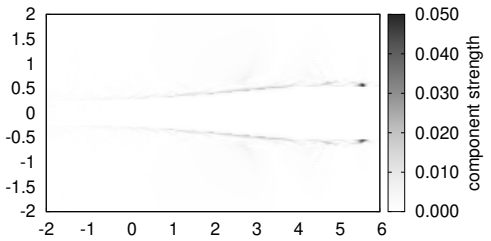

(b) slow-mode wave in the positive x direction

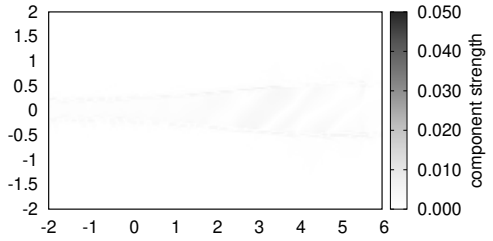

(c) fast-mode wave in the negative y direction

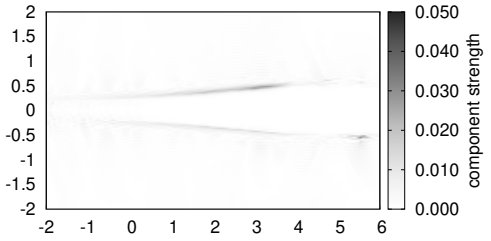

(d) slow-mode wave in the negative y direction

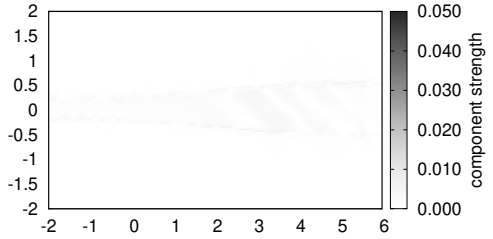

(e) fast-mode wave in the positive y direction

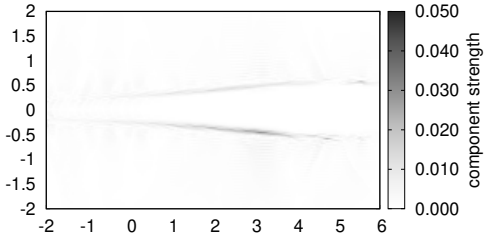

(f) slow-mode wave in the positive y direction

Figure 5.9: Wave strengths $|S_{j+\frac{1}{2},i}|$ at time $t = 4.0$ for run E1 ($\tau = 2.0$, $\beta_{\text{lobe}} = 0.2$, $u_{\text{init}} = -1.0$) of the 2D plasma simulation with a resolution of 32 grid points per unit length. All plots are scaled to the same value to allow for relative comparison; see figure 5.10 for a clearer representation of individual plots.

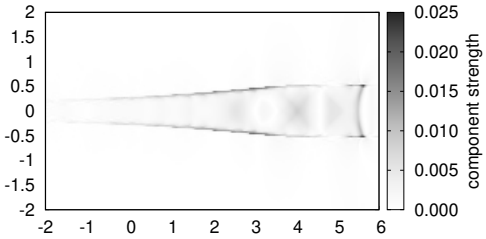

(a) fast-mode wave in the positive x direction

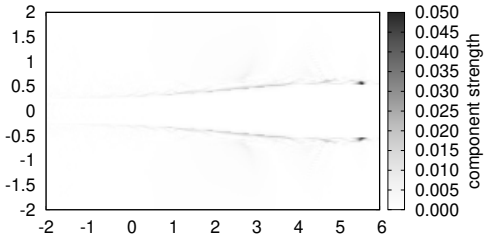

(b) slow-mode wave in the positive x direction

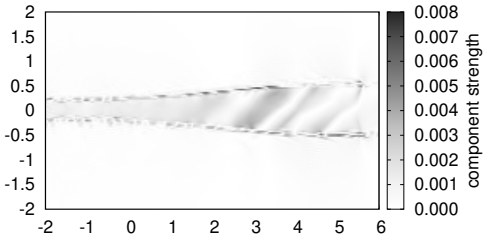

(c) fast-mode wave in the negative y direction

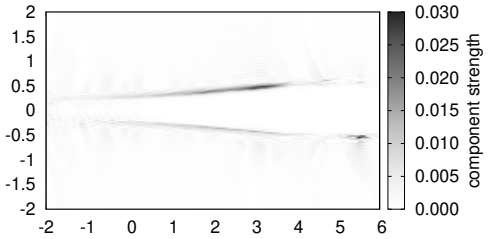

(d) slow-mode wave in the negative y direction

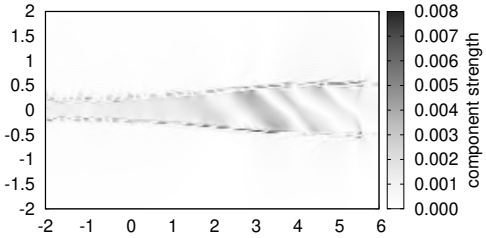

(e) fast-mode wave in the positive y direction

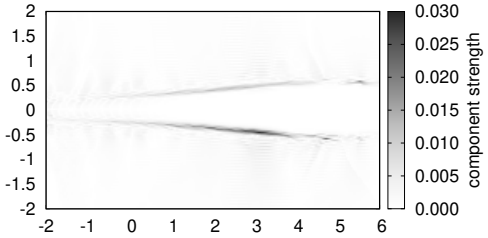

(f) slow-mode wave in the positive y direction

Figure 5.10: Wave strengths $|S_{j+\frac{1}{2},i}|$ at time $t = 4.0$ for run E1 ($\tau = 2.0$, $\beta_{\text{lobe}} = 0.2$, $u_{\text{init}} = -1.0$) of the 2D plasma simulation with a resolution of 32 grid points per unit length. All plots are scaled to their own maximum value; see figure 5.9 for a comparison between different wave modes.

and by extension the wave decomposition described here, is an approximation obtained by locally freezing the value of L. System (5.24) can be split into a set of k independent advection equations

$$\frac{\partial w_i}{\partial t} + \lambda_i \frac{\partial w_i}{\partial x} = 0, \tag{5.25}$$

where w_i $(i = 1, \ldots, k)$ are components of the transformed vector $\mathbf{W} = L\mathbf{U}$, and λ_i are the respective eigenvalues corresponding to the left eigenvectors $\mathbf{L}_i$. It follows that an approximate strength of each wave component can be calculated by discretizing the transformed flux $L\mathbf{F}$ from (5.24).

We define the decomposition of wave components $\mathbf{S}_{j+\frac{1}{2}}$ between grid points j and $j+1$ as

$$\mathbf{S}_{j+\frac{1}{2}} = L_{j+\frac{1}{2}}(\mathbf{F}_{j+1} - \mathbf{F}_j), \tag{5.26}$$

where $L_{j+\frac{1}{2}} = L(\mathbf{U}_{j+\frac{1}{2}})$ is the discretized, locally frozen value of the matrix of the left eigenvectors L between grid points j and $j+1$, with $\mathbf{U}_{j+\frac{1}{2}}$ calculated by averaging density, velocity, magnetic field, and total pressure of $\mathbf{U}_j$ and $\mathbf{U}_{j+1}$ [32], and $\mathbf{F}_j = \mathbf{F}(\mathbf{U}_j)$ is the discretized flux at grid point j. Then, absolute values $S_{j+\frac{1}{2},i}$, where $i = 1, \ldots, k$ and $\mathbf{S}_{j+\frac{1}{2}} = (S_{j+\frac{1}{2},1}, \ldots, S_{j+\frac{1}{2},k})$, can be interpreted as relative strengths of the k wave components.

Figure 5.9 shows the wave components $|S_{j+\frac{1}{2},i}|$ in x and y directions around the thinning front of the plasma sheet for run E1, with other components being at most half as large as the maximum of the positive-direction fast-mode component (≈ 0.025), which is half as large as the peaks of the slow-mode component (≈ 0.050). Figure 5.10 shows the same components, rescaled to better show their structure.

A wave train of fast-mode MHD waves (i.e., sound waves) propagating tailward at sound velocity can be observed inside of the plasma sheet in figure 5.10(a), with peaks and troughs that roughly align with, respectively, troughs and peaks of pressure in figure 5.4(f). There also appears to be a slow-mode MHD wave propagating in the x direction along the sheet–lobe boundary, visible as a peak at $(x, y) \approx (5.6, \pm 0.5)$ in figure 5.10(b). However, the slow-mode peak is not moving at the lobe slow magnetosonic speed

of 0.91, but instead moves at the sheet fast magnetosonic speed (i.e., sound speed) of 1.29, advancing together with the dark arc-like structure at the front of the plasma sheet wave train at $x \approx 5.5$. Since there is a sharp change at the exact point of the sheet–lobe interface when crossing between sheet and lobe, where the fast-mode component (the dark arc) suddenly weakens and the slow-mode component (the peaks) grows, it is likely that the slow wave is generated through mode conversion by the front of the fast-mode wave-train as it touches the boundary.

From the decomposition in the y direction, in figures 5.10(d) and (f) we can observe a strong slow-mode component along the sheet-lobe boundary when crossing from lobe to sheet. As the plasma changes from the strongly magnetized lobe plasma into non-magnetized sheet plasma, the slow magnetosonic speed falls to zero and the slow wave at the boundary is unable to enter the sheet. Instead, it appears to launch a series of fast-mode waves across the sheet, clearly visible in figures 5.10(c) and (e). The location of the peak of the y direction slow-mode wave corresponds to the thinning front of the plasma sheet, suggesting that the slow-mode wave may be driving the thinning process.

Comparing the wave components in figure 5.10 with the pressure plots in figure 5.4, we can see that, while the x direction wave train moves at the same velocity as the rarefaction wave in the 1D model, it causes the sheet pressure to increase instead of decrease, resisting the deformation of the magnetic field lines. After the pulses of increased pressure associated with the wave train pass, the sheet–lobe boundary starts moving inward and the thinning begins, as can be seen from the y-direction slow-mode MHD waves in figures 5.10(d) and (f). The wave train appears to be influenced by the slow-mode wave at the sheet-lobe boundary; as the y direction fast-mode waves move across the sheet, new waves are generated slightly tailwards, giving the appearance of a right-moving stripe. The first pulse in the wave train is generated during the initial sheet recompression, as can be seen in figure 5.4(b).

It is worth noting that there were no Alfvén waves detected by the wave decomposition procedure, down to the level of the numerical error. This sug-

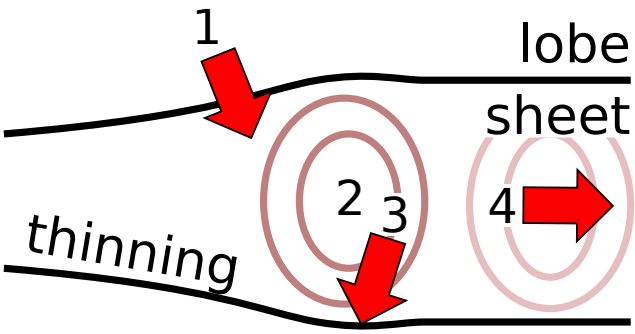

Figure 5.11: Mechanics of the plasma sheet thinning. As the sheet pressure drops, the balance breaks and the sheet-lobe boundary moves inwards (1). This compresses the sheet, raising pressure (2) and resisting the thinning (3). Finally, the pulse of increased pressure is launched tailwards (4), and the thinning can resume (1).

gests that the y direction slow-mode waves are the primary driver behind the bending of the magnetic field lines during the thinning process.

5.7 Mechanics of the thinning process

The results of the wave decomposition begin to paint the picture of a possible process behind plasma sheet thinning in a 2D sheet configuration. The stages are shown in figure 5.11.

Initially, there is a drop in pressure caused by the Earthward plasma flow, a disturbance that was assumed to be caused by the near-Earth current disruption. The sheet-lobe pressure balance is broken, and the boundary moves inwards, towards the center of the sheet, causing thinning to begin (1). At the same time, the pressure drop launches a rarefaction wave (fast mode magnetosonic wave) in all directions. As the y direction rarefaction wave hits the sheet-lobe boundary, the fast mode wave partially reflects, partially crosses over into the lobe, and partially converts into a slow mode magnetosonic wave.

The inward movement of the boundary compresses the sheet plasma, raising

the sheet pressure (2). The reflected fast mode components propagate back towards the opposite sheet-lobe boundaries. Increased sheet pressure pushes back on the boundary, resisting further deformation and slowing down the thinning (3).

Finally, the area of increased pressure moves tailward (4), the pressure drops again, and the thinning resumes (1). The tailward flow manifests as a fast mode magnetosonic wave, and appears to be the combined x components of fast mode waves reflected from upper and lower sheet-lobe boundaries. The y components, on the other hand, have similar strengths and opposite directions, so their effect while propagating through the sheet is minimal. However, once they hit the boundary, they initiate a mode conversion into the slow wave, generating a B_y component of the magnetic field and bending the magnetic field lines inwards; in other words, causing the sheet-lobe boundary to move and causing thinning.

5.8 Comparison of 1D and 2D models

In the 1D gas model by Chao *et al.* [7], the movement of the imaginary piston generates a rarefaction wave traveling tailward. The thinning proceeds in two distinct stages. First, due to the propagation of the rarefaction wave, pressure in the sheet is reduced. Second, due to the broken pressure balance between sheet and lobes, the sheet-lobe boundary is forced to move inward, causing the thinning. Since the plasma beta in the sheet is greater than one, the rarefaction wave moves at the sound velocity, $c_{\mathrm{s,sheet}}$. Chao *et al.* [7] do not explicitly state the propagation velocity of the thinning; however, as the compression is calculated from the plasma state after the rarefaction is completed, we can deduce that the propagation velocity is at most as large as the propagation velocity of the rarefaction wave's foot. From the exact solution (4.1) for the plasma velocity, we can see that the foot of the rarefaction wave propagates at

$$u_{\mathrm{foot}} = \left(c_{\mathrm{s},0} + \frac{\gamma + 1}{2} u_{\mathrm{p}} \right), \tag{5.27}$$

where $c_{s,0}$ is the sound velocity of the initial state, and $u_p < 0$ is the velocity of the imaginary piston. Taking $\gamma = 5/3$ and $u_p = 0.8c_{s,0}$, the representative value from the reference paper, we obtain $u_{foot} = -c_{s,0}/15$; in other words, the foot of the rarefaction wave slowly moves *Earthward*. Therefore, it would appear that—despite the presumed two-stage process—thinning is assumed to proceed at the same velocity as the rarefaction wave. Furthermore, while it is discussed how different treatments of the magnetic flux may change the amount of thinning, from which we can conclude that changes in the lobe magnetic field may do so as well, there is no mention that the thinning front velocity may depend on the conditions in the magnetic lobes.

Extending the 1D model to a 2D gas model, we observed that the rarefaction wave generated by the initial disturbance is drastically weakened in the first moments of the event. Furthermore, even though this weakened form of the rarefaction wave continues propagating, the thinning ceases to propagate due to the loss of the sheet–lobe pressure difference (see figure 5.3).

Extending to a 2D plasma model by introducing the magnetic field into the lobes, the dynamics of the plasma sheet thinning drastically changes.

Firstly, the rarefaction wave is weakened so much that it is no longer clearly noticeable as an independent entity. It is either subsumed in other, stronger waves, or almost completely extinguished by compression in the first few moments of the event. In either case, the significant drop in pressure ceases to propagate tailward. However, despite the lack of a significant pressure drop, and in stark contrast to the 2D gas model, the thinning continues to propagate (figure 5.4). This indicates that the rarefaction wave is not a sole component of the plasma sheet thinning.

Secondly, the thinning front velocity is lower than the rarefaction wave velocity. This is another indicator that thinning dynamics have separated from the rarefaction wave that initially caused them.

Thirdly, the thinning front velocity shows a strong dependence on the conditions in the magnetic lobes (figure 5.7). The thinning front propagates faster when the lobe magnetic field is stronger, in stark contrast to the 1D model. As the 2D gas simulation showed, in the limit of no magnetic field there is an

initial burst after which the thinning front completely stops propagating; this aligns with the small B_x limit of the 2D plasma simulation.

Fourthly, in the 2D plasma model there is a wave train of slight pressure increases moving tailward through the plasma sheet at the fast magnetosonic (i.e., sound) velocity (figure 5.4). The wave train is completely absent in the 1D and 2D gas models.

The above points of comparison clearly show that the dynamics of plasma sheet thinning seem to be dominated by the sheet–lobe interaction that could not be accounted for in the 1D model.

As mentioned in section 1.2.4, the CD model employs the rarefaction wave and the resulting pressure drop to trigger near-Earth reconnection. That is, the rarefaction wave needs to propagate tailward for a long distance; for example, from the site of current disruption ($\sim -10R_{\mathrm{E}}$) to that of reconnection ($\sim -20R_{\mathrm{E}}$), which are approximately $10R_{\mathrm{E}}$ apart. In the current simulation study, however, the rarefaction wave and, more importantly, corresponding pressure drop are damped soon after the occurrence of pressure decrease due to current disruption. Therefore, the mechanism described in the CD model may be insufficient to trigger reconnection because of the weakening of pressure decrease in the central plasma sheet at $\sim -20R_{\mathrm{E}}$. In this sense, the results of the numerical simulation suggest that the CD model may need to be carefully reconsidered to account for magnetic reconnection, as the current form may not be able to fully explain all the phenomena in the magnetotail during the episode of auroral substorm.

Finally, returning the normalized values back to real ones according to table 5.1, we can see that a normalized thinning velocity of ~ 0.6 translates into ~ 400 km/s. To traverse the aforementioned $10R_{\mathrm{E}}$, which is a distance of ~ 3.3 in the normalized units, between the site of current disruption to that of reconnection, the thinning front in the simulation would require $t_{\mathrm{total}} \approx 3.3/0.6 \approx 5.5$ (~ 2.75 min). At time $t = 4$ (~ 2 min), the sheet thickness at $x = 0$ is reduced by 50%, from the initial $\sim 3R_{\mathrm{E}}$ to $\sim 1.5R_{\mathrm{E}}$.

As already mentioned in Chapter 1, observational data of the plasma sheet during substorm events is relatively scarce—especially considering that deter-

mining the spatial and temporal relation between the CD, thinning, and reconnection requires numerous observations over a distance spanning $\sim 10R_{\rm E}$. One such fortuitous case, with 11 satellites present in the nightside magnetosphere during a substorm event, occurred in October 2004; a detailed account of the observations was given by Lui *et al.* [48]. Data from a couple of satellites, Double Star 1 (TC-1) and Cluster, is particularly relevant to the present discussion. A disturbance in the magnetic field that can be interpreted as plasma sheet thinning was observed first by TC-1, and then 1.5 min later by Cluster, which was located $\sim 3R_{\rm E}$ down tail from TC-1. (Note that this is a distance in the x direction; at the time, TC-1 was $\sim 3R_{\rm E}$ south of the equatorial plane, while Cluster was $\sim 5R_{\rm E}$ north. Nevertheless, the x distance should be a decent approximation to the actual distance covered by the presumed thinning front.) It is easily calculated that the observed thinning front would cover a distance of $10R_{\rm E}$ in ~ 5 min, moving at a velocity of ~ 200 km/s. These values are within a factor of two of the results obtained from the simulation, which is close enough to be plausible.

Chapter 6

Conclusion

There are several competing models attempting to explain the process leading to auroral breakup. Currently, the preferred model is the Near-Earth Neutral Line (NENL) model, with the Current Disruption (CD) model a distant second. However, determining the validity of either model is exceedingly difficult due to the scale of the physical events involved. While there is some observational data thanks to a number of satellites moving through the affected region, it has so far been insufficient to conclusively confirm or deny either of the models. The main issue is that the auroral breakup appears to be connected to a large-scale reconfiguration of the Earth's plasma sheet, where the distances involved are on the order of 10–100R_{E}, while the most the satellites can provide is data on specific physical properties at a single point. The overall behavior of the plasma sheet has to be inferred by interpreting the limited data and building a self-consistent global picture. Numerical simulations provide a useful tool for analyzing whether the model is consistent with the available observations.

In this thesis, a one-dimensional (1D) model for thinning of the Earth's plasma sheet according to the CD model of auroral breakup introduced by Chao *et al.* [7] has been extended to a simple 2D configuration. An initial disturbance launches a rarefaction wave, which is a signature component of the CD model. In the original 1D gas model, the rarefaction wave propagates tailward at sound velocity; the resulting drop in pressure is assumed to cause plasma sheet thinning. In the extended 2D *gas* model, the rarefaction wave

is weakened, and the plasma sheet thinning is absent. In the extended 2D *plasma* model, where magnetic field was added into the lobes, the rarefaction wave is quickly lost in the plasma sheet recompression. However, the plasma sheet thinning reappears, propagating at a slower velocity than the 1D model suggests. The thinning is preceded by a wave train of pulses of increased pressure, generated by the thinning process itself. The stark changes as the model is expanded suggest that the dynamics of plasma sheet thinning may be dominated by sheet–lobe interactions that are absent from the 1D model.

In Chapter 1, we gave a brief introduction and an overview of the thesis, followed by a short description of the Earth's magnetosphere, geomagnetic substorms, and the two main models of auroral breakup (NENL and CD). In Chapter 2, we have introduced the magnetohydrodynamic (MHD) equations, their properties, and their formulation as a conservation law. In Chapter 3, we have described the simulation scheme and touched upon the implementation of the simulation code used in this thesis. In Chapter 4, we have presented the 1D piston model by Chao *et al.* [7], and constructed an alternative formulation that is easier to extend, where the piston is replaced by initial velocity. In Chapter 5, we have extended the model to a 2D configuration, simulated it, and analyzed the results.

We have first extended the aforementioned simple 1D model of the plasma sheet thinning to a 2D configuration by adding unmagnetized north and south "lobes". In the 2D gas simulation the rarefaction wave is weakened and thinning ceases to propagate (figure 5.3). After adding a magnetic field to the lobes and simulating the resulting 2D plasma model, the thinning begins to propagate once more, though this time the rarefaction wave is absent (figure 5.4).

The lack of thinning propagation in the 2D gas simulation means that the influence of the sheet–lobe configuration on the dynamics can be too strong to allow extrapolating the behavior from a 1D model. The appearance of thinning in the 2D plasma simulation indicates that the deformation of the magnetic field may play a significant role in the plasma sheet thinning. This conclusion is strengthened by observing that the signature aspect of the CD model of the auroral breakup, the rarefaction wave, as well as its associated pressure drop,

are drastically weakened soon after the event begins, and the thinning, which was supposed to be following behind the—now absent—rarefaction wave, continues propagating, though at a slower velocity. The thinning is preceded by a wave train of pulses of increased pressure, propagating tailward as fast-mode MHD waves. The thinning begins after the wave train passes, and its velocity is shown to be strongly influenced by the conditions in the magnetic lobes; in particular, there is an approximately linear dependence on the lobe magnetic field strength.

Finally, the weakening or outright disappearance of the rarefaction wave and the presence of the wave train indicate that it is possible that the reconnection in the CD model may not be preceded by a significant drop in pressure. On the contrary, the simplified model used in the simulation suggests that the reconnection may even be preceded by a slight pressure *increase* in the center of the plasma sheet. This creates problems for satellite observations attempting to determine the validity of the CD model, as the rarefaction wave and the associated pressure drop were assumed to be the signature of the model. The simulation results presented here indicate that determining which of the auroral breakup models is correct may instead require reconstructing the wide-area configuration of the plasma sheet, which in turn would require a large number of satellites. Additional simulations of candidate models may point at other unique characteristics that could simplify the search once more; however, what those may be is currently unknown.

As we have seen, expanding the 1D model to 2D and introducing the relevant structure of the plasma sheet has dramatically changed the results. It follows that expanding the model once again, to three dimensions, may also have a dramatic effect on the results. On the other hand, the remaining direction (east-west) is a fair bit more uniform than the one introduced here (north-south); therefore, we do not expect *as* much of a divergence. Nevertheless, finding local characteristics that could distinguish the candidate models of auroral breakup may require a global 3D simulation of the CD model, which currently appear to be lacking, that could be compared to global simulations of the NENL model.

It is worth noting that the ideal MHD model employed in the simulation is unable to reproduce the magnetic reconnection, and therefore does not address the development of the system after the thinning of the plasma sheet. A more sophisticated simulation model, e.g., the extended MHD or a kinetic model, would be required to determine whether the reconnection ultimately does or does not occur under the simplified geometry used in this paper.

In future research, we hope to more precisely determine the dependence of the plasma sheet thinning on the parameters of the plasma sheet and magnetic lobes. We would also like to confirm whether or not the reconnection can occur if the presented plasma sheet configuration is simulated with a more sophisticated simulation model.

Appendix A

Order of the simulation scheme

In this section, we analyze the order of the numerical schemes used for the simulations in this thesis. The schemes themselves have already been introduced in section 3.1; spatial integration was calculated with the ENO-LF scheme, and time integration with the three-step Runge-Kutta method.

A.1 Order of the three-step TVD Runge-Kutta method

Taking the optimal three-step TVD Runge-Kutta method [35] (RK3) introduced in section 3.1.5, and rewriting it for a 1D scalar function $u(t)$, we obtain

$$\begin{aligned} u^{(1)} &= u^n + \Delta t f(u^n) \\ u^{(2)} &= \frac{3}{4}u^n + \frac{1}{4}u^{(1)} + \frac{1}{4}\Delta t f(u^{(1)}) \\ u^{n+1} &= \frac{1}{3}u^n + \frac{2}{3}u^{(2)} + \frac{2}{3}\Delta t f(u^{(2)}), \end{aligned} \tag{A.1}$$

where u^n and u^{n+1} are the discretized values of u at points t_n and t_{n+1}, and $u^{(1)}$ and $u^{(2)}$ are the state vectors of the intermediate steps. We arbitrarily choose

$$u(t) = \exp(t) \tag{A.2}$$

$$f(u) = u'(t) = u(t) \tag{A.3}$$

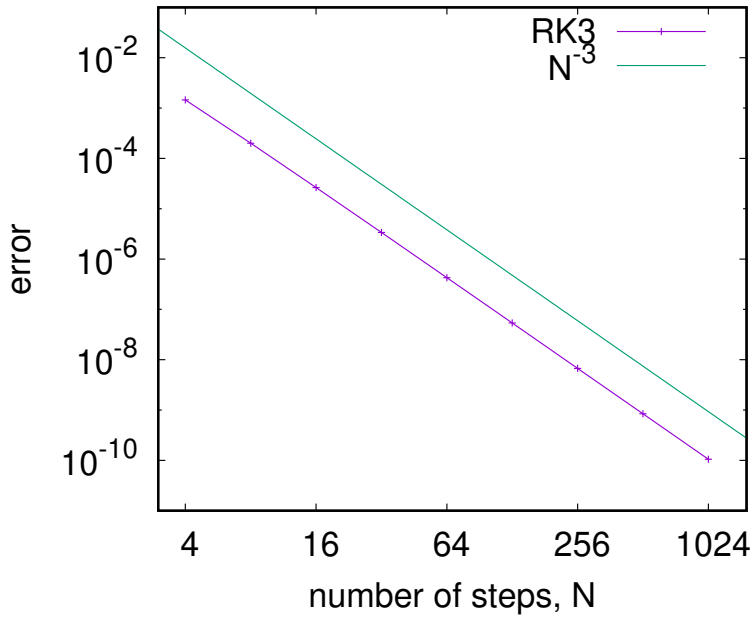

Figure A.1: Error for the RK3 method, with number of steps N on the horizontal axis and error $|u^{n_{\max}} - u(t_{\max})|$ on the vertical axis. A line with the slope N^{-3} is shown for comparison.

as the test function, with initial value

$$u(0) = 1, \tag{A.4}$$

and apply the scheme in (A.1).

The results of the numerical simulation are shown in figure A.1, with the error calculated as

$$\text{err} = |u^N - u(t_{\max})|, \tag{A.5}$$

where u^N is the result of the simulation after N steps of $\Delta t = t_{\max}/N$, and $u(t_{\max})$ is the exact value of $u(t)$ at $t_{\max} = 1.0$. Comparing with the line of slope N^{-3}, we can see that the RK3 method used in the MHD simulation is of a third order.

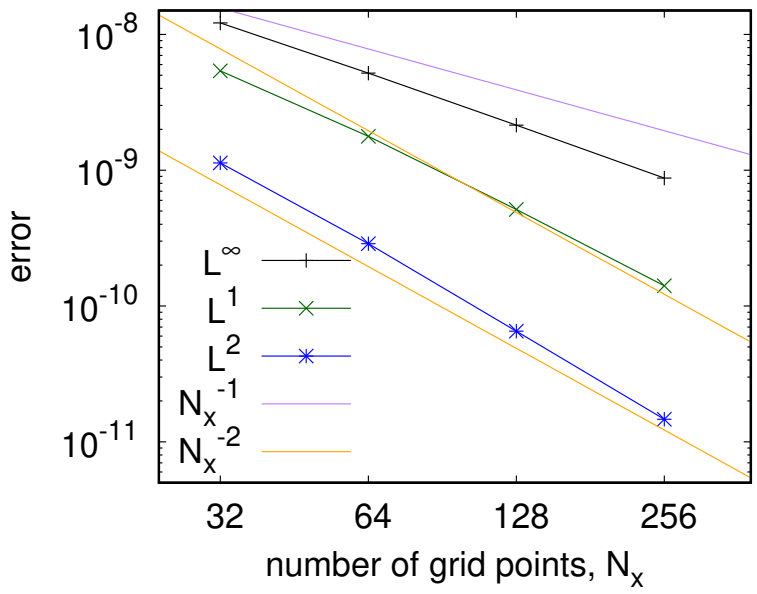

Figure A.2: The L^1, L^2, and L^∞ errors for the ENO-LF scheme, with number of grid points N_x on the horizontal axis and errors on the vertical axis. Two lines, with slopes N_x^{-1} and N_x^{-2}, are shown for comparison.

A.2 Order of the ENO-LF scheme

The ENO scheme is highly nonlinear even for linear problems [33], and it is not possible to analytically obtain the scheme's convergence rate [49]. Therefore, the convergence rate is typically obtained empirically, with numerical experiments.

As the construction of the ENO-LF scheme depends heavily on the equation it is being applied to, it is significantly more difficult to implement in isolation, and there is a risk that the resulting scheme will have different properties than the one used in the simulation itself. Therefore, the order of the ENO-LF scheme for spatial integration has been tested with the full simulation code, as used for the plasma sheet simulation in the main text of this thesis. In order to more effectively measure the numerical error, the scheme is tested on the *linear wave problem*, for which the exact solution is available. The problem itself will be presented later in Appendix E.

The L^1, L^2, and L^∞ errors for the density ρ in the numerical simulation of the fast magnetosonic wave (propagation velocity $c_{\mathrm{fm}} = 2$ over a periodic

domain of size $L_x = 1.0$) are shown in figure A.2. The errors are defined as

$$\mathrm{err}_{L^1} = \Delta x \Delta y \sum_{i,j} |\rho^N_{i,j} - \rho^0_{i,j}|, \tag{A.6}$$

$$\mathrm{err}_{L^2} = \Delta x \Delta y \sqrt{\sum_{i,j} (\rho^N_{i,j} - \rho^0_{i,j})^2}, \tag{A.7}$$

$$\mathrm{err}_{L^\infty} = \max_{i,j} |\rho^N_{i,j} - \rho^0_{i,j}|, \tag{A.8}$$

where $\rho^N_{i,j}$ is the simulation result after $N = 8192$ steps of $\Delta t = t_{\max}/N$ after one period ($t_{\max} = 0.5$), and $\rho^0_{i,j}$ is the initial value at $t_0 = 0$, which coincides with the exact solution at $t_{\max} = 0.5$. By comparing the errors with lines of slopes N_x^{-1} and N_x^{-2}, we can see that the L^∞ error of the ENO-LF scheme used in the MHD simulation is approximately of the first order. However, from the L^1 and L^2 errors, we can see that globally the employed ENO-LF scheme is approximately of the second order, which is satisfactory for the purposes of this thesis.

These results agree with the theory of the ENO schemes, which state that an rth-order accurate ENO scheme may accumulate an $O((\Delta x)^{r-1})$ error around local extremes, becoming $(r-1)$th order accurate in the maximum norm L^∞ [33]. Note that this does not affect the overall stability of the scheme [36].

A.3 Overall order of the RK3 ENO-LF scheme

To obtain the overall accuracy of the simulation scheme, we plot the dependence of error on both spatial and temporal resolutions. Figures A.3(a) and (b) show, respectively, the L^∞ and the L^2 errors of the simulation of the linear wave problem. It is immediately obvious that the primary bottleneck of the scheme's accuracy is the spatial resolution, i.e., the number of grid points. As long as the CFL condition is satisfied, reducing the time step offers no further improvements to the accuracy.

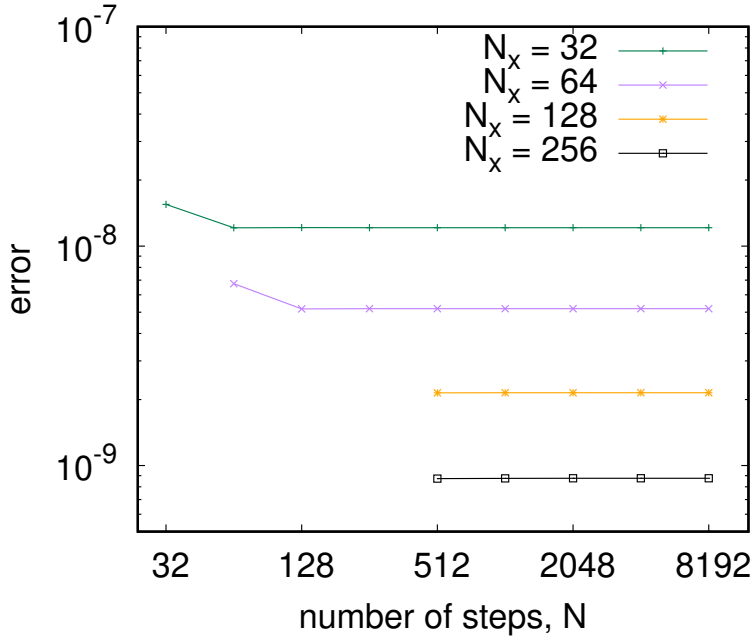

(a) L^∞ error

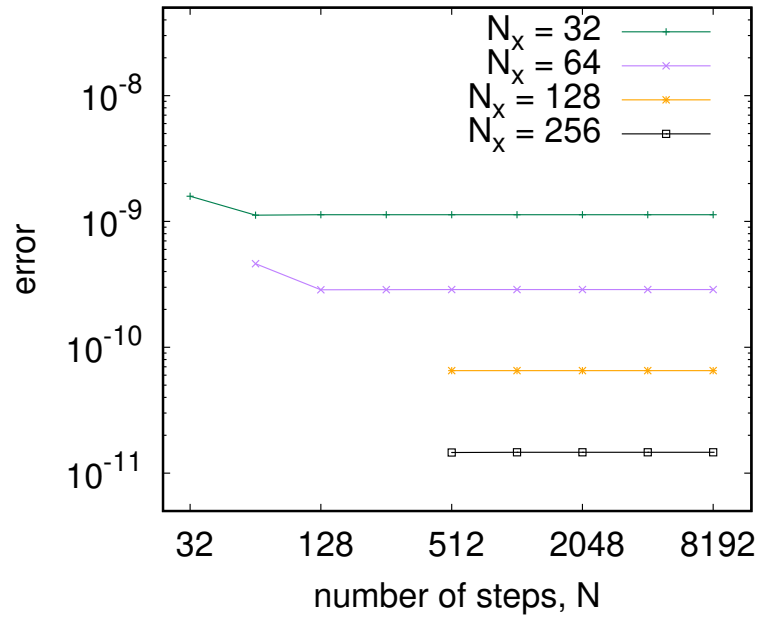

(b) L^2 error

Figure A.3: Errors for the combined ENO-LF scheme with RK3 time stepping, with total number of time steps N on the horizontal axis and error on the vertical axis. Different number of grid points N_x is shown on a different line.

Appendix B

Standard numerical tests

In order to determine whether the simulation program described in Chapter 3 can appropriately deal with the MHD problems that include shocks, in addition to the linear wave problem used for determining the scheme's order (see Appendix A), the code is used to simulate a couple of standard test problems.

The first test is the 1D *Brio & Wu shock tube* problem [32], which shows whether the code can accurately reproduce MHD shocks and rarefactions. (Note that the 1D problem can be run as a 2D simulation by making the medium uniform in the direction perpendicular to the disturbance.) The second test is the *Orszag-Tang vortex* problem [50], which shows how the code handles shock-shock interactions and the MHD turbulence.

We have found the paper and website of the *Athena* astrophysical MHD code to contain a good summary of the various tests for the MHD codes in general. The paper by Stone *et al.* [51] includes a wide range of test problems (including the reasoning behind them) and their solutions. In addition to the black and white plots in the paper, the full-color plots and animation available, at the time of writing of this thesis, at `https://www.astro.princeton.edu/~jstone/Athena/tests/`, were very helpful for testing the simulation code.

B.1 Brio & Wu shock tube

A shock tube is a Riemann problem [29], with two distinct initial states $\mathbf{U}_{\mathrm{L}}$ and $\mathbf{U}_{\mathrm{R}}$ separated by a diaphragm. At time $t = 0$ the diaphragm is removed and the states begin to interact. In hydrodynamics, commonly used initial conditions are those from the *Sod's shock tube* problem [52]; the *Brio & Wu shock tube* [32] is an extension of Sod's shock tube to MHD.

The initial states in Brio & Wu shock tube are

$$\begin{bmatrix} \rho_{\mathrm{L}} \\ u_{\mathrm{L}} \\ v_{\mathrm{L}} \\ w_{\mathrm{L}} \\ B_{x,\mathrm{L}} \\ B_{y,\mathrm{L}} \\ B_{z,\mathrm{L}} \\ p_{\mathrm{L}} \end{bmatrix} = \begin{bmatrix} 1 \\ 0 \\ 0 \\ 0 \\ 0.75 \\ 1 \\ 0 \\ 1 \end{bmatrix}, \quad \begin{bmatrix} \rho_{\mathrm{R}} \\ u_{\mathrm{R}} \\ v_{\mathrm{R}} \\ w_{\mathrm{R}} \\ B_{x,\mathrm{R}} \\ B_{y,\mathrm{R}} \\ B_{z,\mathrm{R}} \\ p_{\mathrm{R}} \end{bmatrix} = \begin{bmatrix} 0.125 \\ 0 \\ 0 \\ 0 \\ 0.75 \\ -1 \\ 0 \\ 0.1 \end{bmatrix}, \tag{B.1}$$

with ratio of specific heats $\gamma = 2$.

Figure B.1 shows the test results at time $t = 0.25$ calculated with grid densities of 16, 32, and 64 points per unit length, in a simulation box of $(L_x, L_y) = (2, 0.5)$, for a total grid size of, respectively, 32×8, 64×16, and 128×32. Black solid line is an approximation for the correct solution, calculated with grid density of 512 points per unit length, in a simulation box of $(L_x, L_y) = (2, 0.015625)$, for a total grid size of 1024×8.

It is clear that the shocks and transitions are smeared out over four or five grid points; however, the overall structure of the solution—size and position of shocks and rarefactions—is captured fairly well even at very low grid densities. For the purposes of this thesis a small amount of smearing is acceptable, as we are mainly interested in large-scale behavior.

B.2 Orszag-Tang vortex

The Orszag-Tang (OT) vortex [50] was designed to explore the evolution of MHD turbulence, in order to compare it with the evolution of hydrodynamic

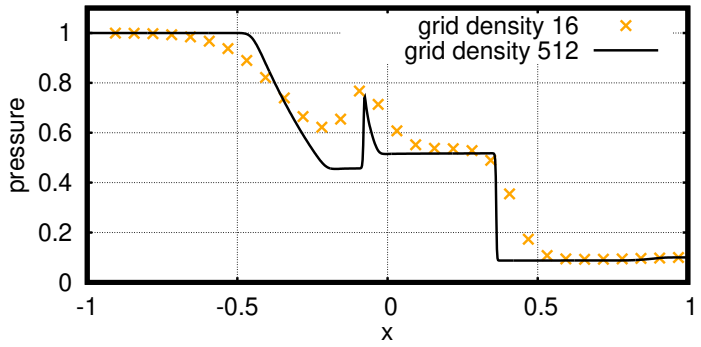

(a) 16 points per unit length

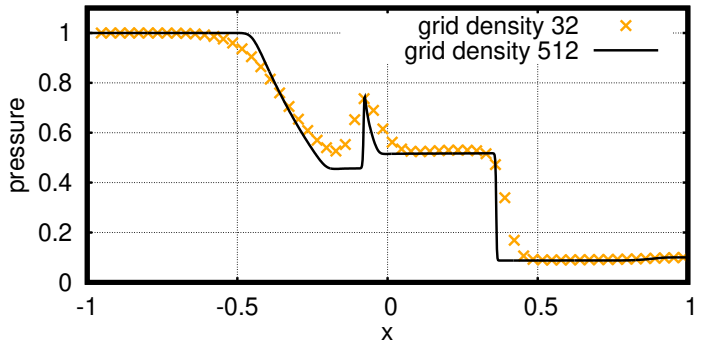

(b) 32 points per unit length

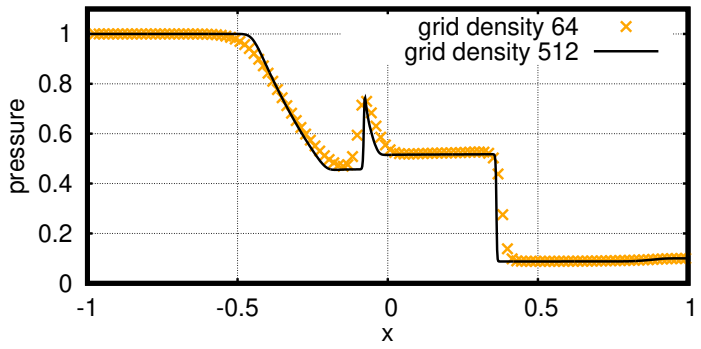

(c) 64 points per unit length

Figure B.1: Pressure plots for the Brio & Wu shock tube problem at time $t = 0.25$. Black solid line is the high-precision result, calculated at 512 grid points per unit length (1024 points total), while orange crosses show the results for the grid densities used in the main plasma sheet simulation in this thesis (16, 32, and 64 grid points per unit length).

turbulence. It has since been used as one of the standard problems for testing 2D MHD simulation code.

The initial conditions for the OT vortex used in this thesis are

$$\begin{aligned} \rho &= \gamma^2, & p &= \gamma, \\ u &= -\sin(y), & v &= \sin(x), & w &= 0, \\ B_x &= -\sin(y), & B_y &= \sin(2x), & B_z &= 0, \end{aligned} \tag{B.2}$$

with the ratio of specific heats $\gamma = 5/3$, and a periodic area of size $(L_x, L_y) = (2\pi, 2\pi)$.

The results for pressure at times $t = 1, 3$ and 10 are shown, respectively, in figures B.2, B.3, and B.4. Each figure shows four results arranged in a 2×2 pattern for easier comparison, with total number of grid points $(N_x, N_y) = (64, 64)$ (top left), $(128, 128)$ (top right), $(256, 256)$ (bottom left), and $(512, 512)$ (bottom right). In figure B.2 the shock fronts have developed, and started moving towards each other. Figure B.3 shows the time shortly after the shock fronts collided in the center of the simulation area. We can see that the interactions of shocks is faithfully captured at all grid sizes, albeit with less detail for coarser grids. The overall structure is preserved even at 64 grid points. Finally, figure B.4 depicts the plasma after the turbulence has had some time to develop. We can see that, while the overall structure is still similar, the results for different number of grid points have started to diverge. Nevertheless, the convergence as the number of grid points is increased is still clear, showing that the simulation code is fairly robust against complicated interaction of MHD shocks and waves.

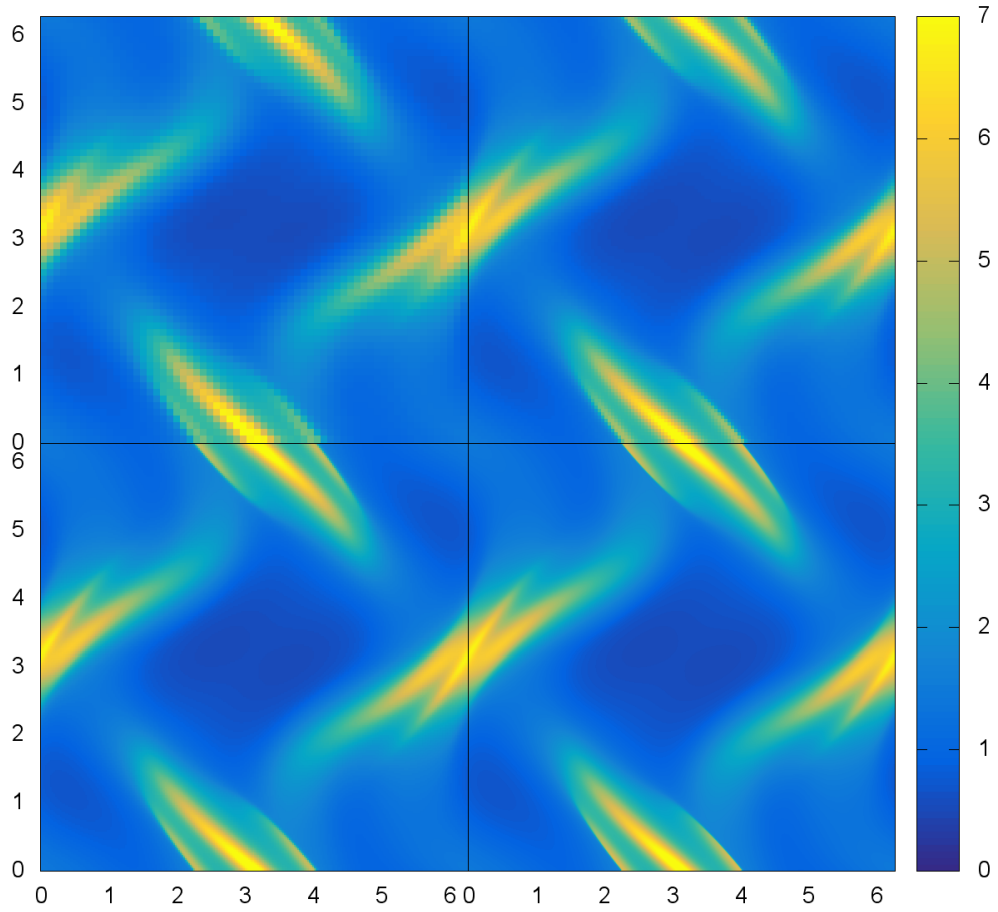

Figure B.2: Pressure plots for the Orszag-Tang vortex problem at time $t = 1$. The entire simulation area is shown four times, once for each number of grid points. Top left: 64×64 grid points; top right: 128×128 grid points; bottom left: 256×256 grid points; bottom right: 512×512 grid points.

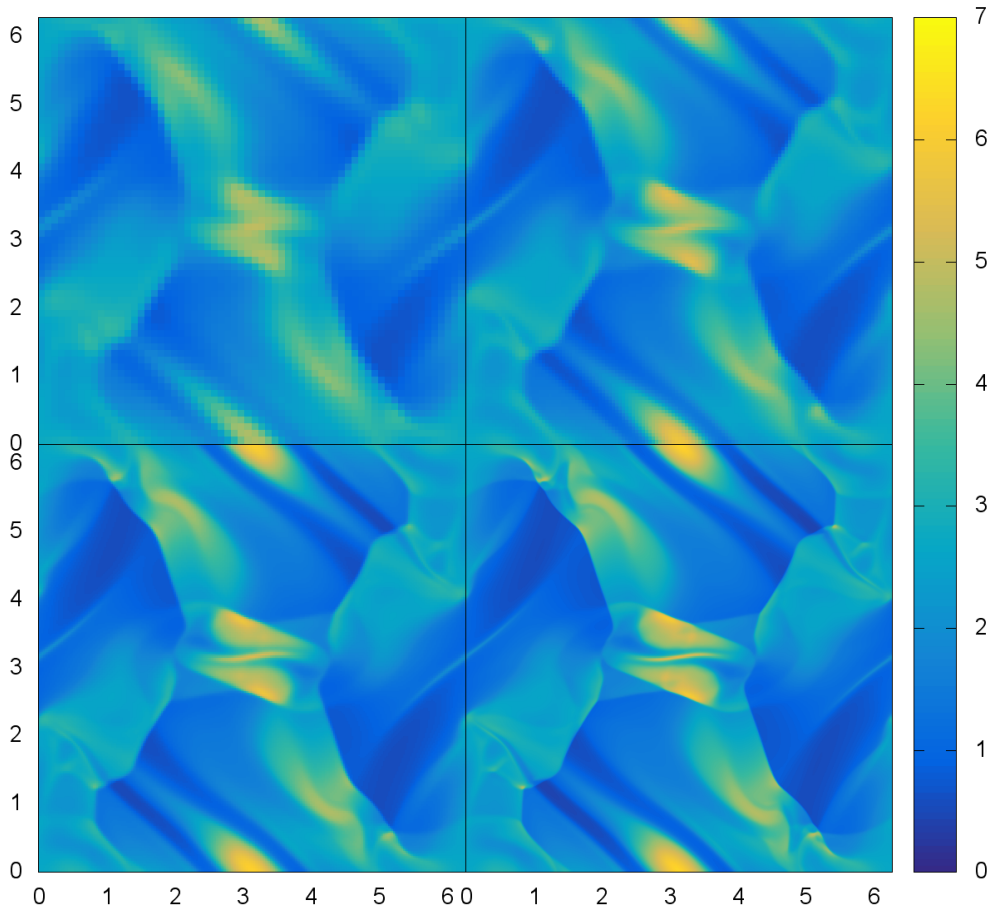

Figure B.3: Pressure plots for the Orszag-Tang vortex problem at time $t = 3$. Structure of the plot is the same as in figure B.2.

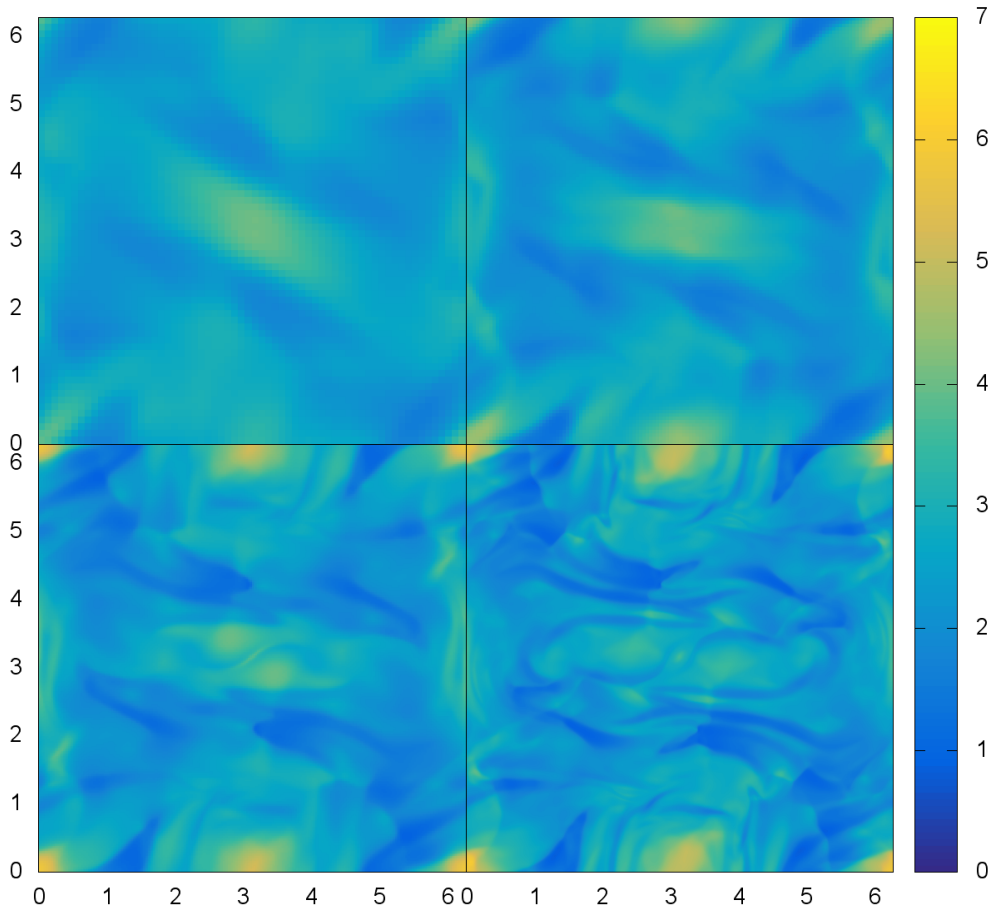

Figure B.4: Pressure plots for the Orszag-Tang vortex problem at time $t = 10$. Structure of the plot is the same as in figure B.2.

Appendix C

Size of the simulation domain

Results of the 2D plasma sheet problem shown in Chapter 5 were simulated on a domain size of $L_x = 32$ and $L_y = 6$. The domain size in the x direction was chosen to be large enough that, even if the boundary effect was significant, waves do not have time to reach the boundary, reflect, and return to the observed area. The primary reason L_x had to be large is that we need the left and right sides of the domain to be static; if there is a significant deviation from the initial conditions at the left or right boundaries, the Dirichlet boundary conditions that were imposed would no longer be valid, and a non-physical disturbance may start propagating through the domain.

On the other hand, the top and bottom boundaries are under the Neumann boundary conditions, so the values of $\mathbf{U}$ are not forced. Furthermore, due to some useful properties of the ENO method [36], coupled with the waves in the plasma sheet (and on the sheet-lobe boundary) being significantly stronger than the waves propagating through the lobes, the nonphysical reflections of waves from the boundary are small enough to have no significant effect on the results. Therefore, the domain size in the y direction can be kept significantly lower, which is certainly helpful to simulation running times.

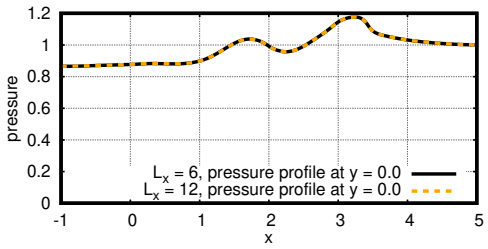

(a) pressure profile at $t = 2.5$

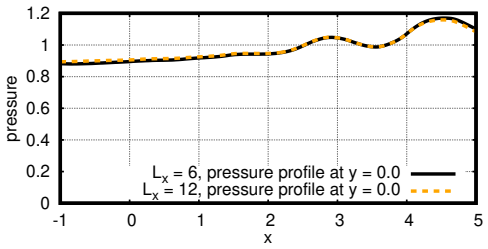

(b) pressure profile at $t = 4.0$

Figure C.1: Horizontal profiles of pressure evolution for run E1 ($\tau = 2.0$, $\beta_{\text{lobe}} = 0.2$, $u_{\text{init}} = -1.0$) of the 2D plasma simulation with a resolution of 32 grid points per unit length. Black solid line is the pressure profile taken through $y = 0$, calculated with domain size $(L_x, L_y) = (32, 6)$, while the orange dashed line is the same with double-height domain size, $(L_x, L_y) = (32, 12)$. (a) shows the pressure profiles at time $t = 2.5$, with the two profiles being perfectly matched. (b) shows the pressure profiles at time $t = 4.0$, where they have started to slightly diverge.

C.1 Domain size in the y direction

To confirm that the effects of the Neumann boundary conditions at the top and bottom boundaries are not significant, we run several simulations with doubled size in the y direction, $L_y = 12$.

Figure C.1 shows the time evolution of pressure, with black solid line and orange dashed line depicting, respectively, the pressure profiles for $L_y = 6$ and $L_y = 12$. In figure C.1(a), the two plots are identical, indicating that either there is no influence from the boundary, or that the disturbance did not yet have time to reach the boundary, reflect, and travel back to the sheet. However, in figure C.1(b), we can observe a slight discrepancy between two domain sizes at $x < 1$ and $x > 4$. This indicates that there is at least *some* reflection from the boundary.

Figure C.2 shows the pressure profiles at $t = 10$, when the reflections from the boundary have had more time to fully propagate throughout the domain. Black solid line and orange dashed line again depict, respectively, the pressure profiles for $L_y = 6$ and $L_y = 12$. Here, it can be seen that the change in the

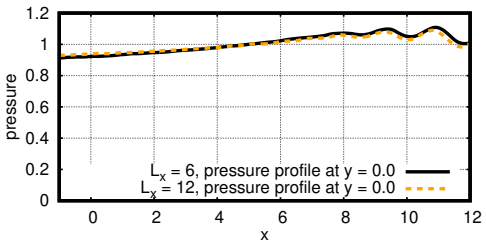

(a) pressure profile at $t = 10$, $y = 0$

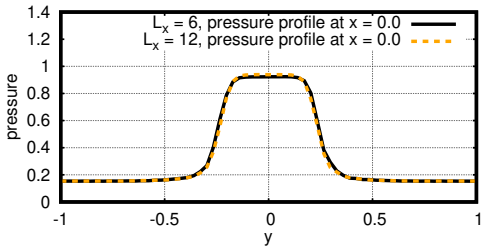

(b) pressure profile at $t = 10$, $x = 0$

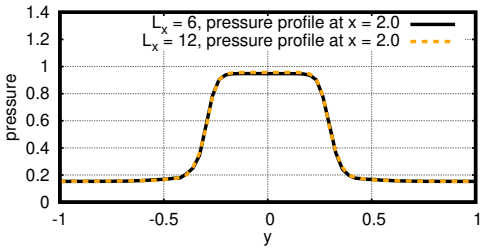

(c) pressure profile at $t = 10$, $x = 2$

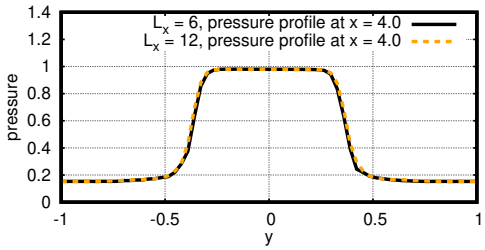

(d) pressure profile at $t = 10$, $x = 4$

Figure C.2: Horizontal and vertical profiles of pressure at $t = 10$ for run E1 ($\tau = 2.0$, $\beta_{\text{lobe}} = 0.2$, $u_{\text{init}} = -1.0$) of the 2D plasma simulation with a resolution of 32 grid points per unit length. Black solid line is the pressure profile for domain size $(L_x, L_y) = (32, 6)$, while the orange dashed line is the same for domain size $(L_x, L_y) = (32, 12)$. (a) shows the horizontal pressure profile through $y = 0$ (note that the scale of the x axis is larger than in figure C.1). (b)–(d) show the vertical pressure profiles through $x = 0, 2, 4$; sheet shapes are visibly different, but not drastically so.

shape of the plasma sheet is still fairly limited. In figure C.2(a) we can see from the horizontal profile through the center of the plasma sheet ($y = 0$) that the overall shape of the inner plasma sheet, including the wave train, is kept to a reasonable degree. Figures C.2(b)–(d) show the vertical profiles at $x = 0, 2, 4$ at the same point in time. We can see that the change in sheet width is barely noticeable.

C.2 Domain size in the x direction

Lowering the domain size in the x (horizontal) direction can introduce a dramatic inconsistency between the state of the plasma in the simulation area and the state as defined by the Dirichlet boundary conditions applied on the left and right edges.

As the simulation results in 2D show (see, e.g., figure 5.4), in the current configuration the plasma sheet thinning propagates both tailward and Earthward. On the other hand, the Dirichlet boundary conditions, defined in equations (5.6) and (5.7), assume that the width of the plasma sheet at the respective boundaries is approximately constant and equal to the initial value. If the thinning reaches the Dirichlet boundary, the assumption of constant width no longer holds. When the discrepancy becomes too large, the simulation breaks down, no longer able to proceed.

Preliminary testing has shown that for the initial disturbance velocity $u_0 = -1$, at time $t = 10$ the thinning front is located at approximately $x = -16$, with the wave train of pulses preceding the train. The left half of the domain for the simulation with a domain width of $L_x = 32$ is shown in figure C.3, with the initial width of the plasma sheet marked with a red line. The shape of the left-moving thinning front can be seen in figure C.3(a), with the wave train preceding the thinning itself. Around $t = 8$, the front of the wave train reaches the left boundary at $x = -16$ (figure C.3(b)). Finally, the thinning itself hits the boundary around $t = 10$ (figure C.3(c)), which is consistent with the measured thinning velocity (see figure 5.7).

It is clear from the plots that there is no noticeable disturbance reflecting

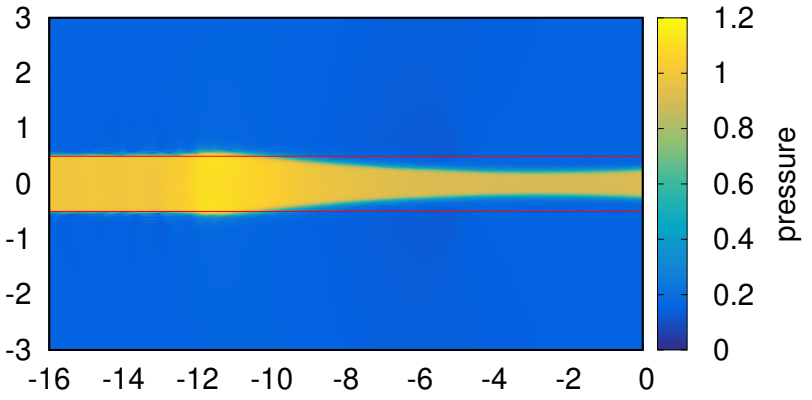

(a) pressure at $t = 6$

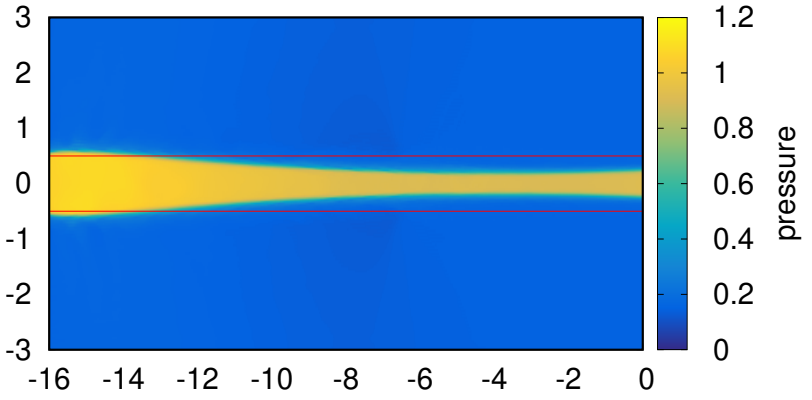

(b) pressure at $t = 8$

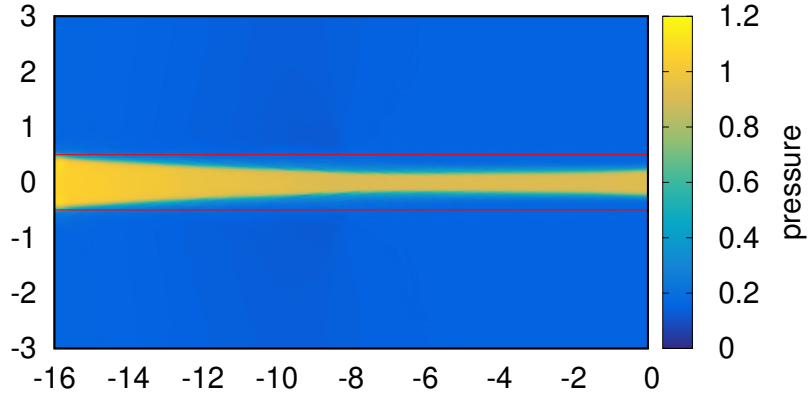

(c) pressure at $t = 10$

Figure C.3: Pressure in the left half of the simulation domain for run E1 ($\tau = 2.0$, $\beta_{\text{lobe}} = 0.2$, $u_{\text{init}} = -1.0$) of the 2D plasma simulation with a resolution of 32 grid points per unit length, with the domain size of $(L_x, L_y) = (32, 6)$. The red lines indicate the initial location of the sheet–lobe boundary. (a) shows the sheet at time $t = 6$, (b) at time $t = 8$, and (c) at time $t = 10$.

from the boundary before the thinning front reaches it. Continuing the simulation for $t > 10$ results in negative pressure and the simulation breaking down in fairly short order.

C.3 Dependence of thinning velocity on domain size

Test simulations for run E1, at grid density of 16 points per unit length, were run for different domain sizes to check the convergence. The results are shown in figure C.4.

From figure C.4(a), it is clear that—once the domain size is large enough for the simulation not to break down—the measured thinning velocity does shows a slight fluctuation, but it is less than one percent. This suggests that any disturbances resulting from the reflection from Dirichlet boundary on the left and right edges are small enough, and/or slow enough, not to influence results.

Figure C.4(b), on the other hand, shows that, at such low heights, the effects of the Neumann boundary are still fairly strong. However, the thinning velocity also displays a clear convergence, and for $L_y \geq 6$ the results are sufficiently stable for the purposes of this thesis. For a larger grid density of 32 points per unit length, this allows us to cut the simulation runtime from ~ 8.3 h for a domain size $(L_x, L_y) = (32, 12)$ to ~ 3.4 h for $(L_x, L_y) = (32, 6)$. Notably, the computational cost would be prohibitive for the largest grid density usid in this thesis, 64 points per unit length, as even with the reduced domain size it took ~ 56 h for a single simulation run.

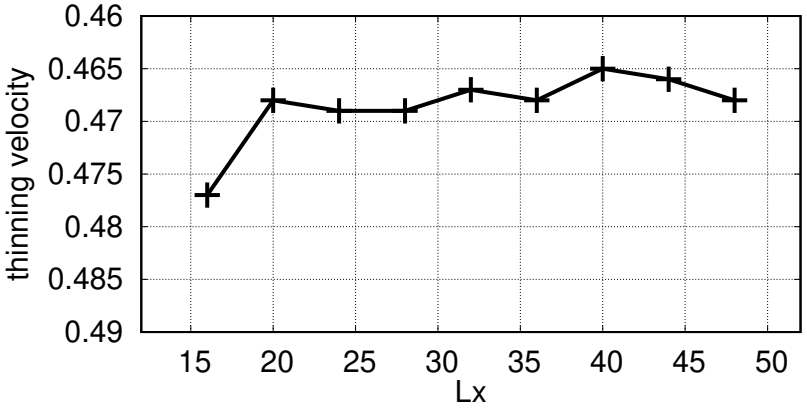

(a) dependence on L_x

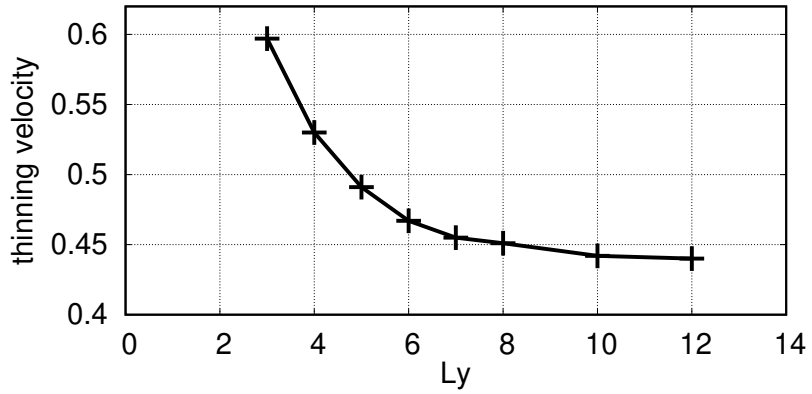

(b) dependence on L_y

Figure C.4: Thinning velocities for run E1 ($\tau = 2.0$, $\beta_{\text{lobe}} = 0.2$, $u_{\text{init}} = -1.0$) of the 2D plasma simulation with a resolution of 16 grid points per unit length, measured with various domain sizes. (a) shows the dependence on L_x, with height fixed to $L_y = 6$. (b) shows the dependence on L_y, with width fixed to $L_x = 32$.

Appendix D

Analysis of Kelvin-Helmholtz instability

In the 2D simulation of the plasma sheet, the interface between sheet and lobe separates two plasmas with dramatically different densities, with one of them (lobe) being stationary and the other (left half of the sheet) being assigned a high velocity, on the order of sound speed, in the parallel direction. The described situation is conductive to the development of the Kelvin-Helmholtz (KH) instability. On the other hand, it is known that the magnetic field has a stabilizing influence, preventing the development of the KH instability. In this chapter, we explore whether the KH instability forms, and if it does, what influence it has on the result.

D.1 Condition for instability

This analysis follows that of Chandrasekhar for homogeneous field [47]. For simplicity, we analyze the 2D dynamics in (x, y) plane under incompressible

MHD equations,

$$\frac{\partial \rho}{\partial t} + \boldsymbol{\nabla} \cdot (\rho \mathbf{u}) = 0, \tag{D.1}$$

$$\rho \left(\frac{\partial \mathbf{u}}{\partial t} + \mathbf{u} \cdot \boldsymbol{\nabla} \mathbf{u} \right) = -\boldsymbol{\nabla} \left(p + \frac{B^2}{2\mu_0} \right) + \frac{1}{\mu_0} \mathbf{B} \cdot \boldsymbol{\nabla} \mathbf{B}, \tag{D.2}$$

$$\frac{\partial \mathbf{B}}{\partial t} + \mathbf{u} \cdot \boldsymbol{\nabla} \mathbf{B} - \mathbf{B} \cdot \boldsymbol{\nabla} \mathbf{u} = \mathbf{0}, \tag{D.3}$$

$$\boldsymbol{\nabla} \cdot \mathbf{u} = 0. \tag{D.4}$$

We assumed incompressible plasma, since compressibility may not play an essential role for the KH instability.

We set up a stratified equilibrium, $\mathbf{u}_{\rm eq} = (u_{\rm eq}, 0)$, $\mathbf{B}_{\rm eq} = (B_{\rm eq}, 0)$, and

$$\rho_{\rm eq} = \begin{cases} \rho_1 \\ \rho_2 \end{cases} \quad u_{\rm eq} = \begin{cases} 0 \\ u_2 \end{cases} \quad p_{\rm eq} = \begin{cases} p_1 \\ p_2 \end{cases} \quad B_{\rm eq} = \begin{cases} B_1 & (y > 0) \\ 0 & (y < 0) \end{cases}, \tag{D.5}$$

where each quantity is homogeneous at each region separated by $y = 0$. To meet the stationary condition of the MHD equations, it must hold that

$$p_1 + \frac{B_1^2}{2\mu_0} = p_2. \tag{D.6}$$

We split all the quantities, represented here by ξ, into equilibrium ($\xi_{\rm eq}$) and perturbed ($\tilde{\xi}$) parts,

$$\xi(x, y, t) = \xi_{\rm eq}(y) + \tilde{\xi}(x, y, t), \tag{D.7}$$

where

$$\tilde{\xi}(x, y, t) = \hat{\xi}(y) \exp[i(kx - \omega t)]. \tag{D.8}$$

Equations (D.1)–(D.4) are then linearized to obtain

$$-\mathrm{i}(\omega - ku_{\mathrm{eq}})\tilde{\rho} + \frac{\mathrm{d}\rho_{\mathrm{eq}}}{\mathrm{d}y}\tilde{v} = 0, \tag{D.9}$$

$$-\mathrm{i}\rho_{\mathrm{eq}}(\omega - ku_{\mathrm{eq}})\tilde{u} + \rho_{\mathrm{eq}}\frac{\mathrm{d}u_{\mathrm{eq}}}{\mathrm{d}y}\tilde{v} = -\mathrm{i}k\tilde{p} + \frac{1}{\mu_0}\frac{\mathrm{d}B_{\mathrm{eq}}}{\mathrm{d}y}\tilde{B}_y, \tag{D.10}$$

$$-\mathrm{i}\rho_{\mathrm{eq}}(\omega - ku_{\mathrm{eq}})\tilde{v} = -\frac{\partial\tilde{p}}{\partial y} - \frac{1}{\mu_0}\left(\frac{\partial B_{\mathrm{eq}}\tilde{B}_x}{\partial y} - \mathrm{i}kB_{\mathrm{eq}}\tilde{B}_y\right), \tag{D.11}$$

$$-\mathrm{i}(\omega - ku_{\mathrm{eq}})\tilde{B}_x + \frac{\mathrm{d}B_{\mathrm{eq}}}{\mathrm{d}y}\tilde{v} - \mathrm{i}kB_{\mathrm{eq}}\tilde{u} - \frac{\mathrm{d}u_{\mathrm{eq}}}{\mathrm{d}y}\tilde{B}_y = 0, \tag{D.12}$$

$$-\mathrm{i}(\omega - ku_{\mathrm{eq}})\tilde{B}_y - \mathrm{i}kB_{\mathrm{eq}}\tilde{v} = 0, \tag{D.13}$$

$$\mathrm{i}k\tilde{u} + \frac{\partial\tilde{v}}{\partial y} = 0, \tag{D.14}$$

where we used the linearization

$$\widetilde{\mathbf{u}\cdot\boldsymbol{\nabla}\mathbf{u}} = \left(\mathrm{i}ku_{\mathrm{eq}}\tilde{u} + \frac{\mathrm{d}u_{\mathrm{eq}}}{\mathrm{d}y}\tilde{v}\right)\mathbf{e}_x + \mathrm{i}ku_{\mathrm{eq}}\tilde{v}\mathbf{e}_y, \tag{D.15}$$

$$\widetilde{\mathbf{u}\cdot\boldsymbol{\nabla}\mathbf{B}} = \left(\mathrm{i}ku_{\mathrm{eq}}\tilde{B}_x + \frac{\mathrm{d}B_{\mathrm{eq}}}{\mathrm{d}y}\tilde{v}\right)\mathbf{e}_x + \mathrm{i}ku_{\mathrm{eq}}\tilde{B}_y\mathbf{e}_y, \tag{D.16}$$

$$\widetilde{\boldsymbol{\nabla}\left(\frac{1}{2}B^2\right)} = \mathrm{i}kB_{\mathrm{eq}}\tilde{B}_x\mathbf{e}_x + \frac{\partial B_{\mathrm{eq}}\tilde{B}_x}{\partial y}\mathbf{e}_y, \tag{D.17}$$

where $\mathbf{e}_x$ and $\mathbf{e}_y$ are, respectively, the unit vectors in the x and y directions. Note that, since u_{eq} and B_{eq} are discontinuous, $\mathrm{d}u_{\mathrm{eq}}/\mathrm{d}y$ and $\mathrm{d}B_{\mathrm{eq}}/\mathrm{d}y$ contain Dirac's delta function $\delta(y)$.

From equations (D.13) and (D.12), we can express the perturbed field components in terms of velocity as

$$\tilde{B}_y = -\frac{kB_{\mathrm{eq}}}{\omega - ku_{\mathrm{eq}}}\tilde{v}, \tag{D.18}$$

$$\tilde{B}_x = -\frac{kB_{\mathrm{eq}}}{\omega - ku_{\mathrm{eq}}}\left(\tilde{u} + \frac{idu_{\mathrm{eq}}/dy}{\omega - ku_{\mathrm{eq}}}\tilde{v}\right) - \frac{\mathrm{i}\mathrm{d}B_{\mathrm{eq}}/\mathrm{d}y}{\omega - ku_{\mathrm{eq}}}\tilde{v}. \tag{D.19}$$

From equation (D.14) we can obtain

$$\tilde{u} = \frac{i}{k}\frac{\partial\tilde{v}}{\partial y}, \tag{D.20}$$

which can be substituted into equations (D.19) and (D.10) to, after some manipulations, obtain

$$\tilde{B}_x = -\frac{\mathrm{i}B_{\mathrm{eq}}}{\omega - ku_{\mathrm{eq}}}\frac{\partial\tilde{v}}{\partial y} - \frac{\mathrm{i}}{\omega - ku_{\mathrm{eq}}}\left(\frac{kB_{\mathrm{eq}}\mathrm{d}u_{\mathrm{eq}}/\mathrm{d}y}{\omega - ku_{\mathrm{eq}}} + \frac{\mathrm{d}B_{\mathrm{eq}}}{\mathrm{d}y}\right)\tilde{v} \tag{D.21}$$

and

$$\tilde{p} = \frac{\mathrm{i}\rho_{\mathrm{eq}}(\omega - ku_{\mathrm{eq}})}{k^2}\frac{\partial \tilde{v}}{\partial y} + \left(\frac{\mathrm{i}\rho_{\mathrm{eq}}}{k}\frac{\mathrm{d}u_{\mathrm{eq}}}{\mathrm{d}y} + \frac{\mathrm{i}B_{\mathrm{eq}}\mathrm{d}B_{\mathrm{eq}}/\mathrm{d}y}{\mu_0(\omega - ku_{\mathrm{eq}})}\right)\tilde{v}. \tag{D.22}$$

Substituting all of these into (D.11) to express it in terms of $\hat{v}$, we obtain

$$\begin{aligned}
&\frac{\mathrm{d}}{\mathrm{d}y}\left[\frac{\rho_{\mathrm{eq}}(\omega - ku_{\mathrm{eq}})}{k^2}\frac{\mathrm{d}\hat{v}}{\mathrm{d}y} + \left(\frac{\rho_{\mathrm{eq}}u'_{\mathrm{eq}}}{k} + \frac{B_{\mathrm{eq}}B'_{\mathrm{eq}}}{\mu_0(\omega - ku_{\mathrm{eq}})}\right)\hat{v}\right] \\
&-\frac{1}{\mu_0}\frac{\mathrm{d}}{\mathrm{d}y}\left[\frac{B_{\mathrm{eq}}^2}{\omega - ku_{\mathrm{eq}}}\frac{\mathrm{d}\hat{v}}{\mathrm{d}y} + \frac{B_{\mathrm{eq}}}{\omega - ku_{\mathrm{eq}}}\left(\frac{kB_{\mathrm{eq}}u'_{\mathrm{eq}}}{\omega - ku_{\mathrm{eq}}} + B'_{\mathrm{eq}}\right)\hat{v}\right] \\
&\qquad + \left(\frac{k^2B_{\mathrm{eq}}^2}{\mu_0(\omega - ku_{\mathrm{eq}})} - \rho_{\mathrm{eq}}(\omega - ku_{\mathrm{eq}})\right)\hat{v} = 0,
\end{aligned} \tag{D.23}$$

where the prime denotes the y-derivative of equilibrium quantities, and the exponential factor in all terms was eliminated.

Because of the continuity of the displacement δy,

$$\frac{\partial \delta y}{\partial t} + \mathbf{u}_{\mathrm{eq}} \cdot \boldsymbol{\nabla}\delta y = \tilde{v}, \tag{D.24}$$

at $y = 0$ the boundary condition is the continuity of $\hat{v}/(\omega - ku_{\mathrm{eq}})$. Additionally, in each of the two homogeneous regions, $y < 0$ or $y > 0$, (D.23) gives

$$\left[(\omega - ku_{\mathrm{eq}})^2 - \frac{k^2B_{\mathrm{eq}}^2}{\mu_0\rho_{\mathrm{eq}}}\right]\left(\frac{\mathrm{d}^2\hat{v}}{\mathrm{d}y^2} - k^2\hat{v}\right) = 0. \tag{D.25}$$

Therefore, the solution which vanishes as $y \to \pm\infty$ and gives continuous δy at $y = 0$ is

$$\hat{v} = \begin{cases} A\omega e^{-ky} \\ A(\omega - ku_2)e^{ky} \end{cases} \quad \frac{\mathrm{d}\hat{v}}{\mathrm{d}y} = \begin{cases} -kA\omega e^{-ky} & (y > 0) \\ kA(\omega - ku_2)e^{ky} & (y < 0) \end{cases}, \tag{D.26}$$

where A is an arbitrary constant which satisfies $A = \lim_{y\to 0}[\hat{v}/(\omega - ku_{\mathrm{eq}})]$. By the infinitesimal integration of (D.23) around $y = 0$, we can obtain the dispersion relation

$$\left[\frac{\rho_{\mathrm{eq}}}{k^2}(\omega - ku_{\mathrm{eq}})\frac{\mathrm{d}\hat{v}}{\mathrm{d}y}\right]_{-\epsilon}^{\epsilon} - \left[\frac{B_{\mathrm{eq}}^2}{\mu_0(\omega - ku_{\mathrm{eq}})}\frac{\mathrm{d}\hat{v}}{\mathrm{d}y}\right]_{-\epsilon}^{\epsilon} = 0, \tag{D.27}$$

which, with the use of (D.26), gives

$$\rho_1\omega^2 + \rho_2(\omega - ku_2)^2 = \frac{k^2B_1^2}{\mu_0}. \tag{D.28}$$

From the discriminant, the condition for instability is

$$u_2^2 > \frac{(\rho_1 + \rho_2)B_1^2}{\mu_0 \rho_1 \rho_2}. \tag{D.29}$$

(Interestingly, the critical flow energy is exactly half of Chandrasekhar's example of the homogeneous magnetic field [47, §106, equation (205)].)

D.2 Instability in the simulation

Applied to the plasma sheet setup described in Chapter 5, the condition (D.29) becomes

$$u_{\text{sheet}}^2 > \frac{(\rho_{\text{lobe}} + \rho_{\text{sheet}})B_{x,\text{lobe}}^2}{\rho_{\text{lobe}}\rho_{\text{sheet}}} \tag{D.30}$$

For the smallest simulated lobe beta ($\beta_{\text{lobe}} = 0.2$), with temperature ratio $\tau = 2$, the parameters are

$$u_{\text{init}} = -1, \qquad \rho_{\text{lobe}} = 0.31, \qquad \rho_{\text{sheet}} = 1, \qquad |B_{x,\text{lobe}}| = 1.3, \tag{D.31}$$

which means that the condition (D.30) is not satisfied in any region of our simulation. However, for a weaker field, the condition (D.30) *may* be satisfied in some regions. For example, for a high beta case with $\beta_{\text{lobe}} = 31$ and $\tau = 2$, the parameters are

$$u_{\text{init}} = -1, \qquad \rho_{\text{lobe}} = 1.9375, \qquad \rho_{\text{sheet}} = 1, \qquad |B_{x,\text{lobe}}| = 0.25, \tag{D.32}$$

and the instability condition (D.30) is satisfied in the left side of the computational domain. It is important to note that the KH instability is expected to occur only in the left half of the domain ($x \lesssim 0$) even in the case of notionally unstable parameters such as (D.32), since the initial condition u_{init} is applied only in the left half of the plasma sheet.

Figure D.1 shows the color plot of density at $t = 10$ in the whole computational domain for (a) low beta case corresponding to (D.31), and (b) high beta case corresponding to (D.32). For the low beta, the lobe–sheet boundary forms smooth curves over the entire domain, confirming that the KH instability did not develop.

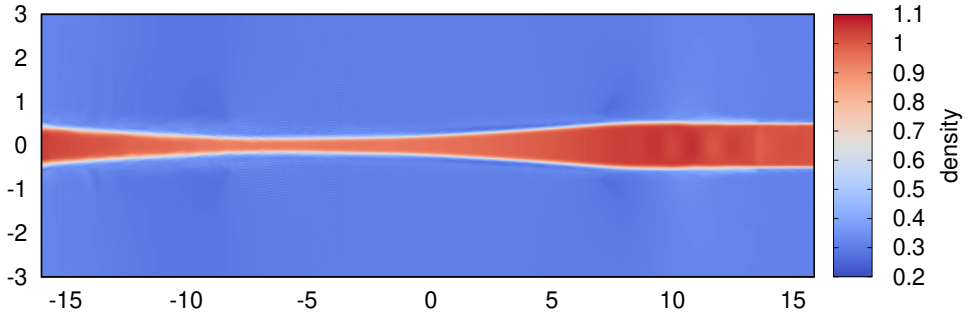

(a) Low beta case, $\beta_{\text{lobe}} = 0.2$.

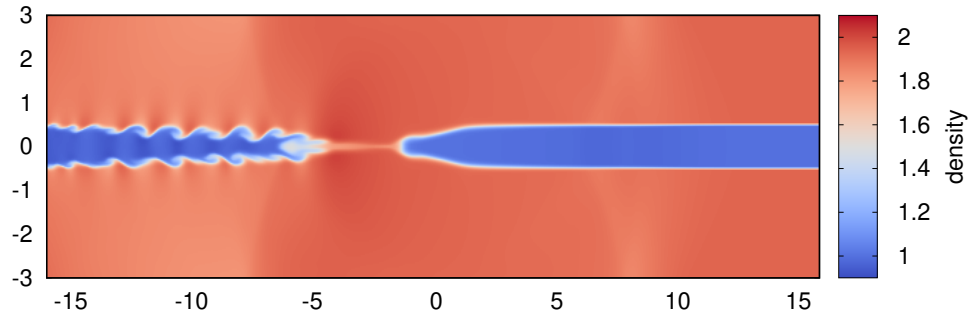

(b) High beta case, $\beta_{\text{lobe}} = 31$.

Figure D.1: Density for temperature ratio $\tau = 2$ at time $t = 10$, with grid density of 32 points per unit length; plots show the entire computational domain.

On the other hand, for the high beta, we see a clear evidence of KH instability at $x \lesssim -5$. However, as can be seen from the lack of the KH instability in the right half of the domain ($x > 0$), even though the initial velocity $u_{\rm init}$ is given at $x < 0$, the plasma velocity at $x \gtrsim 0$ is small enough over the entire simulation period. Since the sheet velocity varies nearly linearly on x in the region $u_{\rm init}t < x < 0$ for $t > 0$, the instability drive becomes weaker as x approaches the origin from the left. Therefore, the KH instability does not influence the right side of the domain ($x > 0$), and is not important for evaluating the plasma sheet thinning.

Appendix E

Comparison of wave decomposition methods

In order to better understand the physics behind certain developments in a plasma simulation, it would be useful if we could see how each individual wave propagates, as well as relative strengths of all waves present. The simulation scheme used for this thesis, described in Chapter 3, offers a possible approach as to how this might be achieved. Specifically, during the spatial integration step described in section 3.1.3, we use the characteristic decomposition to locally separate the constituent equations of the MHD system into a set of independent advection equations, each describing the local propagation of a particular MHD wave.

There are multiple ways to apply the characteristic decomposition on the simulation results with a goal to obtain the wave decomposition. We have evaluated two of these methods. The first one, which we will dub the *characteristic variable method*, will be presented and tested below in section E.2. The second one, dubbed here the *characteristic flux method*, has already been introduced in section 5.6; here we will evaluate it and show the test results in section E.3. The characteristic variable method, while suitable for analysis of a 1D problem, will ultimately be shown as insufficient when applied on a 2D one; the characteristic flux method, which was used to analyze the plasma sheet problem, appears to be adequate in 2D. But first, in order to assess the

suitability of the candidate wave decomposition methods, we require some kind of a test problem.

E.1 Linear wave problem

In a nonlinear problem, such as the plasma sheet problem described in the main body of the thesis, the plasma waves can exhibit complicated interactions and difficult-to-analyze behavior (which is the reason behind this entire exercise). Therefore, to properly evaluate the wave decomposition methods a simpler, easier-to-analyze method is required. We will use the *linear wave problem*, where a small-amplitude disturbance corresponding to a particular chosen wave is added to a uniform background, and propagates at that wave's velocity.

The initial state $\mathbf{U}^{(0)}$ in the 1D MHD linear wave problem, as described by Gardiner and Stone [53], is of the form

$$\mathbf{U}^{(0)} = \bar{\mathbf{U}} + \varepsilon \bar{\mathbf{R}}_l \cos(2\pi x), \tag{E.1}$$

where $\bar{\mathbf{U}}$ is the uniform background, $\bar{\mathbf{R}}_l = \mathbf{R}_l(\bar{\mathbf{U}})$ is the right eigenvector corresponding to the l-th wave mode of the Jacobian matrix of the flux $\mathbf{F}(\bar{\mathbf{U}})$, and ε is the wave amplitude. The uniform background is taken as

$$\begin{aligned} \bar{\rho} &= 1, \\ \bar{p} &= 1/\gamma, \\ (\bar{u}, \bar{v}, \bar{w}) &= (0, 0, 0), \\ (\bar{B}_x, \bar{B}_y, \bar{B}_z) &= (1, \sqrt{2}, 1/2), \end{aligned} \tag{E.2}$$

with the values chosen so that various MHD waves move at different velocities: fast waves at $c_{\mathrm{fm}} = 2$, Alfvén waves at $c_{\mathrm{A}} = 1$, slow waves at $c_{\mathrm{sm}} = 1/2$, and entropy wave at $u = 0$. As the entropy wave does not propagate under these conditions, when testing the entropy component the x component of the velocity is set to $u = 1$. The wave amplitude was set to $\varepsilon = 10^{-7}$, and the length scale has been normalized so that $-0.5 < x < 0.5$, with periodic boundary conditions. The values of $\bar{\mathbf{R}}_l$ for $\bar{\mathbf{U}} = (\bar{\rho}, \bar{\rho}\bar{u}, \bar{\rho}\bar{v}, \bar{\rho}\bar{w}, \bar{B}_x, \bar{B}_y, \bar{B}_z, \bar{e})^\intercal$

from Gardiner & Stone [53], reproduced here for posterity, are

$$\bar{\mathbf{R}}_{1,7} = \frac{1}{6\sqrt{5}}(6, \pm 12, \mp 4\sqrt{2}, \mp 2, 0, 8\sqrt{2}, 4, 27)^\intercal, \tag{E.3}$$

$$\bar{\mathbf{R}}_{2,6} = \frac{1}{3}(0, 0, \pm 1, \mp 2\sqrt{2}, 0, -1, 2\sqrt{2}, 0)^\intercal, \tag{E.4}$$

$$\bar{\mathbf{R}}_{3,5} = \frac{1}{6\sqrt{5}}(12, \pm 6, \pm 8\sqrt{2}, \pm 4, 0, -4\sqrt{2}, -2, 9)^\intercal, \tag{E.5}$$

$$\bar{\mathbf{R}}_{4} = \frac{1}{6\sqrt{5}}(2, 2, 0, 0, 0, 0, 0, 1)^\intercal, \tag{E.6}$$

with indices $l = 1, \ldots, 7$ being assigned to waves in non-increasing order of wave velocities (see equation (2.50)). The right eigenvector for the degenerate wave $\mathbf{R}_8$ is set to zero.

The initial conditions of the 1D linear wave problem can be applied as-is to a 2D grid, with uniform plasma in the y direction, $\mathbf{U}^{(0)}(x, y) = \mathbf{U}^{(0)}(x)$; we also take $-0.5 < y < 0.5$ with periodic boundaries. By simulating the 1D problem on a 2D grid, we can obtain the wave decomposition in x and y directions; as the waves are moving strictly in the x direction, a correct decomposition should recover the dominant component in the x direction and no waves in the y direction.

E.2 Characteristic variable method

This decomposition method is directly based on the properties of the linear wave problem introduced above. We assume that the uniform background $\bar{\mathbf{U}}$ is excited with a linear combination of small-amplitude disturbances $\varepsilon_l \bar{\mathbf{R}}_l \cos(2\pi x)$,

$$\mathbf{U}^{(0)}(x) = \bar{\mathbf{U}} + \sum_l \varepsilon_l \bar{\mathbf{R}}_l \cos(2\pi x), \tag{E.7}$$

where $\bar{\mathbf{R}}_l$, $(l = 1, \ldots, 8)$ are the right eigenvectors of the Jacobian matrix of the flux $\mathbf{F}(\bar{\mathbf{U}})$ corresponding to the wave modes l, and ε_l are their respective amplitudes. After some simple manipulation, we can express the wave decomposition $\mathbf{q}^{(0)}(x)$ as

$$\mathbf{q}^{(0)}(x) = \bar{L}(\mathbf{U}^{(0)}(x) - \bar{\mathbf{U}}), \tag{E.8}$$

where $\bar{L}$ is the matrix whose rows are the left eigenvectors of the Jacobian of the flux $\mathbf{F}(\bar{\mathbf{U}})$. Substituting $\mathbf{U}^{(0)}$, we obtain

$$\mathbf{q}^{(0)}(x) = \sum_l \varepsilon_l \bar{L}\bar{\mathbf{R}}_l \cos x = (\varepsilon_1, \varepsilon_2, \ldots, \varepsilon_k)^\intercal \cos(2\pi x), \tag{E.9}$$

and it becomes clear that $\mathbf{q}^{(0)}(x)$ gives us the relative strengths of the component waves of the disturbance at every point x.

However, the plasma sheet simulation that we ultimately want to analyze is a *not* a linear problem, and we do not have a uniform background state we could use to calculate the exact decomposition of the disturbance. We can approximate the result, however, by using the state at times t_1 and t_2, with $t_1 < t_2$, treating $\mathbf{U}^{(1)}(x) = \mathbf{U}(x, t_1)$ as a background state and $\mathbf{U}^{(2)}(x) = \mathbf{U}(x, t_2)$ as the disturbed state. By analogy to the linear waves, we define the wave decomposition $\mathbf{Q}^{(2)}(x)$ as

$$\mathbf{Q}^{(2)}(x) = L^{(1)}(x)(\mathbf{U}^{(2)}(x) - \mathbf{U}^{(1)}(x)), \tag{E.10}$$

where $L^{(1)}(x)$ is the matrix whose rows are the left eigenvectors of the Jacobian of the flux $\mathbf{F}(\mathbf{U}^{(1)})$. If we let $\Delta t = t_2 - t_1$ go to zero, $\mathbf{Q}^{(2)}(x)$ in equation (E.10) becomes proportional to the first time derivative of the linear wave decomposition $\mathbf{q}^{(2)} = \bar{L}(\mathbf{U}^{(2)}(x) - \bar{\mathbf{U}})$ at time t_2. We should be able to use the absolute values of the decomposition, $|Q_l^{(2)}|$, where $\mathbf{Q^{(2)}} = (Q_1^{(2)}, Q_2^{(2)}, \ldots, Q_k^{(2)})^\intercal$, to estimate the relative wave strengths, and therefore the dominant wave components in an MHD system.

Extending the method to 2D, with $\mathbf{U} = \mathbf{U}(x, y)$, we can rewrite the wave component decomposition (E.10) as

$$\mathbf{Q}_x^{(2)}(x, y) = L_x^{(1)}(x, y)(\mathbf{U}^{(2)}(x, y) - \mathbf{U}^{(1)}(x, y)), \tag{E.11}$$

$$\mathbf{Q}_y^{(2)}(x, y) = L_y^{(1)}(x, y)(\mathbf{U}^{(2)}(x, y) - \mathbf{U}^{(1)}(x, y)), \tag{E.12}$$

where $L_x^{(1)}(x, y)$ is a matrix of left eigenvectors of the Jacobian of the x direction flux $\mathbf{F}(\mathbf{U}^{(1)})$, where $L_y^{(1)}(x, y)$ is a matrix of left eigenvectors of the Jacobian of the y direction flux $\mathbf{G}(\mathbf{U}^{(1)})$, and $\mathbf{Q}_x^{(2)}(x, y)$ and $\mathbf{Q}_y^{(2)}(x, y)$ are the wave decompositions in, respectively, x and y directions.

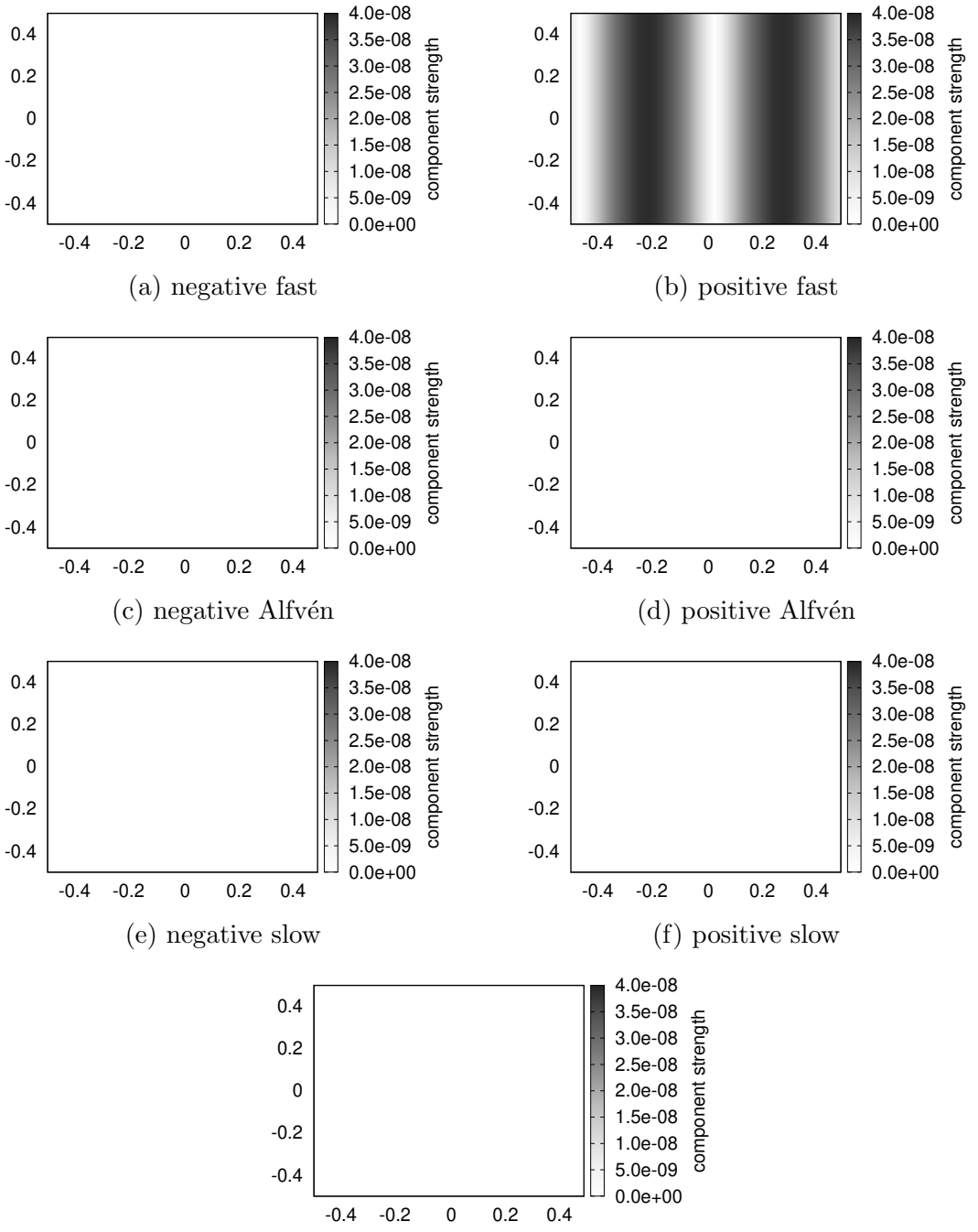

(a) negative fast

(b) positive fast

(c) negative Alfvén

(d) positive Alfvén

(e) negative slow

(f) positive slow

(g) entropy

Figure E.1: Strength $|Q^{(2)}_{x,l}(x,y)|$ of the x direction wave components for a linear wave problem initialized with the right-moving (i.e., positive) fast magnetosonic wave. As expected, the positive fast magnetosonic component is dominant; other six components are on the order of numerical error.

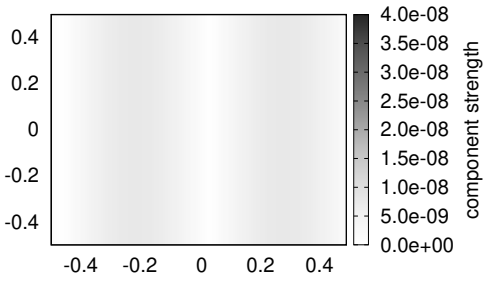

(a) negative fast

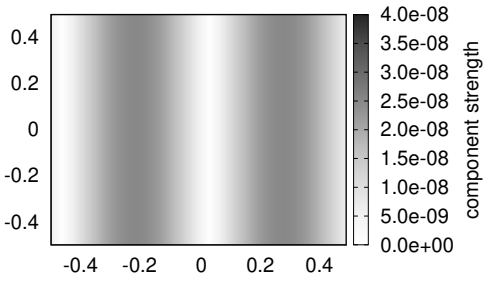

(b) positive fast

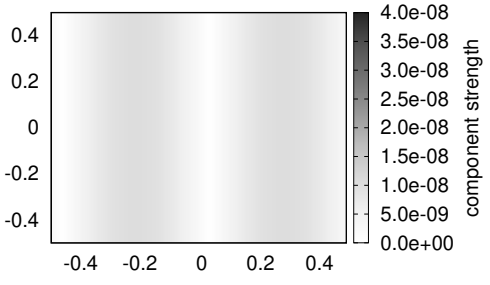

(c) negative Alfvén

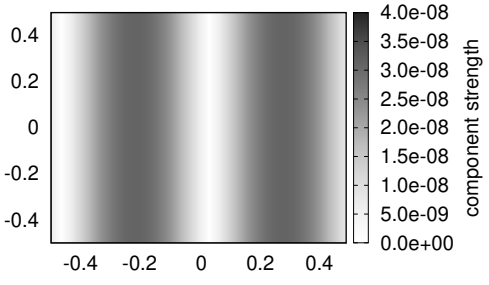

(d) positive Alfvén

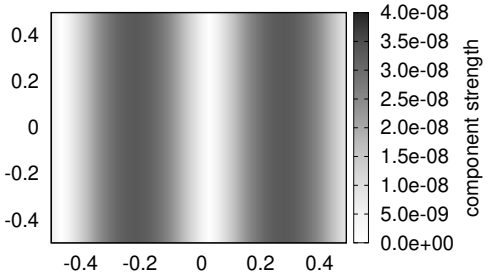

(e) negative slow

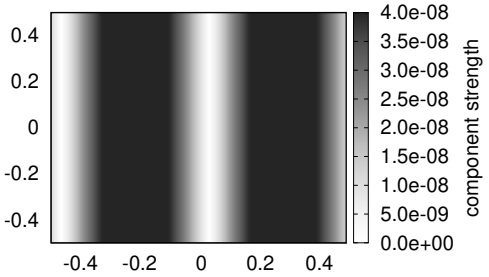

(f) positive slow

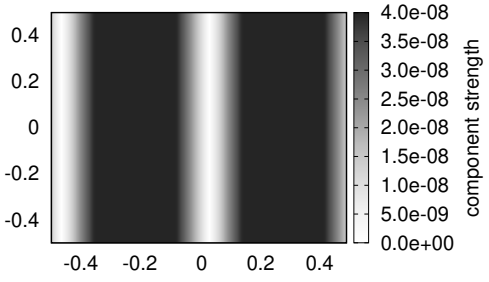

(g) entropy

Figure E.2: Strength $|Q^{(2)}_{y,l}(x, y)|$ of the y direction wave components for a linear wave problem initialized with the right-moving fast magnetosonic wave. For a correct decomposition, all of the y direction components should be significantly weaker than the dominant component in the x direction (see figure E.1).

We take a linear wave problem initialized with a right-moving fast magnetosonic wave ($\bar{\mathbf{R}}_7$), and obtain the characteristic variable wave decompositions at time $t_2 = 0.03$ with respect to time $t_1 = 0$.

Figure E.1 shows plots of the wave component strengths in the x direction, $|Q^{(2)}_{x,l}(x, y)|$. It is clear that the decomposition in the x direction was successful in recovering the dominant wave component, with other components orders of magnitude weaker (the actual values are on the order of the numerical error, 10^{-16}).

Figure E.2 shows plots of the wave component strengths in the y direction, $|Q^{(2)}_{y,l}(x, y)|$. As there is no wave propagating in the y direction in the given linear wave problem, in a correct decomposition all of the components would be zero, or at least significantly weaker than the dominant x direction component. However, as can be seen from the plots, that is not the case; the obtained y direction wave components are of the same order as the dominant x direction component.

From the above results, we can surmise that the characteristic variable decomposition method works correctly *only* in the direction of wave propagation. To see why this may be the case, consider the wave decompositions as expressed by equations (E.11) and (E.12), and substitute the linear wave problem. Then,

$$\mathbf{U}^{(1)}(x, y) = \mathbf{U}^{(0)}(x - \lambda t_1, y) = \bar{\mathbf{U}} + \varepsilon \bar{\mathbf{R}}_x \cos(2\pi(x - \lambda t_1)), \tag{E.13}$$

$$\mathbf{U}^{(2)}(x, y) = \mathbf{U}^{(0)}(x - \lambda t_2, y) = \bar{\mathbf{U}} + \varepsilon \bar{\mathbf{R}}_x \cos(2\pi(x - \lambda t_2)), \tag{E.14}$$

where $\bar{\mathbf{R}}_x$ is the chosen right eigenvector of the Jacobian of the x direction flux $\mathbf{F}(\bar{\mathbf{U}})$ of the uniform background $\bar{\mathbf{U}}$, and λ is the corresponding eigenvalue. Substituting into the x direction wave decomposition, we obtain

$$\mathbf{Q}^{(2)}_x(x, y) = \epsilon L^{(1)}_x(x, y)\bar{\mathbf{R}}_x(\cos(2\pi(x - \lambda t_2)) - \cos(2\pi(x - \lambda t_1))), \tag{E.15}$$

which appears to successfully recover the wave amplitude ϵ. On the other hand, substituting into the y direction wave decomposition, we obtain

$$\mathbf{Q}^{(2)}_y(x, y) = \epsilon L^{(1)}_y(x, y)\bar{\mathbf{R}}_x(\cos(2\pi(x - \lambda t_2)) - \cos(2\pi(x - \lambda t_1))), \tag{E.16}$$

where $L_y^{(1)}(x, y)$ and $\bar{\mathbf{R}}_x$ are eigenvectors of different Jacobians; $\bar{\mathbf{R}}_x$ is obtained from the Jacobian of the x direction flux $\mathbf{F}$, while $L_y^{(1)}$ is obtained from the Jacobian of the y direction flux $\mathbf{G}$. It becomes clear that the decomposition is only valid in the direction of wave propagation; in other words, the characteristic variable method of wave decomposition can be used only on 1D problems.

E.3 Characteristic flux method

In contrast to the characteristic variable method introduced in the previous section, which was derived from the properties of the 1D linear wave problem, this method (introduced in section 5.6) is obtained directly from the diagonalization of a conservation law.

We can extend the 1D decomposition to 2D as

$$\mathbf{S}_{x,i+\frac{1}{2},j} = L_{x,i+\frac{1}{2},j}(\mathbf{F}_{i+1,j} - \mathbf{F}_{i,j}), \tag{E.17}$$

$$\mathbf{S}_{y,i,j+\frac{1}{2}} = L_{y,i,j+\frac{1}{2}}(\mathbf{G}_{i,j+1} - \mathbf{G}_{i,j}) \tag{E.18}$$

where $L_{x,i+\frac{1}{2},j} = L_x(\mathbf{U}_{i+\frac{1}{2},j})$ and $L_{y,i,j+\frac{1}{2}} = L_y(\mathbf{U}_{i,j+\frac{1}{2}})$ are, respectively, locally frozen matrices of the left eigenvectors of fluxes $\mathbf{F}$ and $\mathbf{G}$, with $\mathbf{U}_{i+\frac{1}{2},j}$ and $\mathbf{U}_{i,j+\frac{1}{2}}$ as the midpoint values obtained through averaging [32]; while $\mathbf{S}_{x,i+\frac{1}{2},j}$ and $\mathbf{S}_{y,i,j+\frac{1}{2}}$ are the decompositions of the wave components in x and y directions, with $|S_{x,i+\frac{1}{2},j,l}|$ and $|S_{y,i,j+\frac{1}{2},l}|$ being the strengths of l-th wave component ($l = 1, \ldots, 7$) in x and y directions.

As in the previous section, we take a linear wave problem initialized with a right-moving fast magnetosonic wave ($\bar{\mathbf{R}}_7$), and obtain the characteristic variable wave decompositions at time $t = 0$ (i.e., for the initial conditions).

Figure E.3 shows plots of the wave component strengths in the x direction, $|S_{x,i+\frac{1}{2},j,l}|$. As can be clearly seen from the plots, the x direction fast magnetosonic wave component is successfully recovered, and other components are several degrees of magnitude below it (the actual values are, as before, on the order of the numerical error, 10^{-16}).

Figure E.4 shows plots of the wave component strengths in the y direction, $|S_{y,i,j+\frac{1}{2},l}|$. Recall that there is no wave propagating in the y direction in the

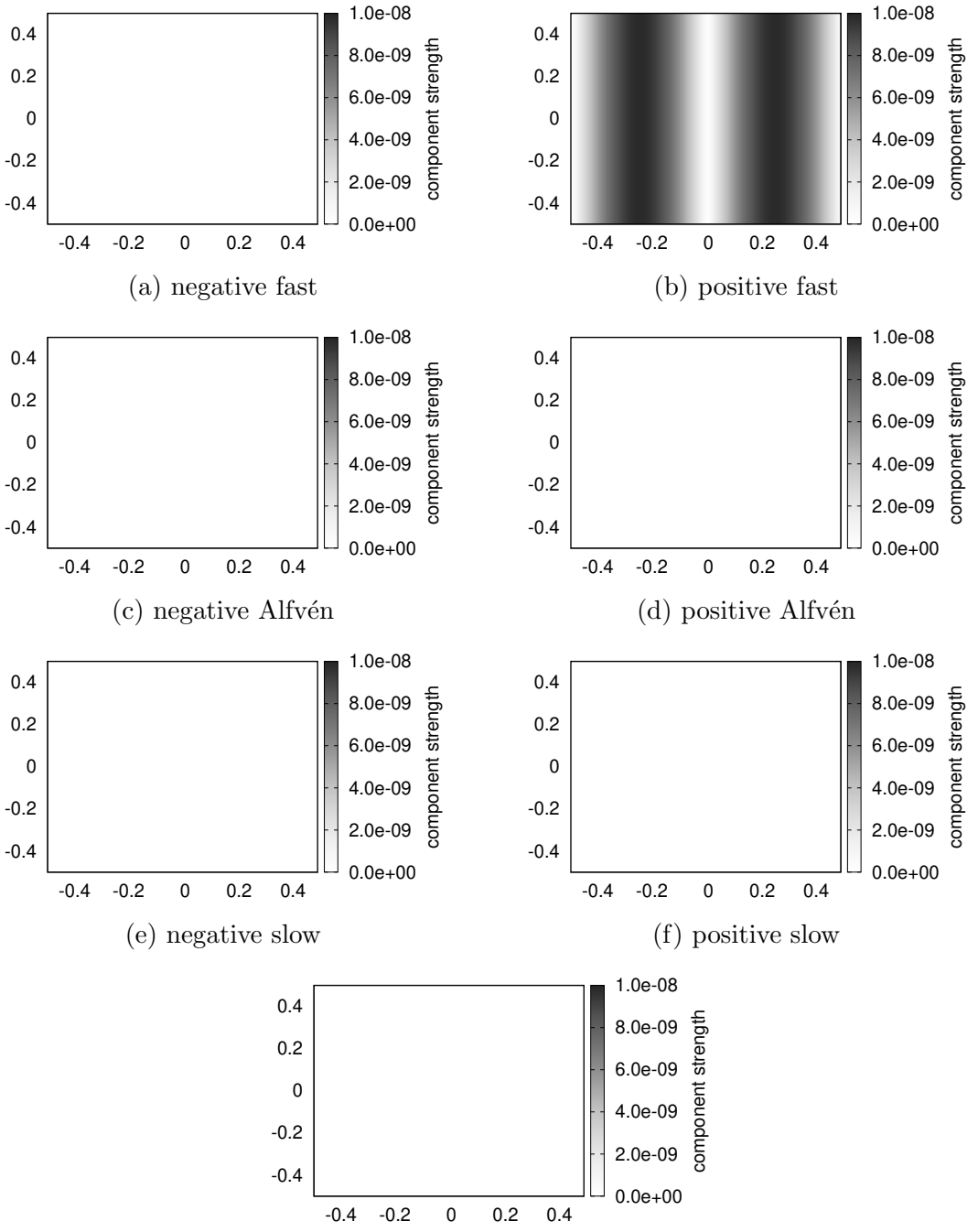

(a) negative fast

(b) positive fast

(c) negative Alfvén

(d) positive Alfvén

(e) negative slow

(f) positive slow

(g) entropy

Figure E.3: Strength $|S_{x,i+\frac{1}{2},j,l}|$ of the x direction wave components for a linear wave problem initialized with the right-moving (i.e., positive) fast magnetosonic wave. The positive fast magnetosonic component is dominant; other six components are on the order of numerical error.

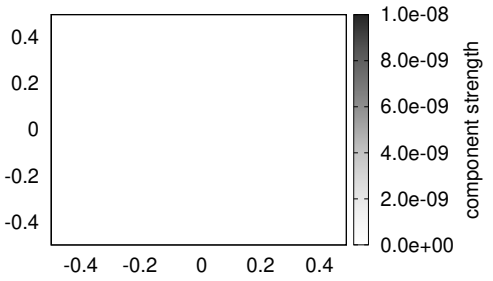

(a) negative fast

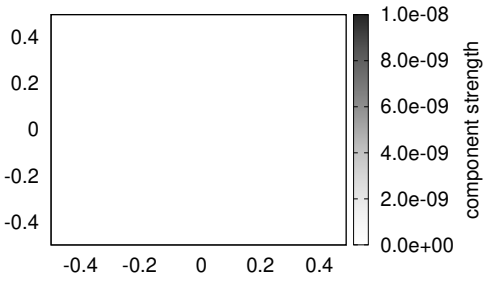

(b) positive fast

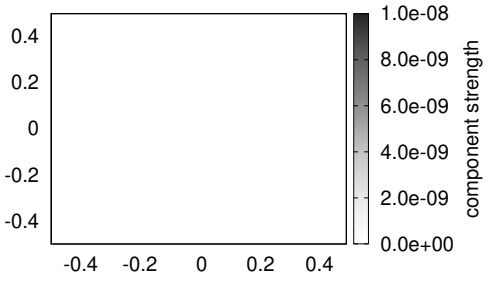

(c) negative Alfvén

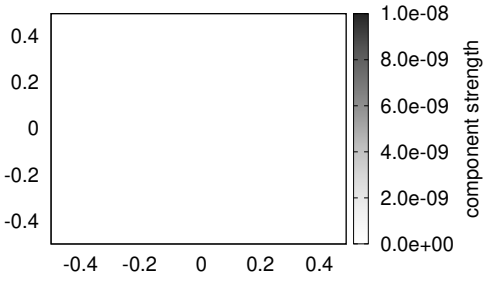

(d) positive Alfvén

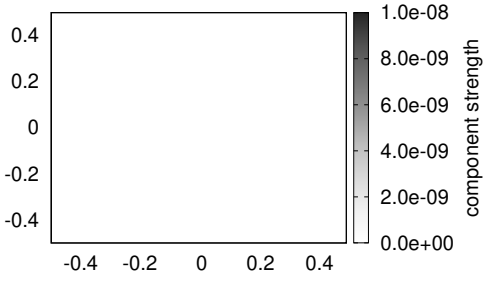

(e) negative slow

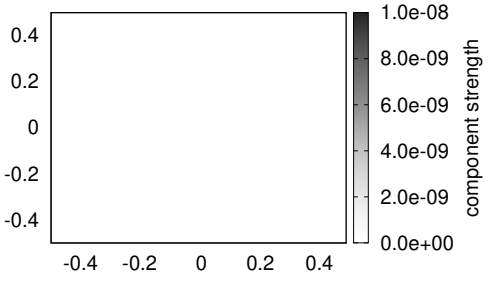

(f) positive slow

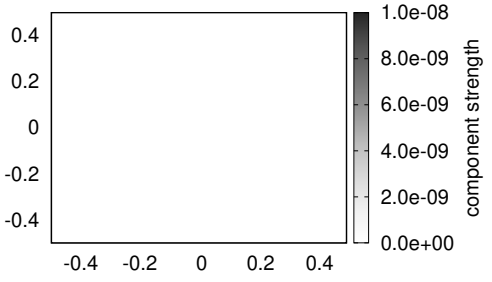

(g) entropy

Figure E.4: Strength $|S_{y,i,j+\frac{1}{2},l}|$ of the y direction wave components for a linear wave problem initialized with the right-moving fast magnetosonic wave. All of the y direction components are equal to zero over the entire domain.

given linear wave problem, and therefore, there should be no detectable y direction component. Looking at the plots for individual wave components, we can confirm that none of the y direction components are visible; indeed, the actual values are identical to 0 over the entire domain.

Tests for the other six waves gave similar results. Therefore, we can conclude that, at least in the case of linear waves, the wave decomposition method described in section 5.6 works correctly.

Appendix F

Scaling

In this appendix, we describe an unsuccessful attempt to analytically determine the dependence of the thinning front velocity u_{F} on plasma sheet parameters. The writeup is provided for informational purposes, to perhaps help anyone else wishing to do the same by providing some ideas and showing a few failed approaches.

From the simulation results (figure 5.7b), we anticipate that the scaling for the front velocity u_{F} should be

$$u_{\mathrm{F}} \sim B_0. \tag{F.1}$$

Or, put another way, the scaling for the front location x_{F} should be

$$x_{\mathrm{F}} \sim B_0 t. \tag{F.2}$$

There is also a minor lobe density (i.e., temperature ratio τ) dependence. There could be other variables as well, though it appears that there should *not* be a dependence on initial velocity.

Assuming constant outflow on the Earth side of the simulated plasma sheet, the volume flow rate (or rather, area flow rate) for sheet plasma loss is

$$Q = -h_{\mathrm{sheet}} u_{\mathrm{init}}. \tag{F.3}$$

As plasma is lost from the sheet, the sheet pressure drops and lobe plasma pushes inward, compressing the sheet plasma, which increases the pressure

again. Assuming that, after re-compression, the density change of sheet plasma is negligible, the volume (i.e., cross-sectional area) reduction of the plasma sheet is

$$A_{\text{loss}} = h_{\text{sheet}} u_{\text{init}} t. \tag{F.4}$$

However, another consequence of the lobe plasma moving inward is a distortion of the lobe magnetic field. The magnetic tension thus generated is another force that needs to be balanced.

F.1 Curved thinning boundary

Assume the disturbed sheet–lobe boundary forms an arc (figure F.1) of radius R and angle φ, with arc length l, chord length $a = 2\Delta x$, circle segment height Δy, and area A,

$$a = 2R \sin \frac{\varphi}{2}, \tag{F.5}$$

$$\varphi = 2 \sin^{-1} \frac{a}{2R}, \tag{F.6}$$

$$l = 2R\pi \frac{\varphi}{2\pi} = R\varphi, \tag{F.7}$$

$$\Delta y = R(1 - \cos \frac{\varphi}{2}), \tag{F.8}$$

$$A = R^2 \pi \frac{\varphi}{2\pi} - \frac{1}{2} a(R - \Delta y) = \frac{1}{2} R^2 (\varphi - \sin \varphi). \tag{F.9}$$

We attempt to balance the force that comes from pressure difference with the force that comes from magnetic tension. As this is a 2D model, all forces are implicitly assumed to be per unit length along z.

The magnitude of the force generated by pressure difference is

$$F_{\text{p}} = (p_{\text{tot,lobe}} - p_{\text{sheet}}) l, \tag{F.10}$$

where $p_{\text{tot,lobe}}$ is the total lobe pressure, which we assume is constant even after the deformation,

$$p_{\text{tot,lobe}} = p_0, \tag{F.11}$$

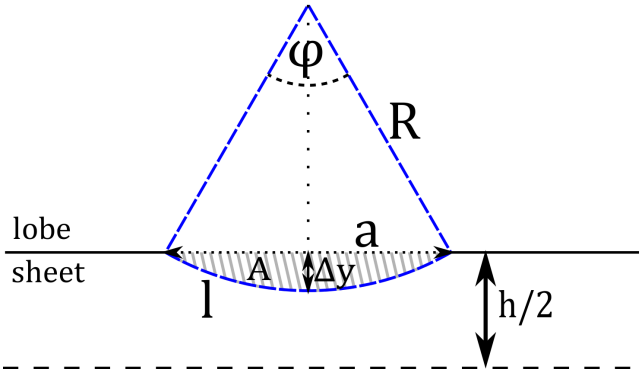

Figure F.1: Shape and parameters for a curved disturbance scaling model; only the upper (north) half of the sheet is shown.

and $p_{\rm sheet}$ is the sheet pressure after deformation,

$$\frac{p_{\rm sheet}}{p_{\rm mid}} = \frac{\frac{1}{2}h_{\rm sheet}a}{\frac{1}{2}h_{\rm sheet}a - A}, \tag{F.12}$$

with $p_{\rm mid}$ being the midpoint (minimum) pressure of the plasma sheet from the exact solution of the 1D model in equation (4.2),

$$p_{\rm mid} = \alpha p_0, \tag{F.13}$$

$$\alpha \equiv \left[1 - \frac{1}{2}(\gamma - 1)\frac{u_{\rm init}}{2c_{\rm s}}\right]^{\frac{2\gamma}{\gamma-1}}. \tag{F.14}$$

As an example, for $\gamma = 5/3, p = 1, \rho = 1, u_{\rm init} = 1$, we obtain $\alpha \approx 0.501$. Then, the pressure difference force is

$$F_{\rm p} = p_0 l \left(1 - \frac{\frac{1}{2}h_{\rm sheet}a\alpha}{\frac{1}{2}h_{\rm sheet}a - A}\right). \tag{F.15}$$

The force due to the magnetic tension of the deformed magnetic field lines is

$$\mathbf{F}_{\rm T} = \iint_{A_{\rm D}} (\mathbf{B}\cdot\boldsymbol{\nabla})\mathbf{B}\,{\rm d}\varphi{\rm d}r \tag{F.16}$$

where $A_{\rm D}$ is the deformed area. We place the center of the coordinate system at the center of the circle, with x coordinate parallel to the plasma sheet, and

assume a circular deformation with no change in magnitude of the field,

$$\mathbf{B} = \frac{B_0}{\sqrt{x^2+y^2}} \begin{pmatrix} y \\ -x \\ 0 \end{pmatrix} = -B_0 \mathbf{e}_\theta, \tag{F.17}$$

$$(\mathbf{B}\cdot\boldsymbol{\nabla})\mathbf{B} = -\frac{B_0^2}{x^2+y^2} \begin{pmatrix} x \\ y \\ 0 \end{pmatrix} = -\frac{B_0^2}{r}\mathbf{e}_r. \tag{F.18}$$

The x component will obviously integrate to 0, so it can be dropped. Transforming to Cartesian coordinates and limiting the deformation to the circular segment, the magnitude of the magnetic tension force becomes

$$F_\mathrm{T} = 2\int_0^{a/2} \mathrm{d}x \int_{-\sqrt{R^2-x^2}}^{-(R-\Delta y)} \mathrm{d}y \, \frac{-B_0^2 y}{x^2+y^2} \tag{F.19}$$

$$= 2B_0^2 \int_0^{a/2} \mathrm{d}x \int_{R-\Delta y}^{\sqrt{R^2-x^2}} \mathrm{d}y \, \frac{y}{x^2+y^2} \tag{F.20}$$

$$= 2B_0^2 \int_0^{a/2} \mathrm{d}x \left[\frac{1}{2}\log(x^2+y^2)\right]_{y=R-\Delta y}^{y=\sqrt{R^2-x^2}} \tag{F.21}$$

$$= 2B_0^2 \int_0^{a/2} \mathrm{d}x \left(-\frac{1}{2}\log(x^2+(R-\Delta y)^2) + \frac{1}{2}\log(x^2+R^2-x^2)\right) \tag{F.22}$$

$$= B_0^2 \int_0^{a/2} \mathrm{d}x \left(\log(R^2) - \log(x^2+R^2\cos^2(\varphi/2))\right) \tag{F.23}$$

$$= B_0^2 \big[x\log(R^2) + 2x - x\log(x^2+R^2\cos^2(\varphi/2)) \\ -2R\cos(\varphi/2)\tan^{-1}(x/R\cos(\varphi/2))\big]_0^{a/2} \tag{F.24}$$

$$= B_0^2 \big(R\sin(\varphi/2)\log(R^2) + 2R\sin(\varphi/2) \\ - R\sin(\varphi/2)\log(R^2\sin^2(\varphi/2)+R^2\cos^2(\varphi/2)) \\ -2R\cos(\varphi/2)\tan^{-1}(\tan(\varphi/2))\big) \tag{F.25}$$

$$= B_0^2(2R\sin(\varphi/2) - R\varphi\cos(\varphi/2)). \tag{F.26}$$

Comparing the two forces, we obtain

$$F_\mathrm{T} \sim F_\mathrm{p} \tag{F.27}$$

$$B_0^2(2R\sin(\varphi/2) - R\varphi\cos(\varphi/2)) \sim p_0 l \left(1 - \frac{\frac{1}{2}h_\mathrm{sheet}a\alpha}{\frac{1}{2}h_\mathrm{sheet}a - A}\right). \tag{F.28}$$

Taylor expanding the left side for small φ,

$$2\sin(\varphi/2) - \varphi\cos(\varphi/2) = \varphi - \frac{\varphi^3}{24} + O(\varphi^5) - \varphi + \frac{\varphi^3}{8} + O(\varphi^5) \tag{F.29}$$

$$\approx \varphi^3/12. \tag{F.30}$$

Then, and taking (F.7) and $A = A_{\text{loss}}/2$,

$$\frac{B_0^2 R\varphi^3}{24 p_0 R\varphi} \sim \frac{\frac{1}{2}h_{\text{sheet}}a - \frac{1}{2}h_{\text{sheet}}u_{\text{init}}t - \frac{1}{2}h_{\text{sheet}}a\alpha}{\frac{1}{2}h_{\text{sheet}}a - \frac{1}{2}h_{\text{sheet}}u_{\text{init}}t} \tag{F.31}$$

$$\frac{B_0^2\varphi^2}{p_0} \sim \frac{a - u_{\text{init}}t - a\alpha}{a - u_{\text{init}}t}. \tag{F.32}$$

Since the midpoint of the disturbance is moving to the left at the velocity $u = -u_{\text{init}}/2$, the right–side front of the disturbance x_{F} is located at

$$x_{\text{F}} = -\frac{1}{2}u_{\text{init}}t + \frac{1}{2}a, \tag{F.33}$$

therefore

$$\frac{B_0^2\varphi^2}{p_0} \sim \frac{2x_{\text{F}} - \alpha a}{2x_{\text{F}}}. \tag{F.34}$$

From (F.5) and (F.9), for small φ, we obtain

$$a \approx R\varphi, \tag{F.35}$$

$$A \approx \frac{1}{2}R^2\left(\varphi - \varphi + \frac{1}{6}\varphi\right) \approx \frac{1}{12}a^2\varphi. \tag{F.36}$$

Using equation (F.4) for plasma loss from the sheet, we have

$$A \approx \frac{1}{2}A_{\text{loss}} = \frac{1}{2}h_{\text{sheet}}u_{\text{init}}t, \tag{F.37}$$

$$\varphi \approx 6\frac{h_{\text{sheet}}u_{\text{init}}t}{a^2}. \tag{F.38}$$

Substituting φ into (F.34) and dropping the constant,

$$\frac{B_0^2 h_{\text{sheet}}^2 u_{\text{init}}^2 t^2}{p_0 a^4} \sim \frac{2x_{\text{F}} - \alpha a}{2x_{\text{F}}}, \tag{F.39}$$

which can not be further manipulated.

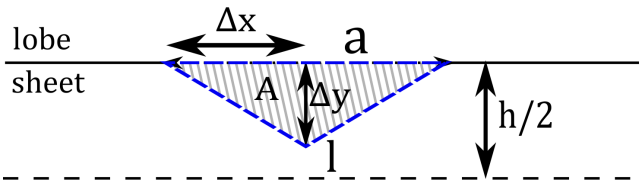

Figure F.2: Shape and parameters for a straight disturbance scaling model; only the upper (north) half of the sheet is shown.

Assumptions from simulation

If we assume that $x_\mathrm{F}/a \sim$ const (both fronts travel at the same velocity), then the right-hand side is a constant, and we obtain

$$a^4 \sim \frac{B_0^2 h_\mathrm{sheet}^2 u_\mathrm{init}^2 t^2}{p_0}, \tag{F.40}$$

$$a \sim \frac{\sqrt{B_0 h_\mathrm{sheet} u_\mathrm{init} t}}{p_0^{1/4}}. \tag{F.41}$$

Since we assumed that $a \sim x_\mathrm{F}$, then

$$x_\mathrm{F} \sim \frac{\sqrt{B_0 h_\mathrm{sheet} u_\mathrm{init} t}}{p_0^{1/4}}. \tag{F.42}$$

However, this implies that the front velocity u_F scales like

$$u_\mathrm{F} = x_\mathrm{F}/t \sim \frac{\sqrt{B_0 h_\mathrm{sheet} u_\mathrm{init}}}{p_0^{1/4}\sqrt{t}}, \tag{F.43}$$

i.e., $u_\mathrm{F} \sim t^{-1/2}$, while the simulation indicates it should be $u_\mathrm{F} \sim$ const. Furthermore, it conflicts with the assumption; $a \sim x_\mathrm{F}$, from (F.33), implies $x_\mathrm{F} \sim t$.

F.2 Straight thinning boundary with static pressure

Assume the disturbed sheet–lobe boundary forms an isosceles triangle, with height Δy and base length $2\Delta x$ (figure F.2).

$$a = 2\Delta x, \tag{F.44}$$

$$l = \sqrt{\Delta x^2 + \Delta y^2} \tag{F.45}$$

$$A = \Delta x \Delta y. \tag{F.46}$$

To simplify parts of the calculation, we also introduce the ratio r,

$$r = \frac{\Delta x}{\Delta y}. \tag{F.47}$$

For the magnetic field, we again assume that only the direction changes and the magnitude stays approximately constant,

$$B_x^2 + B_y^2 = B_0^2, \tag{F.48}$$

$$\frac{B_x}{B_y} = \frac{\Delta x}{\Delta y} = r. \tag{F.49}$$

Then, using

$$B_x = rB_y \tag{F.50}$$

from (F.49) and substituting into (F.48) we get

$$(r^2 + 1)B_y^2 = B_0^2, \tag{F.51}$$

which gives

$$B_y^2 = \frac{B_0^2}{r^2 + 1}, \tag{F.52}$$

$$B_x^2 = \frac{r^2 B_0^2}{r^2 + 1}. \tag{F.53}$$

As before, we attempt to balance the force that comes from pressure difference with the force that comes from magnetic tension. The pressure difference force is the same as in the curved case, shown in equation (F.15). In Cartesian coordinates, the magnetic tension force from (F.16) becomes

$$\mathbf{F}_{\mathrm{T}} = \iint_{A_{\mathrm{D}}} (\mathbf{B} \cdot \boldsymbol{\nabla})\mathbf{B} \, \mathrm{d}x\mathrm{d}y, \tag{F.54}$$

where A_{D} is the deformed area. Taking the deformation area to be the area A of the shaded triangle in figure F.2, the x-component will again vanish due to symmetry, and the y-component becomes

$$F_{\mathrm{T}} = \iint_A (\mathbf{B} \cdot \boldsymbol{\nabla})B_y \, \mathrm{d}x\mathrm{d}y \tag{F.55}$$

$$= \iint_A (B_x \frac{\partial B_y}{\partial x} + B_y \frac{\partial B_y}{\partial y}) \, \mathrm{d}x\mathrm{d}y. \tag{F.56}$$

As B_y does not change in the y direction inside the relevant area,

$$F_{\mathrm{T}} = \iint_A B_x \frac{\partial B_y}{\partial x} \, \mathrm{d}x\mathrm{d}y. \tag{F.57}$$

Approximating this integral over the area A,

$$\begin{aligned} F_{\mathrm{T}} &\approx B_x \frac{2B_y}{\Delta x} A && \text{(F.58)} \\ &= 2B_x B_y \Delta y && \text{(F.59)} \\ &= 2\Delta y \frac{r B_0^2}{r^2+1} && \text{(F.60)} \\ &= 2\Delta x \frac{B_0^2}{r^2+1}. && \text{(F.61)} \end{aligned}$$

Comparing the two forces, we get

$$\begin{aligned} F_{\mathrm{T}} &\sim F_{\mathrm{p}} && \text{(F.62)} \\ 2\Delta x \frac{B_0^2}{r^2+1} &\sim p_0 l \left(1 - \frac{\frac{1}{2} h_{\mathrm{sheet}} a\alpha}{\frac{1}{2} h_{\mathrm{sheet}} a - A}\right). && \text{(F.63)} \end{aligned}$$

Dropping the constant, assuming

$$\Delta x \gg \Delta y \tag{F.64}$$

(which also gives us $r \gg 1$), and using $2A = h_{\mathrm{sheet}} u_{\mathrm{init}} t$, we get

$$\begin{aligned} \Delta x \frac{B_0^2}{r^2} &\sim p_0 \Delta x \left(1 - \frac{a\alpha}{a - u_{\mathrm{init}} t}\right) && \text{(F.65)} \\ B_0^2 \Delta y^2 &\sim p_0 \Delta x^2 \left(1 - \frac{\Delta x \alpha}{\Delta x - \frac{1}{2} u_{\mathrm{init}} t}\right). && \text{(F.66)} \end{aligned}$$

Comparing the two expressions for the area,

$$\begin{aligned} \Delta x \Delta y &= \frac{1}{2} h_{\mathrm{sheet}} u_{\mathrm{init}} t && \text{(F.67)} \\ \Delta y &= \frac{1}{2\Delta x} h_{\mathrm{sheet}} u_{\mathrm{init}} t, && \text{(F.68)} \end{aligned}$$

and using the relationship (F.33), we obtain

$$B_0^2 h_{\mathrm{sheet}}^2 u_{\mathrm{init}}^2 t^2 \sim p_0 \Delta x^4 \left(1 - \frac{\Delta x \alpha}{x_{\mathrm{F}}}\right), \tag{F.69}$$

which, again, can not be further manipulated.

Assumptions from simulation

If we assume that $\Delta x/x_{\mathrm{F}} \approx$ const (i.e., they have similar scaling),

$$B_0^2 h_{\mathrm{sheet}}^2 u_{\mathrm{init}}^2 t^2 \sim p_0 \Delta x^4 \tag{F.70}$$

$$\Delta x \sim \frac{\sqrt{B_0 h_{\mathrm{sheet}} u_{\mathrm{init}} t}}{p_0^{1/4}}. \tag{F.71}$$

As in the previous section, since we assumed that $\Delta x \sim x_{\mathrm{F}}$, then

$$x_{\mathrm{F}} \sim \frac{\sqrt{B_0 h_{\mathrm{sheet}} u_{\mathrm{init}} t}}{p_0^{1/4}}, \tag{F.72}$$

and this again gives us $u_{\mathrm{F}} \sim t^{-1/2}$ instead of $u_{\mathrm{F}} \sim$ const, with the accompanying violation of implied $x_{\mathrm{F}} \sim t$.

F.3 Straight thinning boundary with dynamic pressure

As the above two approaches have failed, we try to add an alternative approach, where the main force balancing with magnetic tension is not the pressure difference, but dynamic pressure,

$$p_{\mathrm{D}} = \frac{1}{2}\rho u^2. \tag{F.73}$$

Converting the dynamic pressure to a force, and assuming the other side is stationary, we get (in 2D)

$$F_{\mathrm{D}} = \int \frac{1}{2}\rho u^2 \mathrm{d}l. \tag{F.74}$$

Assuming that the density is approximately equal to the initial density ρ_0, and remembering that the initial velocity goes from $-u_{\mathrm{init}}$ to 0 over the relevant range, we find that the integral is approximately

$$F_{\mathrm{D}} \sim \rho_0 u_{\mathrm{init}}^2 l. \tag{F.75}$$

Using the same magnetic tension force as in the previous case (and ignoring the constant coefficients),

$$F_{\mathrm{T}} \sim F_{\mathrm{D}} \tag{F.76}$$

$$\Delta x \frac{B_0^2}{r^2+1} \sim \rho_0 u_{\mathrm{init}}^2 l \tag{F.77}$$

$$\Delta x \frac{B_0^2}{r^2+1} \sim \rho_0 u_{\mathrm{init}}^2 \sqrt{\Delta x^2 + \Delta y^2}. \tag{F.78}$$

Taking $\Delta x \gg \Delta y$,

$$\Delta x \frac{B_0^2}{r^2} \sim \rho_0 u_{\mathrm{init}}^2 \sqrt{\Delta x^2} \tag{F.79}$$

$$\frac{B_0^2 \Delta y^2}{\Delta x^2} \sim \rho_0 u_{\mathrm{init}}^2 \tag{F.80}$$

$$B_0^2 \Delta y^2 \sim \rho_0 u_{\mathrm{init}}^2 \Delta x^2. \tag{F.81}$$

From (F.68),

$$B_0^2 \frac{1}{4\Delta x^2} h_{\mathrm{sheet}}^2 u_{\mathrm{init}}^2 t^2 \sim \rho_0 u_{\mathrm{init}}^2 \Delta x^2 \tag{F.82}$$

$$B_0^2 h_{\mathrm{sheet}}^2 t^2 \sim \rho_0 \Delta x^4 \tag{F.83}$$

$$\Delta x^2 \sim \frac{B_0}{\sqrt{\rho_0}} h_{\mathrm{sheet}} t. \tag{F.84}$$

We have at least obtained the scaling for Δx. However, what is required is scaling for x_{F}, which cannot be determined without additional assumptions.

Assumptions from simulation

If we once more assume that $\Delta x / x_{\mathrm{F}} \approx \mathrm{const}$, we obtain

$$x_{\mathrm{F}} \sim \frac{\sqrt{B_0 h_{\mathrm{sheet}} t}}{\rho_0^{1/4}}, \tag{F.85}$$

which, as before, gives us $u_{\mathrm{F}} \sim t^{-1/2}$ instead of $u_{\mathrm{F}} \sim \mathrm{const}$ and the violation of implied $x_{\mathrm{F}} \sim t$.

Therefore, neither of the three simplified models have been useful in determining the dependence of thinning velocity on plasma sheet parameters.

Acknowledgements

First of all, I would like to thank my advisor, Professor Tomo Tatsuno. It is not an exaggeration to say that without Prof. Tatsuno, this thesis would likely never be completed. I have leaned heavily on his knowledge and experience to point me in the right direction, and most of all, relied on him to push me to act despite my procrastinating tendencies.

I would also like to thank my secondary advisor, Professor Keisuke Hosokawa, for providing the idea for the research topic, and frequent discussions about theory and observations that underpin any simulation worth its salt.

The thesis was dramatically improved thanks to comments by the supervisory committee; my sincere thanks to Professor Nobito Yamamoto, Professor Yoshinobu Nakatani, and Professor Tadashi Yamazaki.

For useful discussions that helped with solving issues around development of the simulation, I thank Dr. Takashi Minoshima of the Japan Agency for Marine-Earth Science and Technology (JAMSTEC) and Professor William Dorland of the University of Maryland.

I also thank the Japanese Government and the Rotary Club for scholarships that have supported me through most of my study in Japan.

After the said scholarships ended, I had to find part-time work to finance myself. My boss, Ms. Hiroko Masuyama, was very supportive of my studies and allowed me a fairly flexible schedule—especially when a deadline loomed ahead, for which I am very thankful.

Finally, I thank my family, Tretlers and Kličkovićs, for their emotional and financial support over these 13 years abroad, and especially my grandmother Vida for occasional packages of home-baked cookies.

List of publications

Publications

1. Rudolf Tretler, Tomo Tatsuno, and Keisuke Hosokawa, "Loss of the rarefaction wave during plasma sheet thinning," *Plasma and Fusion Research*, vol. 15, 2401053, 2020.

2. Rudolf Tretler, Tomo Tatsuno, and Keisuke Hosokawa, "Plasma sheet thinning due to loss of near-Earth magnetotail plasma," *Journal of Plasma Physics*, vol. 87, 905870108, 2021.

3. Miyagawa Yamato, Tretler Rudolf, and Tatsuno Tomoya, "Automatic tuning of reduced MHD simulation code," *Journal of Plasma and Fusion Research*, vol. 93, no. 6, pp. 271–277, 2017.

Bibliography

[1] S.-I. Akasofu, *Polar and magnetospheric substorms*. Springer, 1968.

[2] A. T. Y. Lui, "A synthesis of magnetospheric substorm models," *Journal of Geophysical Research: Space Physics*, vol. 96, no. A2, pp. 1849–1856, 1991.

[3] L. A. Frank, J. B. Sigwarth, J. D. Craven, J. P. Cravens, J. S. Dolan, M. R. Dvorsky, P. K. Hardebeck, J. D. Harvey, and D. W. Muller, "The visible imaging system (VIS) for the polar spacecraft," *Space Science Reviews*, vol. 71, no. 1-4, pp. 297–328, 1995.

[4] NASA/Goddard Space Flight Center Scientific Visualization Studio, "Auroral substorm from Polar." `https://svs.gsfc.nasa.gov/3513`, July 2008.

[5] D. N. Baker, T. I. Pulkkinen, V. Angelopoulos, W. Baumjohann, and R. L. McPherron, "Neutral line model of substorms: Past results and present view," *Journal of Geophysical Research*, vol. 101, no. A6, pp. 12975–13010, 1996.

[6] A. T. Y. Lui, C.-I. Meng, and S.-I. Akasofu, "Search for the magnetic neutral line in the near-Earth plasma sheet 2. Systematic study of Imp 6 magnetic field observations," *Journal of Geophysical Research*, vol. 82, no. 10, pp. 1547–1565, 1977.

[7] J. K. Chao, J. R. Kan, A. T. Y. Lui, and S.-I. Akasofu, "A model for thinning of the plasma sheet," *Planetary and Space Science*, vol. 25, pp. 703–710, 1977.

[8] V. Angelopoulos, "The THEMIS mission," *Space Science Reviews*, vol. 141, no. 5, 2008.

[9] W. Baumjohann and R. A. Treumann, *Basic Space Plasma Physics, Revised Edition*. Imperial College Press, 2012.

[10] D. Biskamp, *Magnetic reconnection in plasmas*. Cambridge University Press, 2000.

[11] Y. Asano, T. Mukai, M. Hoshino, Y. Saito, H. Hayakawa, and T. Nagai, "Current sheet structure around the near-Earth neutral line observed by Geotail," *Journal of Geophysical Research: Space Physics*, vol. 109, no. A2, 2004.

[12] A. T. Y. Lui, "Current disruption in the Earth's magnetosphere: Observations and models," *Journal of Geophysical Research: Space Physics*, vol. 101, no. A6, pp. 13067–13088, 1996.

[13] K. Takahashi, L. J. Zanetti, R. E. Lopez, R. W. McEntire, T. A. Potemra, and K. Yumoto, "Disruption of the magnetotail current sheet observed by AMPTE/CCE," *Geophysical Research Letters*, vol. 14, no. 10, pp. 1019–1022, 1987.

[14] A. T. Y. Lui, R. E. Lopez, B. J. Anderson, K. Takahashi, L. J. Zanetti, R. W. McEntire, T. A. Potemra, D. M. Klumpar, E. M. Greene, and R. Strangeway, "Current disruptions in the near-earth neutral sheet region," *Journal of Geophysical Research: Space Physics*, vol. 97, no. A2, 1992.

[15] C. L. Tang, Z. Y. Li, V. Angelopoulos, S. B. Mende, K. H. Glassmeier, E. Donovan, C. T. Russell, and L. Lu, "THEMIS observations of the near-Earth plasma sheet during a substorm," *Journal of Geophysical Research: Space Physics*, vol. 114, no. A9, 2009.

[16] J. R. Kan, "A global magnetosphere-ionosphere coupling model of substorms," *Journal of Geophysical Research: Space Physics*, vol. 98, no. A10, pp. 17263–17275, 1993.

[17] E. Hameiri, P. Laurence, and M. Mond, "The ballooning instability in space plasmas," *Journal of Geophysical Research: Space Physics*, vol. 96, no. A2, pp. 1513–1526, 1991.

[18] K. Schindler, "Plasma and fields in the magnetospheric tail," *Space Science Reviews*, vol. 17, no. 2-4, pp. 589–614, 1975.

[19] J. G. Lyon, S. H. Brecht, J. D. Huba, J. A. Fedder, and P. J. Palmadesso, "Computer simulation of a geomagnetic substorm," *Physical Review Letters*, vol. 46, no. 15, p. 1038, 1981.

[20] R. J. Walker, T. Ogino, J. Raeder, and M. Ashour-Abdalla, "A global magnetohydrodynamic simulation of the magnetosphere when the interplanetary magnetic field is southward: The onset of magnetotail reconnection," *Journal of Geophysical Research: Space Physics*, vol. 98, no. A10, pp. 17235–17249, 1993.

[21] T. Tanaka, A. Nakamizo, A. Yoshikawa, S. Fujita, H. Shinagawa, H. Shimazu, T. Kikuchi, and K. K. Hashimoto, "Substorm convection and current system deduced from the global simulation," *Journal of Geophysical Research: Space Physics*, vol. 115, no. A5, 2010.

[22] K. Shiokawa, Y. Miyashita, I. Shinohara, and A. Matsuoka, "Decrease in b_z prior to the dipolarization in the near-Earth plasma sheet," *Journal of Geophysical Research: Space Physics*, vol. 110, no. A9, 2005.

[23] S. B. Mende, S. E. Harris, H. U. Frey, V. Angelopoulos, C. T. Russell, E. Donovan, B. Jackel, M. Greffen, and L. M. Peticolas, "The THEMIS array of ground-based observatories for the study of auroral substorms," *Space Science Reviews*, vol. 141, no. 357, 2008.

[24] V. Angelopoulos, J. P. McFadden, D. Larson, C. W. Carlson, S. B. Mende, H. Frey, T. Phan, D. G. Sibeck, K.-H. Glassmeier, U. Auster, *et al.*, "Tail reconnection triggering substorm onset," *Science*, vol. 321, no. 5891, pp. 931–935, 2008.

[25] A. T. Y. Lui, "Comment on "Tail reconnection triggering substorm onset"," *Science*, vol. 324, no. 5933, pp. 1391–1391, 2009.

[26] F. F. Chen, *Introduction to Plasma Physics and Controlled Fusion, Volume 1: Plasma Physics, Second Edition*. Plenum Press, 1984.

[27] D. Ryu and T. W. Jones, "Numerical magnetohydrodynamics in astrophysics: algorithm and tests for one-dimensional flow," *The Astrophysical Journal*, vol. 442, pp. 228–258, 1995.

[28] R. J. Goldston and P. H. Rutheford, *Introduction to Plasma Physics*. Taylor & Francis Group, 1995.

[29] E. F. Toro, *Riemann Solvers and Numerical Methods for Fluid Dynamics: A Practical Introduction*. Springer, 2009.

[30] D. Ryu, T. W. Jones, and A. Frank, "Numerical magnetohydrodynamics in astrophysics: algorithm and tests for multidimensional flow," *The Astrophysical Journal*, vol. 452, pp. 785–796, 1995.

[31] T. Tatsuno, *Ideal Magnetohydrodynamic Spectra of Static and Flowing Plasmas*. PhD thesis, Kyoto University, January 2002.

[32] M. Brio and C. C. Wu, "An upwind differencing scheme for the equations of ideal magnetohydrodynamics," *Journal of Computational Physics*, vol. 75, pp. 400–422, 1988.

[33] A. Harten, "Uniformly high order accurate essentially non-oscillatory schemes, III," *Journal of Computational Physics*, vol. 71, pp. 231–303, 1987.

[34] A. Harten, "High resolution schemes for hyperbolic conservation laws," *Journal of Computational Physics*, vol. 49, pp. 357–393, 1983.

[35] S. Gottlieb and C.-W. Shu, "Total variation diminishing Runge-Kutta schemes," *Mathematics of Computation*, vol. 67(221), pp. 73–85, 1998.

[36] C.-W. Shu, "Essentially non-oscillatory and weighted essentially non-oscillatory schemes for hyperbolic conservation laws," *Lecture Notes in Mathematics*, vol. 1697, pp. 325–432, 1998. Springer-Verlag, Berlin.

[37] C.-W. Shu and S. Osher, "Efficient implementation of essentially non-oscillatory shock capturing schemes II," *Journal of Computational Physics*, vol. 83, pp. 32–78, 1989.

[38] P. L. Roe, "Approximate Riemann solvers, parameter vectors, and difference schemes," *Journal of Computational Physics*, vol. 43, pp. 357–372, 1981.

[39] K. G. Powell, "An approximate Riemann solver for magnetohydrodynamics," *ICASE report*, vol. 94-24, 1994.

[40] W. H. Press, S. A. Teukolsky, W. T. Vetterling, and B. P. Flannery, *Numerical recipes in C*. Cambridge University Press, 1988.

[41] `www.boost.org`, "Boost 1.55.0 library." `https://www.boost.org/doc/libs/1_55_0/`, November 2013.

[42] R. Tretler, "MHD2D solver." `https://github.com/piccolo255/mhd2d-solver`, March 2019.

[43] L. D. Landau and E. M. Lifshitz, *Fluid Mechanics: Volume 6 (Course Of Theoretical Physics)*. Butterworth-Heinemann, 1987.

[44] W. Baumjohann, G. Paschmann, and C. A. Cattell, "Average plasma properties in the central plasma sheet," *Journal of Geophysical Research*, vol. 94, no. A6, pp. 6597–6606, 1989.

[45] T. Minoshima. private communication, 2018.

[46] W. Baumjohann, G. Paschmann, and H. Lühr, "Pressure balance between lobe and plasma sheet," *Geophysical Research Letters*, vol. 17, no. 1, pp. 45–48, 1990.

[47] S. Chandrasekhar, *Hydrodynamic and hydromagnetic stability.* Dover Publications, 1981.

[48] A. T. Y. Lui, M. Volwerk, M. W. Dunlop, I. V. Alexeev, A. N. Fazakerley, A. P. Walsh, M. Lester, A. Grocott, C. Mouikis, M. G. Henderson, L. M. Kistler, C. Shen, J. K. Shi, T. L. Zhang, and H. Rème, "Near-Earth substorm features from multiple satellite observations," *Journal of Geophysical Research: Space Physics*, vol. 113, no. A07S26, 2008.

[49] A. M. Rogerson and E. Meiburg, "A numerical study of the convergence properties of ENO schemes," *Journal of Scientific Computing*, vol. 5, no. 2, pp. 151–167, 1990.

[50] S. Orszag and C. Tang, "Small-scale structure of two-dimensional magnetohydrodynamic turbulence," *Journal of Fluid Mechanics*, vol. 90, pp. 129–143, 1979.

[51] J. M. Stone, T. A. Gardiner, P. Teuben, J. F. Hawley, and J. B. Simon, "Athena: A new code for astrophysical MHD," *The Astrophysical Journal Supplement Series*, vol. 178, pp. 137–177, 2008.

[52] G. A. Sod, "A survey of several finite difference methods for systems of nonlinear hyperbolic conservation laws," *Journal of Computational Physics*, vol. 27, no. 1, pp. 1–31, 1978.

[53] T. A. Gardiner and J. M. Stone, "An unsplit Godunov method for ideal MHD via constrained transport," *Journal of Computational Physics*, vol. 205, no. 2, pp. 509–539, 2005.